

Dissertation zur Erlangung des Doktorgrades
der Fakultät für Chemie und Pharmazie
der Ludwig-Maximilians-Universität München



**Structural and functional analysis of ATP dependent
conformational changes in the bacterial
Mre11:Rad50 catalytic head complex**

Carolin Möckel

aus

München

2011

Erklärung

Diese Dissertation wurde im Sinne von § 13 Abs. 3 bzw. 4 der Promotionsordnung vom 29. Januar 1998 (in der Fassung der sechsten Änderungssatzung vom 16. August 2010) von Herrn Prof. Dr. Karl-Peter Hopfner betreut.

Ehrenwörtliche Versicherung

Diese Dissertation wurde selbständig, ohne unerlaubte Hilfe erarbeitet.

München, den 19. Dezember 2011

.....
Carolin Möckel

Dissertation eingereicht am	14. Oktober 2011
1. Gutachter:	Prof. Dr. Karl-Peter Hopfner
2. Gutachter:	Prof. Dr. Patrick Cramer
Mündliche Prüfung am	12. Dezember 2011

This thesis has been prepared from November 2007 to October 2011 in the laboratory of Prof. Dr. Karl-Peter Hopfner at the Gene Center of the Ludwig-Maximilians-University of Munich (LMU).

Publications

During the work of this thesis, the following publications have been published or are in the process of being published:

Lammens K. *, Bemeleit D. J. *, Möckel C.*, Clausing E., Schele A., Hartung S., Schiller C. B., Lucas M., Angermüller C., Söding J., Strässer K., and Hopfner K.-P. (2011). *The Mre11:Rad50 Structure Shows an ATP-Dependent Molecular Clamp in DNA Double-Strand Break Repair*. Cell **145**(1): 54-66.

* These authors contributed equally to this work

Möckel C., Lammens K., Schele A., and Hopfner K.-P. (2011). *ATP driven structural changes of the bacterial Mre11:Rad50 catalytic head complex*. Nucleic Acids Res. 2011 Sep 21. [Epub ahead of print]

Schiller C.B., Lammens K., Guerini I., Coordes B., Schlauderer F., Möckel C., Schele A., Sträßer K., Jackson S. P. and Hopfner K.-P. (2011). *Insights into DNA double-strand break signaling and ataxia-telangiectasia like disease from the structure of an Mre11-Nbs1 complex*. Manuscript submitted.

Table of Contents

1. Summary	1
2. Introduction	2
2.1. DNA – history of the keystone of life	2
2.2. DNA damage.....	2
2.2.1. DNA double strand breaks (DSBs)	4
2.3. DSB repair.....	6
2.3.1. Homologous recombination and single strand annealing.....	8
2.3.2. Classical and alternative non-homologous end-joining	10
2.4. The Mre11:Rad50:Nbs1 (MRN) complex – a key player in DSB repair.....	11
2.4.1. Structural organization of the MR(N) complex.....	12
2.4.2. Functional insights into the MR(N) complex.....	15
2.4.3. Multiple roles of MRN in eukaryotes.....	17
2.4.4. Role of MR in prokaryotes.....	21
2.4.5. The bacterial MR catalytic head complex.....	22
2.4.6. Working model of MR’s DNA binding mechanism	24
2.5. Objectives.....	26
3. Materials and Methods.....	27
3.1. Materials.....	27
3.1.1. Oligonucleotides.....	27
3.1.2. Plasmids	29
3.1.3. Strains.....	31
3.1.4. Media and antibiotics	31
3.1.5. Preparation of sodium orthovanadate solution.....	31
3.2. Molecular biology methods.....	32
3.2.1. Molecular cloning	32
3.2.2. Site directed mutagenesis	33
3.2.3. Transformation of <i>E. coli</i>	34

3.3.	Protein biochemistry methods.....	34
3.3.1.	Protein expression in <i>E. coli</i>	34
3.3.2.	Purification of recombinant proteins.....	34
3.3.3.	Denaturing polyacrylamide gel electrophoresis (SDS-PAGE).....	37
3.3.4.	Dimerization of <i>TmMre11^{HLH}:Rad50^{NBD}</i>	37
3.3.5.	Analytical size exclusion chromatography.....	37
3.3.6.	Crosslinking via Bis-Maleimidoethane (BMOE).....	38
3.3.7.	Disulfide bridging via copper sulfate (CuSO ₄).....	38
3.4.	Structural biology methods.....	39
3.4.1.	Crystallization.....	39
3.4.2.	Data collection.....	41
3.4.3.	Structure determination, model building and refinement.....	41
3.4.4.	Small angle x-ray scattering.....	43
3.5.	<i>In vitro</i> activity assays of <i>Mre11:Rad50</i>	43
3.5.1.	ATP hydrolysis assay.....	43
3.5.2.	Electrophoretic mobility shift assay (EMSA).....	44
3.5.3.	Nuclease activity assay.....	45
3.5.4.	Endonuclease activity assay.....	45
3.5.5.	Protein-DNA encircling assay.....	46
3.5.6.	Antibody DNA binding assay.....	46
3.6.	Bioinformatic methods.....	47
3.6.1.	Structure based sequence alignment.....	47
4.	Results.....	48
4.1.	<i>Mre11^{HLH}:Rad50^{NBD}</i> of <i>T. maritima</i>	48
4.1.1.	Cloning and purification of <i>Mre11^{HLH}:Rad50^{NBD}</i>	48
4.1.2.	Crystallization and structure determination of <i>Mre11^{HLH}:Rad50^{NBD}:AMPPNP</i>	49
4.1.3.	Crystal structure of <i>Mre11^{HLH}:Rad50^{NBD}</i> bound to AMPPNP.....	51
4.1.4.	Crystallization and structure determination of <i>Mre11^{HLH}:Rad50^{NBD}:ADP[VO₄]³⁻</i>	55
4.2.	<i>Mre11:Rad50^{NBD}</i> of <i>T. maritima</i>	58

4.2.1.	Cloning and enzymatic characterization of Mre11:Rad50 ^{NBD}	58
4.2.2.	Analysis of Mre11:Rad50 ^{NBD} interface 2	60
4.2.3.	ATP induced engagement of Rad50 NBDs.....	62
4.3.	Mre11:Rad50 ^{NBD} of <i>T. maritima</i> trapped in its ATP/ADP bound state	65
4.3.1.	Crystallization and structure determination of Mre11:Rad50 ^{NBD (S-S)}	65
4.3.2.	Crystal structure of Mre11:Rad50 ^{NBD (S-S)} in its ATP/ADP bound state.....	69
4.3.3.	ATP induced conformational changes of Mre11:Rad50 ^{NBD}	71
4.3.4.	Anchoring and transient interfaces of Mre11:Rad50 ^{NBD}	74
4.3.5.	Analysis of Mre11:Rad50 ^{NBD (S-S)} in solution via small angle x-ray scattering	77
4.4.	Analysis of the DNA binding mechanism of <i>T. maritima</i> Mre11:Rad50	79
4.4.1.	DNA affinity of the Mre11:Rad50 ^{NBD} complex in the open and closed state	79
4.4.2.	DNA affinity of the single MR components	80
4.4.3.	Analyzing the molecular clamp mechanism of Mre11:Rad50 ^{NBD}	82
4.4.4.	Examination of DNA binding via surface analysis of Mre11:Rad50 ^{NBD}	85
5.	Discussion	88
5.1.	Two states of Mre11 ^{HLH} :Rad50 ^{NBD}	88
5.2.	Trapping ATP dependent NBD-NBD formation	91
5.3.	Mre11:Rad50 ^{NBD (S-S)} in its ATP/ADP bound state.....	92
5.4.	DNA binding mechanism of MR	95
5.5.	Interacting partners of MR(N).....	96
5.6.	Working model of MR for DNA tethering and DSB processing	98
6.	References	I
7.	Abbreviations	XIV
8.	Curriculum vitae.....	XVII
9.	Acknowledgements	XVIII

1. Summary

The integrity of the genome displays a central role for all living organisms. Double strand breaks (DSBs) are probably the most cytotoxic and hazardous type of DNA lesion and are linked to cancerogenic chromosome aberrations in humans. To maintain genome stability, cells use various repair mechanisms, including homologous recombination (HR) and non-homologous end-joining (NHEJ) pathways. The Mre11:Rad50 (MR) complex plays a crucial role in DSB repair processes including DSB sensing and processing but also tethering of DNA ends. The complex consists of the evolutionarily conserved core of two Rad50 ATPases from which a long coiled-coil region protrudes and a dimer of the Mre11 nuclease. Even though various enzymatic and also structural functions of MR(N) could be determined, so far the molecular interplay of Rad50's ATPase together with DNA binding and processing by Mre11 is rather unclear. The crystal structure of the bacterial MR complex in its nucleotide free state revealed an elongated conformation with accessible Mre11 nuclease sites in the center and a Rad50 monomer on each outer tip, thus suggesting conformational changes upon ATP and/or DNA binding. However, so far high resolution structures of MR in its ATP and/or DNA bound state are lacking.

The aim of this work was to understand the ATP-dependent engagement-disengagement cycle of Rad50's nucleotide binding domains (NBDs) and thereby the ATP-controlled interaction between Mre11 and Rad50. For this purpose high resolution crystal structures of the bacterial *Thermotoga maritima* (*Tm*) MR complex with engaged Rad50 NBDs were determined. Small angle x-ray scattering proved the conformation of the nucleotide bound complex in solution. DNA affinity was also analyzed to investigate MR's DNA binding mechanism.

ATP binding to *Tm*Rad50 induces a large structural change and surprisingly, the NBD dimer binds directly in the Mre11 DNA binding cleft, thereby blocking Mre11's dsDNA binding sites. DNA binding studies show that MR does not entrap DNA in a ring-like structure and that within the complex Rad50 likely forms a dsDNA binding site in response to ATP, while the Mre11 nuclease module retains ssDNA binding ability. Finally, a possible mechanism for ATP dependent DNA tethering and DSB processing by MR is proposed.

2. Introduction

2.1. DNA – history of the keystone of life

Deoxyribonucleic acid (DNA) was first discovered and isolated in 1869 by coincidence by the physician Friedrich Miescher. Since the isolated substance was located in the nuclei of the cell it was first called *nuclein* (Dahm, 2008). Almost ten years later, Albrecht Kossel started the investigation of nuclear materials and could isolate the non-protein component of the *nuclein* – consequently, due to its unusual acidic properties, called *nucleic acid* - and later on all five primary *nucleobases* (Jones, 1953). The importance of DNA as carrier of heritable information was first proposed by Frederick Griffith in 1928, soon after by Oswald Avery and coworkers in 1944 and finally confirmed in 1952 by Alfred Hershey and Martha Chase as they could show that DNA is the genetic material of the T2 phage (Avery et al., 1944; Hershey and Chase, 1952; Lorenz and Wackernagel, 1994). In 1953, James D. Watson and Francis Crick published the to date accepted double-helix model of DNA structures (Watson and Crick, 1953). To understand genome function, variation and evolution, and the information stored in DNA, sequencing projects started in the 1980s. A significant achievement was the 2.91 billion base pair (bp) consensus sequence of the euchromatin portion of the human genome (Venter et al., 2001).

2.2. DNA damage

The physiochemical organization of DNA does not provide for life-time stability. Environmental factors and normal metabolic processes cause between thousand and one million individual lesions per cell per day (Hoeijmakers, 2009). In fact, mutagenesis is a widespread fact of life, generating genetic diversity such as that in germ cells for Darwinian evolution. However, various severe diseases with fatal outcomes occur as a result of defective DNA damage repair pathways, illustrating that preventing mutational liability in somatic cells is as essential to life as the generation of a limited value of mutations in the germ line (Friedberg et al., 2004; Hoeijmakers, 2001).

DNA damage can occur spontaneously (endogenously) or exogenously, meaning it is environmentally derived. Endogenously derived DNA modifications are the primarily

source of DNA damages and include mutations caused by products of the normal cellular metabolism like reactive oxygen species (ROS), such as superoxide anions, hydroxyl radicals and hydrogen peroxide. ROS originate naturally from oxidative respiration and display products of lipid peroxidation. So far, over one hundred oxidative mediated modifications have been identified in DNA, including oxidized DNA bases and DNA breaks (Cadet et al., 2002; Hoeijmakers, 2001). Further endogenously derived damage may occur since some chemical bonds in the DNA, like the base-sugar N-glycosyl bond, are prone to hydrolysis (depurination, depyrimidination) leading to the release of free bases and therefore to abasic sites. Also spontaneously occurring hydrolytic deaminations of cytosine, adenine, guanine and 5-Methylcytosine can cause modifications resulting in the miscoding bases uracil, hypoxanthine, xanthine and thymine. Moreover, non-enzymatic alkylation of bases, usually methylation and often induced by S-adenosylmethionine (SAM), compromises the genome (Lindahl, 1993; Lindahl and Barnes, 2000). Finally, the process of replication is susceptible to errors leading to spontaneously derived DNA damage like mismatched base pairs and insertion or deletion in the range of one error per 10^{10} nucleotides synthesized (Jiricny, 1998).

Even DNA is damaged to a great part from within the cell exogenous sources for DNA modifications can also induce up to 10^5 lesions per cell per day (Hoeijmakers, 2009). Environmental agents derived from chemical or physical sources such as ionizing radiation, ultraviolet (UV) light, various genotoxic chemicals or carcinogens contained in foods and cigarettes can lead to alterations in DNA structure (Hoeijmakers, 2001; Jiricny, 1998).

The diversity and frequency of DNA modification illustrate the importance of a variety of repair mechanisms, like nucleotide-excision repair (NER), base-excision repair (BER), mismatch repair or repair pathways like homologous recombination (HR) and non-homologous end-joining (NHEJ). Their functionality is the basis to maintain genomic stability preventing cancer, aging or inborn diseases. Some of the common types of DNA damages and their repair mechanisms are summarized in Figure 1.

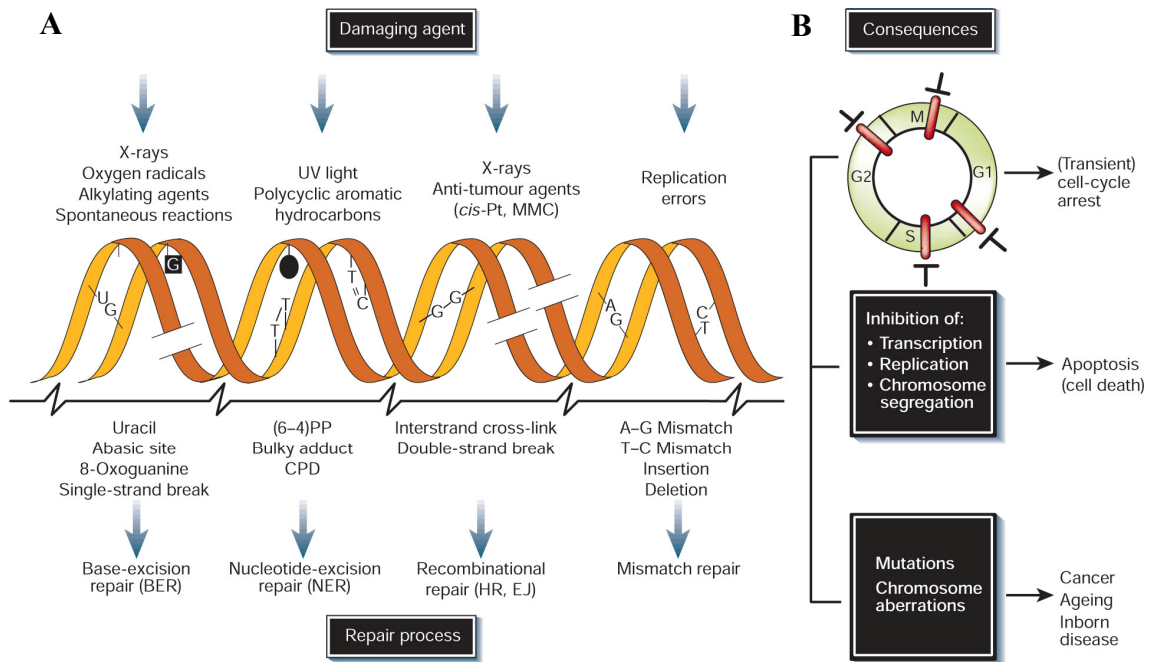


Figure 1: Simplified scheme of the correlation between DNA damaging agents, repair mechanisms and consequences of DNA damage, adapted from Hoeijmakers, 2001. (A) Endo- and exogenously occurring mutations lead to a variety of DNA damages. Corresponding DNA repair pathways are annotated. *Cis*-Pt and MMC, cisplatin and mitomycin C (both crosslinking agents); (6-4)PP and CPD, 6-4 photoproduct and cyclobutane pyrimidine dimer (both induced by UV light); HR, homologous recombination; EJ, end-joining. **(B)** DNA damage can lead either to transient cell-cycle arrest upon checkpoint control (upper panel), to cell death (middle panel), or long-term DNA damage (lower panel) if checkpoint control and repair are not functional.

2.2.1. DNA double strand breaks (DSBs)

Various types of endo- and exogenously derived DNA damage are able to occur within the cell, leading to genomic instability if not repaired correctly. One species that displays probably the most cytotoxic form of damaged DNA are double strand breaks (DSBs) (Khanna and Jackson, 2001). DSBs can arise directly from a diversity of exogenous sources, but they also occur indirectly for instance during the replication of single strand breaks (SSBs) or bulky lesions like pyrimidine dimers (Borde and Cobb, 2009). Contrariwise DSBs also play an important role in cellular metabolic processes where they are induced with intent (Khanna and Jackson, 2001). Thus, DSBs exhibit a dual role within a cell: as harmful lesions and important intermediates in cellular metabolism.

Directly and indirectly occurring DSBs from exo- and endogenous sources

DSBs can arise directly and indirectly from a variety of exogenous agents like ionizing radiation, genotoxic chemicals and UV light but also indirectly from endogenous sources like ROS.

Ionizing radiation (IR) appears naturally from environmental sources such as cosmic radiation but it can also arise as a result of medical procedures like x-ray examinations or radiation therapy in cancer treatment (Ciccia and Elledge, 2010). IR can damage DNA either directly by deposition of energy or indirectly via the formation of ROS. ROS, which can occur also endogenously, affect DNA molecules as cited before in several ways but amongst others lead to SSBs. Two or more SSBs on opposing strands within 10-20 bp cause in turn DSBs. Besides this, DSBs may occur when a replication fork crosses one single SSB present in the template strand, leading to a fork collapse (Kuzminov, 2001; Mahaney et al., 2009; Sutherland et al., 2000).

Chemical agents like camptothecin or its derivatives topotecan and irinotecan play a role in cancer therapy as topoisomerase (Topo) I inhibitors. These chemicals bind to the covalently fused TopoI-DNA complex and prevent religation of the transiently created SSBs. The accumulation of TopoI bound SSBs potentially lead indirectly to DSBs when a replication fork collides. Moreover TopoII inhibitors like etoposide act similar by trapping the cleavable TopoII-DNA complex and therefore preventing re-annealing of the transiently introduced DSB (Ciccia and Elledge, 2010; Degraasi et al., 2004).

In addition, UV light induced lesions like cyclobutane pyrimidine dimers and photoproducts or aromatic DNA adducts from cigarette smoke are assumed to cause indirectly DSBs at or close to stalled replication forks (Ciccia and Elledge, 2010; Hoeijmakers, 2009; Limoli et al., 2002).

DSBs in cellular processes

Beside the hazardous role of DSBs which compromises the integrity of the genome, DSBs have an impact on cellular processes as they display important intermediates. For instance the recombinational processes between homologous chromosomes in meiosis exhibit a significant role for the genetic diversity of sexually reproducing organisms (Edlinger and Schlogelhofer, 2011). Meiotic recombination is initiated in the first meiotic prophase by transiently formed DSBs which are catalyzed by the TopoII-like enzyme

Spo11 and facilitated by the Mre11:Rad50:Nbs1(Xrs2) complex. Most of the DSBs arise in hot spot intergenic regions, but also locations in coding sequences are reported. To guarantee the genetic diversity on the one hand and the genomic stability on the other hand, it is necessary to repair these DSBs in the course of meiosis by interaction with the unbroken homologous chromosome (see section 2.3.1) (Baudat and Nicolas, 1997; Borde, 2007).

In addition, the generation of genetic diverse T cell receptors (TCR) and B cell receptors (immunoglobulins) in vertebrates during early B and T lymphocyte development necessitate the recombination of Variable (V), Diversity (D) and Joining (J) encoding DNA segments (Dudley et al., 2005). During the process of V(D)J recombination, programmed DSBs are induced between the encoding gene sequences and a flanking recombination signal sequence (RSS) which is recognized and therefore cleaved by lymphocyte-specific RAG1 and RAG2 proteins. Further progress does need enzymes involved in end-joining repair pathways (see section 2.3.2) (Bassing et al., 2008; Perkins et al., 2002).

The final maturation of B lymphocytes proceeds upon antigen recognition in which B cells diversify their range of immunoglobulins (Ig) in a process called class switch recombination (CSR). The modification of Ig's leading to different isotypes takes place through the introduction of transient DSBs at large repetitive switch regions initiated by the activation-induced cytidine deaminase (AID). To ensure progress of CSR and assure the diversity in humoral response, religation of DSBs is required and relies on enzymes involved in end-joining repair pathways (see section 2.3.2) (Du et al., 2008; Dudley et al., 2005; Soulas-Sprauel et al., 2007).

Regardless if DSBs result due to exo- and endogenous agents or are introduced as intermediates on purpose to ensure genetic diversity in germ cells as well as cells of the immune system, repair of these breaks is indispensable to life.

2.3. DSB repair

The integrity of the genome is essential for all living organisms. As already mentioned, DSBs are one of the most cytotoxic and disruptive forms of DNA damages. They can result in broken chromosomes and therefore cell death if not repaired. On the

other hand, DSBs can lead to chromosome aberrations like translocations and therefore to genomic instability and diseases like cancer if repair proceeds inappropriate. Therefore sensing and repair of these life-threatening DSBs is critical for cell viability (Chu, 1997; Costanzo et al., 2001).

In normal cells, DSBs are recognized by different checkpoints, which control transient cell cycle arrest and activate DNA repair systems. In eukaryotic cells, DSBs are predominantly repaired by two major pathways: homologous recombination (HR) and classical non-homologous end-joining (c-NHEJ). The HR pathway is dependent on the existence of an intact sister chromatid as template, and is therefore relatively error free and almost exclusively activated in S- and G2-phase of the cell cycle (Ciccia and Elledge, 2010; Harper and Elledge, 2007). By contrast c-NHEJ is based on the rejoining and ligation of two broken DNA ends and potentially active throughout the entire cell cycle. C-NHEJ is the preferred pathway in G1-phase when no sister chromatid is available (Dudley et al., 2005; Mahaney et al., 2009). In addition, recently published data suggests that c-NHEJ is also the first choice pathway in G2-phase in mammalian cells and only if rapid rejoining does not occur, HR is promoted (Shibata et al., 2011). Since DNA ends on DSBs contain often non-ligatable groups, processing leads to either the loss or addition of nucleotides at the repair junction, making c-NHEJ potentially error-prone (Mladenov and Iliakis, 2011).

The relative importance of the two main repair pathways, HR and c-NHEJ, varies by organism and cell-type as well as cell-cycle stage. Whereas HR seems to be the major repair pathway in yeast cells, the majority of DSBs, including IR- and RAG-induced DSBs, are repaired by c-NHEJ in higher eukaryotes (Chu, 1997; Mahaney et al., 2009; Shibata et al., 2011).

In addition to HR and c-NHEJ, there are two extra pathways which are considered to repair DSBs, the microhomology-mediated end joining (MMEJ) which belongs to the alternative NHEJ (alt-NHEJ) pathway and the single strand anneling (SSA) process (Ciccia and Elledge, 2010; Wang et al., 2006).

2.3.1. Homologous recombination and single strand annealing

Homologous recombination is defined as the exchange of genetic information between allelic sequences and plays an important role in both mitosis and meiosis to maintain genomic integrity and stability of the organism karyotype. The mechanism of eukaryotic HR can be roughly divided in three different states: presynapsis, synapsis and postsynapsis (Figure 2B) (Heyer et al., 2010; San Filippo et al., 2008).

In the first stage, DSBs are detected and resected to form an extended 3' single stranded DNA end. The Mre11:Rad50:Nbs1 (MRN; MRX in *S. cerevisiae*) complex plays a crucial role in this by sensing and tethering the break but also in mediating the initiation of resection. Further proteins involved in human presynapsis are nucleases like CtIP (Sae2 in *S. cerevisiae*), Exo1 and Dna2, the helicase BLM (Sgs1 in *S. cerevisiae*) and the E3 ligase BRCA1 (Heyer et al., 2010; Huen et al., 2010; Nimonkar et al., 2011). To stabilize the single strand tail and to prevent formation of secondary structures the replication protein A (RPA) binds to the resected ssDNA end (San Filippo et al., 2008).

The synapsis stage includes a homology search and strand invasion between homologous DNA sequences induced by the Rad51 (RecA in bacteria) recombinase (New et al., 1998; Ogawa et al., 1993). The formation of the Rad51-DNA nucleoprotein filament and the displacement of RPA is carried out in the presence of so-called mediator proteins belonging to the Rad52 epistasis group. The nucleoprotein filament invades the homologous strand with the help of accessory proteins like the translocase Rad54 which induces superhelical stress in dsDNA. After removal of Rad51, the homologous sequence attaches the template strand by correct base-pairing, forming a so-called displacement loop (D-loop) (Sung and Klein, 2006). In meiosis, an additional recombinase, Dcm1 was found to play a role in DNA pairing and strand exchange (Heyer et al., 2010; San Filippo et al., 2008).

After DNA polymerase extension from the 3' end of the invading strand, the generated D-Loop can be resolved in postsynapsis by three different modes. First, the D-loop can be cleaved in a process called break-induced replication (BIR) which occurs in the absence of a second DSB end, e. g. at telomeres or at broken replication forks. Otherwise, when two DSB ends are present, the D-loop intermediate can be repaired either by synthesis-dependent strand annealing (SDSA) or double strand break repair (DSBR).

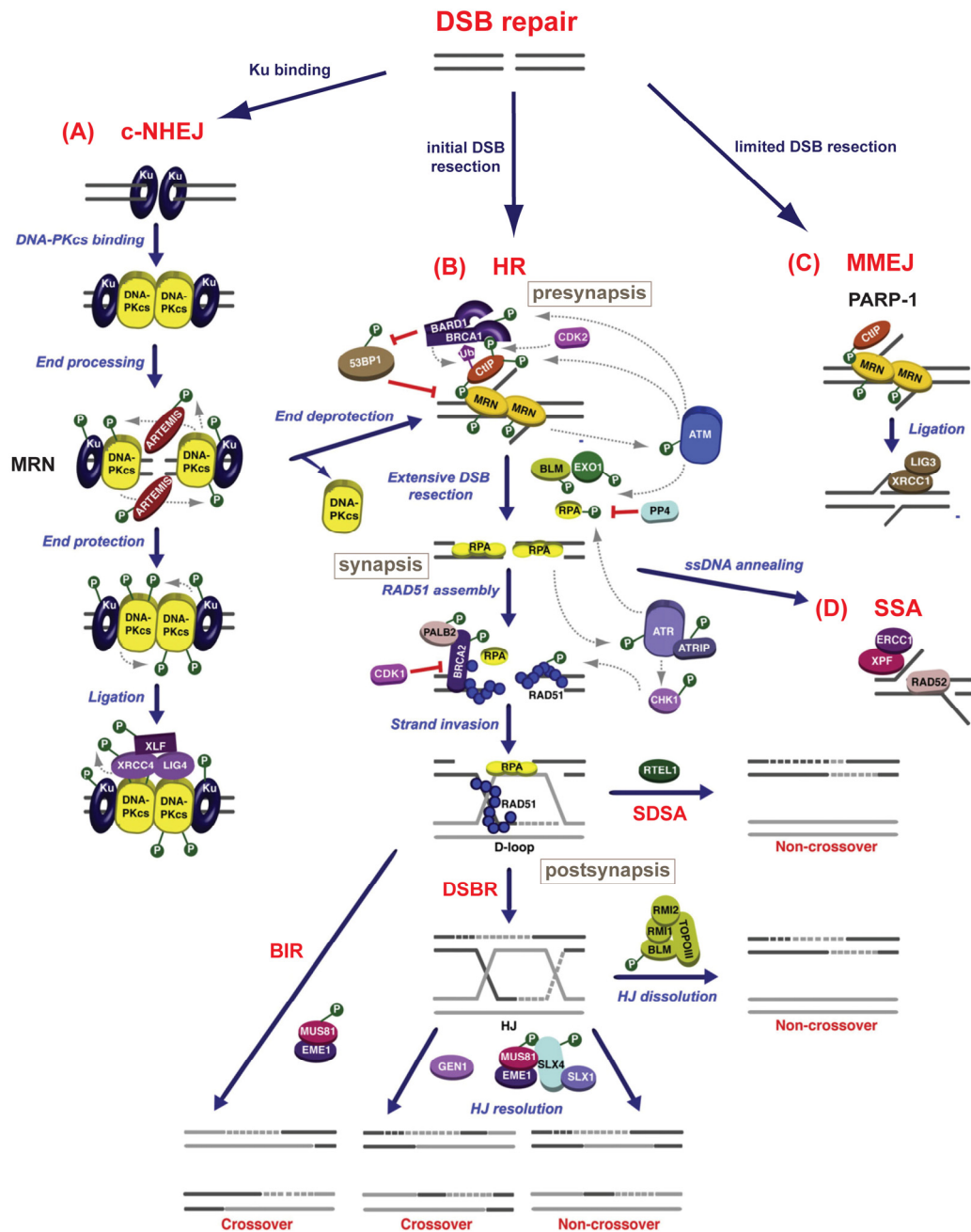


Figure 2: Schematic representation of pathways involved in eukaryotic DSB repair adapted from Ciccia and Elledge, 2010. (A) The classical NHEJ (c-NHEJ) pathway is initiated by binding Ku proteins to the DSB break. Recruitment of DNA-PKcs enables the initial processing by enzymes like Artemis. Ligation by the XRCC4/Ligase IV complex is stimulated by XLF/Cernunnos and attaches the two broken DNA ends, resulting in an rather error-prone repair. **(B)** The HR pathway is mediated by MRN which recruits various additional processing enzymes to ensure repair with the help of the homologous sister chromatid. The generated D-loop can be resolved in three different modes: break induced repair (BIR), double strand break repair (DSBR) and synthesis-dependent strand annealing (SDSA). These different subpathways lead to either crossover or non-crossover events or both. Involved proteins are annotated for the human orthologs. **(C)** Microhomology-mediated end-joining (MMEJ) is based on short microhomologies (1-4bp) and displays a backup system which seems to be rather error-prone than c-NHEJ. **(D)** Single strand annealing (SSA) is the most mutagenic pathway and is based on homologous repeat sequences which are located in direct orientation on both sides of the DSB.

In SDSA the invading 3' strand is displaced after its extension and re-anneals to the ssDNA end that was not involved in D-loop formation. Since this pathway restricts crossovers and therefore reduces the genetic variability it is predominant in somatic cells. Contrary to this, meiotic recombination mainly proceeds via the third so-called DSBR pathway. In this case, the 3' overhang which is not involved in D-loop formation gets annealed to the extended D-loop, therefore forming a structure designated as Holliday junction (Bzymek et al., 2010). Dependent on how the Holliday junction is resolved DSBR results in either crossover or non-crossover events or both (Ciccica and Elledge, 2010; Heyer et al., 2010; San Filippo et al., 2008).

Another homology-mediated recombinational repair pathway, known as single strand annealing (SSA), is well characterized in yeast but not in mammalian cells, although SSA has been identified as a significant pathway leading to translocations frequently inflicted in human cancers. The repair via SSA is carried out when two homologous (repeat) sequences are flanking each side of the DSB (Figure 2D). The DSB ends are first degraded in 5'-3' direction to form 3'tails like in HR. Subsequently the single stranded homologous sequences anneal and the non-complementary 3'ends are removed. As a result SSA is always correlated with a sequence deletion, therefore presenting the most mutagenic and for this reasons least attractive pathway for DSB repair in a cell (Ivanov et al., 1996; Mansour et al., 2008).

2.3.2. Classical and alternative non-homologous end-joining

The classical NHEJ (c-NHEJ) pathway starts with the detection and binding of the Ku70/80 heterodimer to DSB ends (Figure 2A). The potential function of Ku70/80 is to protect the DNA ends from unwanted processing or degradation, assistance in the tethering of broken ends and the recruitment or activation of damage repair enzymes (Dudley et al., 2005). After binding, Ku70/80 performs an inward translocation to allow a serine-threonine kinase, the catalytic subunit of a DNA dependent protein kinase (DNA-PKcs) to bind to the DNA end and Ku80. The DNA-PKcs interact with each other across the DSB and form the so-called synaptic complex which tethers and secures the DSB ends and stimulates the kinase activity of DNA-PKcs (Dudley et al., 2005; Mahaney et al., 2009). Since the ends of DSBs contain often non-ligatable groups, like ssDNA overhangs or damaged bases, processing enzymes are recruited to the break. Autophosphorylation of

DNA-PKcs leads to destabilization of itself with DNA and consequently enables the nuclease Artemis to bind and process on DSB ends (Ciccia and Elledge, 2010). Depending on the nature of the DSB other processing enzymes apart from Artemis can be involved in this repair pathway. These enzymes include DNA polymerase lambda (λ) and mu (μ) (Pol 4 in yeast), polynucleotide kinase (PNK) and most likely the Aprataxin and PNK-like factor (APLF) and the Werner's syndrome helicase (WRN). Subsequent to processing, DNA Ligase IV which exists in complex with XRCC4 (Dnl4 and Lif1 in yeast) is recruited to the end (Mahaney et al., 2009). XRCC4 depicts a scaffolding protein, which stabilizes and activates the function of the DNA Ligase IV. With the help of an additional stimulatory factor XLF (also known as Cernunnos; Nej1 in yeast), which interacts with XRCC4, the religation of the broken ends is carried out by the Ligase IV/XRCC4 complex (van Gent and van der Burg, 2007; Wang et al., 2006).

Mutants with defects in enzymes involved in c-NHEJ show declined repair activity, but nevertheless most DSBs are rejoined. This is assumed to occur by a slowly operating, alternative NHEJ pathway (alt-NHEJ) or also called Microhomology-mediated end-joining (MMEJ) (Figure 2C). The repair mechanism is based on a short junctional homology of 1-4bp, also designated as microhomologies. In this pathway, DSBs are most likely detected by PARP-1 (no yeast homolog) in association with DNA ligase III and possibly XRCC1. This backup system is rather more error-prone than classical NHEJ but appears to be efficiently used in class switch recombination (Lieber, 2010; Wang et al., 2006; Zha et al., 2009).

Finally, also MRN or MRN together with the nuclease CtIP is indicated to have an important function in the c-NHEJ and alt-NHEJ pathways, respectively, since a depletion of respective proteins reduced the end-joining efficiency up to 40% in mammalian cells (Rass et al., 2009; Xie et al., 2009).

2.4. The Mre11:Rad50:Nbs1 (MRN) complex – a key player in DSB repair

The Mre11:Rad50:Nbs1 (MRN; Mre11:Rad50:Xrs2 in *S. cerevisiae*; Mre11:Rad50 in prokaryotes) complex is a keystone complex, involved in early DSB detection, nucleolytic processing of DNA ends, recruitment of DSB processing enzymes and DNA damage signaling by activating the checkpoint kinase ATM. Furthermore, MRN acts as scaffolding protein by tethering DNA ends (Mirzoeva and Petrini, 2001). There are also

indications that the MRN complex could play a central role in bridging the recombinational and the NHEJ pathways in human cells (Yang et al., 2006). In any case complete deletion of either Mre11, Rad50, or Nbs1 leads to embryonic lethality in mice emphasizing the importance of MRN (Luo et al., 1999; Xiao and Weaver, 1997; Zhu et al., 2001). Moreover, hypomorphic mutations in the MRN-ATM axis are linked to human diseases like Ataxia-Telangiectasia (A-T, mutations in ATM) A-T like disorder (A-TLD, mutations in Mre11), the Nijmegen breakage sndrome (NBS; mutations in Nbs1) and NBS-like disorders (NBSLD, mutations in Rad50 or Mre11), respectively. All diseases show similar phenotypes including predisposition to cancer, mostly lymphomas, radiation sensitivity, immunodeficiency and neurological disorder. In addition, cells derived from patients show increased levels of spontaneously arising chromosomal aberrations or short telomeres (Carney et al., 1998; Petrini, 2000; Stewart et al., 1999; Uchisaka et al., 2009; Varon et al., 1998; Waltes et al., 2009). These findings stress the role of MRN as key player in the cellular response to double strand breaks and therefore the maintenance of genomic stability and cell viability.

2.4.1. Structural organization of the MR(N) complex

The multisubunit complex MR(N) is composed of the two core proteins Mre11 (meiotic recombination 11) and Rad50 (radiation sensitive) in prokaryotes and of a third component, Nbs1 (Nijmegen breakage syndrome, or its functional homolog Xrs2 in *S. cerevisiae*) which is only found in eukaryotes (Figure 3). Both, Mre11 and Rad50 are highly conserved in all three biological kingdoms and even exist in some viruses like the bacteriophage T4 (Herdendorf et al., 2011). The Mre11 dimer and the ABC ATPase domains of Rad50 form the catalytic head module. A large flexible helical region protrudes from the catalytic head module as indicated by electron and atomic force microscopy, linking the N- and C-terminal ABC segments of Rad50 (de Jager et al., 2001; Hopfner et al., 2002; Moreno-Herrero et al., 2005; Sharples and Leach, 1995; Stracker and Petrini, 2011). Nbs1, in contrast, is less sequence conserved and associated with the globular MR head module possibly in the course of evolutionarily diversification from prokaryotes to eukaryotes (Assenmacher and Hopfner, 2004).

Each Mre11 monomer consists of a conserved phosphodiesterase domain at the N-terminus that harbors a nuclease active site (also designated as nuclease domain) (Figure

3A1 and B). The five conserved phosphodiesterase motifs are located in loop regions connecting core β -sheets and are capable of coordinating two Mn^{2+} ions near the surface. Adjacent to the phosphodiesterase domain is a C-terminal DNA capping domain which comprises one of the two interaction regions for Rad50. A second interaction site could be identified on the C-terminal end of Mre11 (Bemeleit, 2007; Chamankhah and Xiao, 1999). Interaction of Nbs1 and Mre11 was first predicted by yeast-two-hybrid screening and then confirmed by structural analysis to occur via a eukaryotic insertion loop region situated in the nuclease domain (Desai-Mehta et al., 2001; Schiller, 2011). Beside Mre11's nuclease domain, studies on eukaryotic Mre11 revealed two potential DNA binding sites located in the C-terminal part of Mre11. Whereas the DNA interaction motif adjacent to the capping domain seems to be important for mitotic repair, the DNA motif on the C-terminal end was reported to play a role in DSB formation in meiotic recombination (Furuse et al., 1998; Usui et al., 1998). In addition the former DNA motif seems to be at least partially conserved in prokaryotes, as it was shown to be involved in forming DNA contacts as well in the archaeal *Pyrococcus furiosus* Mre11 (see section 2.4.6) (Williams et al., 2008). Additionally, the interaction of two phosphodiesterase domains and therefore the dimerization of Mre11 is critical for DNA binding and activity (Hopfner et al., 2001; Stracker and Petrini, 2011; Williams et al., 2008). Last but not least, the structural analysis of archaeal, bacterial and eukaryotic Mre11 proved the conserved morphology of the complex throughout all three biological kingdoms (Bemeleit, 2007; Hopfner et al., 2001; Schiller, 2011).

Rad50 resembles the structural maintenance of chromosomes (SMC) proteins, which are involved in chromatin condensation and chromosome cohesion and contains a bipartite ABC ATP binding cassette. The N-terminal part of Rad50 harbors the ATP binding Walker A motif, whereas the C-terminal part contains the ATP hydrolyzing Walker B and signature motifs (Figure 3A2 and B). The two ABC segments dimerize in a head to tail orientation upon ATP binding. In detail, each lobe I (mainly consisting of the N-terminal ABC segment) binds to lobe II (mainly consisting of the C-terminal ABC segment) of the opposing Rad50 molecule, therefore coordinating one ATP and one Mg^{2+} molecule (Hopfner et al., 2001; Hopfner et al., 2000b). Both, the N- and C-terminal segments are connected over a long antiparallel coiled-coil region which can be up to 500 Å in length in human Rad50 (Figure 3A2-3).

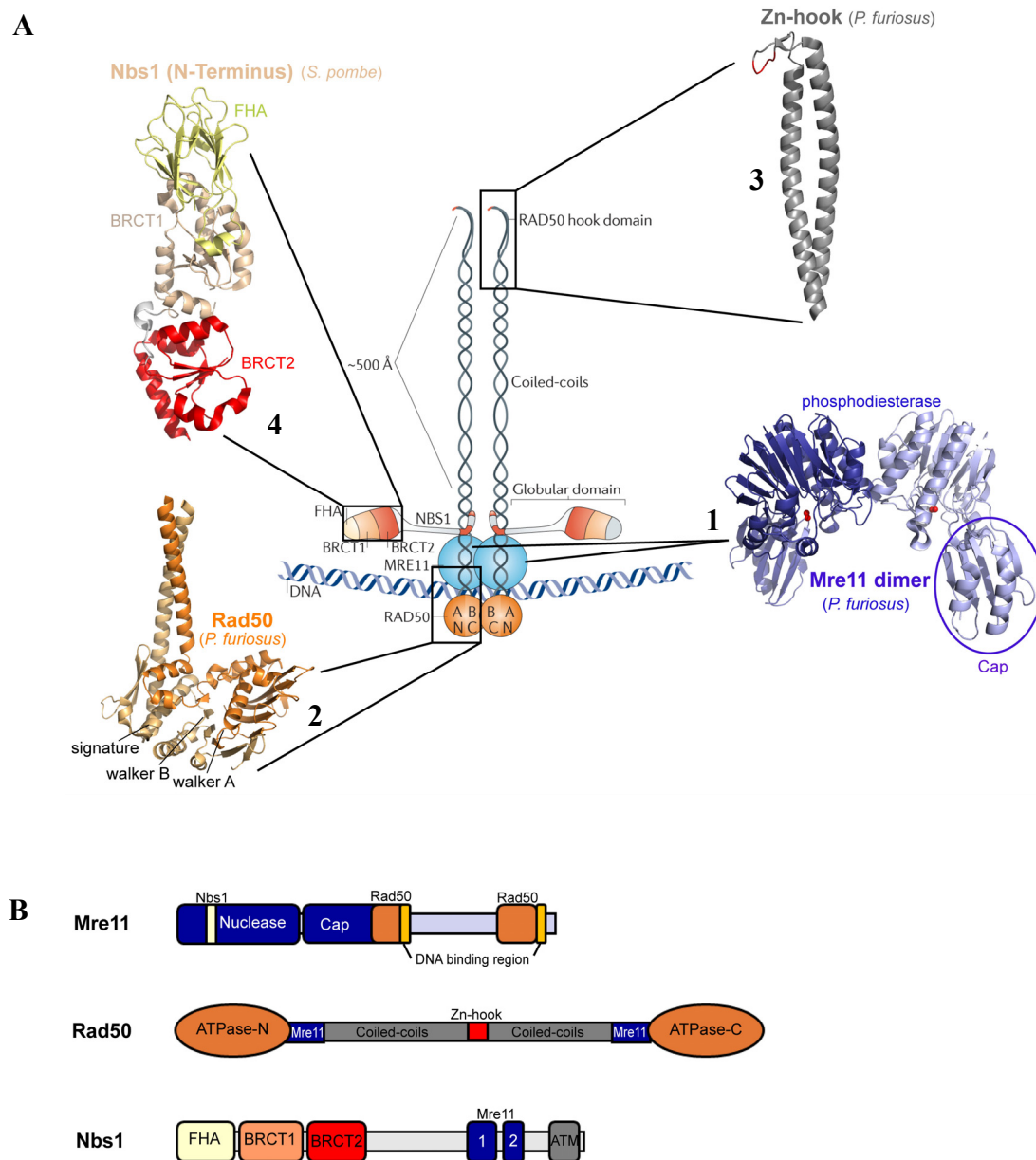


Figure 3: Schematic and structural overview of the Mre11:Rad50:Nbs1 complex. (A) Schematic overview of MRN adapted from Stracker and Petrini, 2011 including 3D structure representations of four crystallized domains (1-4). **(1-3)** Ribbon representation of the *P. furiosus* **(1)** Mre11 dimer (blue), consisting of the phosphodiesterase and flanking capping domains (PDB entry: 1II7), **(2)** N- and C-terminal (lobe I, orange; lobe II, sand) part of the Rad50 monomer (PDB entry: 1II8) and **(3)** of a Rad50 coiled-coil fragment (grey) containing the highly conserved Cys-X-X-Cys motif (red) (PDB entry: 1L8D). **(4)** Ribbon representation of the *S. pombe* N-terminal part consisting of FHA (yellow), BRCT1 (crème) and BRCT2 (red) domain (PDB entry: 3HUE). **(B)** Domain architecture of the individual MRN complex subunits. **Upper panel:** Mre11 consists of an N-terminal nuclease domain and an adjacent capping domain (blue). The Rad50 interaction regions (orange), the two proposed DNA binding sites (yellow) and the eukaryotic Nbs1 interaction region (crème) are highlighted. **Middle panel:** Rad50 ABC ATPase consisting of an N- and C-terminal ATPase segment (orange), connected by a long coiled-coil domain (grey). The center of the heptad repeats contains the CXXC motif (red) that forms a Zn-hook bridge between two neighbored coiled-coil domains. Mre11 binding sites are highlighted in blue. **Lower panel:** The N-terminus of Nbs1 consists of the FHA (crème) and BRCT1/2 (orange/red) domains and is connected via an unstructured linker with Mre11 interaction region 1 and 2 (blue) and an ATM binding domain (grey).

The two coiled-coil domains contain a highly conserved Cys-X-X-Cys (CXXC) motif in the center of the heptad repeats that folds into a Zn-hook motif. Therefore, Rad50 is able to form dimers on the basis of a second dimerization site, via coordinating a Zn^{2+} ion by four conserved cysteine residues to form a flexible bridge of up to 1000 Å (Stracker and Petrini, 2011). Mutations in the conserved cysteine residues disrupt the interaction of Mre11 and Rad50, suggesting a conformational cross-talk between Rad50's Zn-hook and the Mre11:Rad50 globular head domain (Hohl et al., 2011; Hopfner et al., 2002). Rad50 was found to interact with Mre11 upon its upper coiled-coil domain, including segments of the N- and C-terminal ATPase region (Bemeleit, 2007; Williams et al., 2011). Further interaction sites are possible, yet remain to be investigated.

Nbs1 is the least conserved component of the eukaryotic MRN complex (Figure 3A4 and B). The N-terminal region of Nbs1 consists of a forkhead-associated (FHA) domain and two (tandem) breast cancer carboxy-terminal (BRCT) domains which are primarily considered to be interaction sites for phosphoproteins like CtIP, and are known to be elements of other proteins involved in DNA damage response and cell cycle checkpoint control (Desai-Mehta et al., 2001; Durocher and Jackson, 2002; Williams et al., 2009). The C-terminal part of Nbs1 contains a rather unstructured linker connecting the FHA/BRCT domain with two Mre11 interacting regions and an ATM interaction site (Schiller, 2011). Taken together, Nbs1 seems to be the connecting link between the Mre11:Rad50 core, the checkpoint kinase ATM (Tel1 in *S. cerevisiae*) and the DSB processing enzyme CtIP (Sae2 in *S. cerevisiae*) (Williams et al., 2009).

2.4.2. Functional insights into the MR(N) complex

Biochemical *in vitro* studies on pro- and eukaryotic MR(N) revealed three basic activities for Mre11: endonucleolytic cleavage of single stranded DNA, DNA hairpin opening and exonucleolytic degradation of double stranded DNA in 3'-5' polarity. All three activities require Mn^{2+} and cannot be replaced by other divalent ions like Mg^{2+} , Fe^{2+} or Co^{2+} (Connelly et al., 1997; Connelly and Leach, 1996; Paull and Gellert, 1998; Trujillo et al., 1998). Hairpin opening and exonucleolytic activity, the latter one at least in prokaryotes, was shown to be stimulated by ATP binding. Although Mre11 acts as an endonucleolytic enzyme on single stranded DNA its activity is suggested to require double stranded DNA ends, hence the opening of hairpins occurs by nicking the dsDNA part 5' to

the ssDNA region (Connelly et al., 1999). Finally, MR(N) is able to remove 15-55 nucleotides (nt) 5' to DSBs in an ATP dependent manner resulting in 3' single strand tails therefore possibly disrupting covalent protein-DNA interactions on DSBs *in vivo*, such as removing of Spo11 in meiosis (see section 2.4.3) (Connelly et al., 2003; Hopkins and Paull, 2008).

The role of Rad50's ATPase function has been unclear, although it is essential for MR(N) function (Waltes et al., 2009). ATP binding was identified to play a role in Mre11's nuclease activity as described above. Furthermore, the appearance of 3' single strand ends generated by removal of 15-55 nt 5' to DSBs could occur due to a dual role of endonucleolytic cleavage and partial melting and unwinding on the basis of Rad50's ATP binding and hydrolysis activity (Hopkins and Paull, 2008; Paull and Gellert, 1999). It has been proposed that Rad50 could also operate as an adenylate kinase *in vivo* (Bhaskara et al., 2007). Nevertheless, a Rad50 signature motif mutant, which lacks the ability to bind ATP, loses the capability to stimulate the checkpoint kinase ATM *in vivo* (Lee and Paull, 2005), making it necessary to learn more about the structural framework of the catalytic head and therefore the role of Rad50's ATPase.

Besides the enzymatic functions of Mre11 and Rad50, the complex comprises also non-enzymatic, architectural features based on Rad50's coiled-coil domain (Hopfner et al., 2002). A structural function of MR(N) was suggested as nuclease-inactivating mutations in Mre11 did not impair most forms of DSB repair in mitotic cells. Moreover, the Rad50 hook domain was shown to be critical in telomere maintenance and for induction of Spo11 dependent meiotic DSB formation (Hohl et al., 2011; Wiltzius et al., 2005). In addition, MRX increased the ligation rate of linear DNA ends in c-NHEJ, suggesting a role for MRN as end-bridging factor (Chen et al., 2001). Scanning force microscopy analysis of human and prokaryotic MR(N) support these genetic studies. Intramolecular coiled-coil interaction seems to alter upon DNA binding, leading to either a structure where the coiled-coils are oriented in parallel or to a intermolecular bridging interaction based on the Zn-hook (Figure 4) (Moreno-Herrero et al., 2005; van der Linden et al., 2009). Summing up, MR(N) seems to have a major role in enforcing physical proximity of DNA ends, moreover the recombinational repair achieved by MR(N) in mitotic and meiotic cells seems to be primarily structural (Stracker and Petrini, 2011).

Nbs1 possesses no enzymatic activity on its own but rather it plays an important role in mediating between the MR core complex and the signal checkpoint protein kinase ATM and in recruiting other processing enzymes involved in DSB repair like CtIP. Nbs1 also regulates the MR(N) complex, stimulating DNA binding and Mre11's nuclease activity (Lee et al., 2003; Paull and Gellert, 1999; Schiller, 2011).

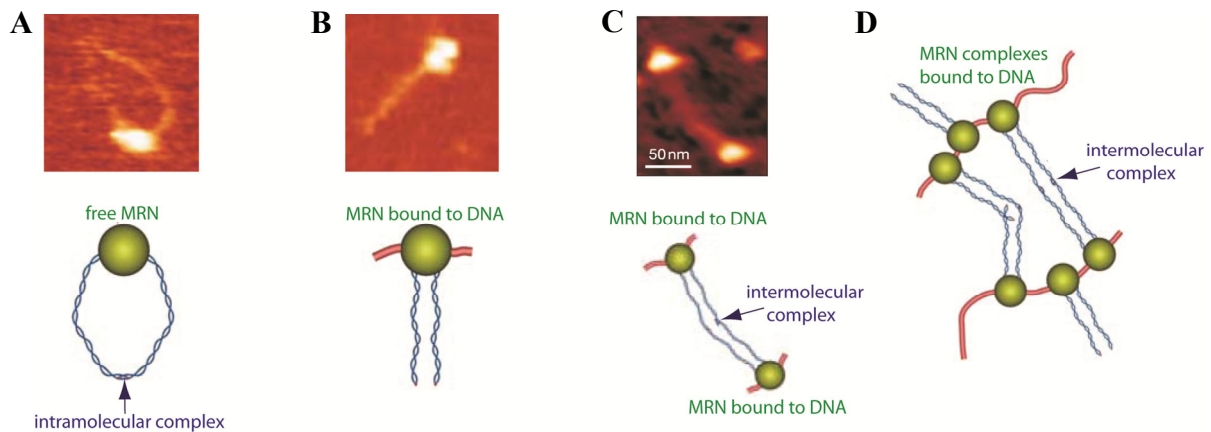


Figure 4: Atomic force microscopy (AFM) of human MRN adapted from Moreno-Herrero et al., 2005. (A) AFM images and schematic model of free MRN shows intramolecular coiled-coil interaction within the complex. (B) AFM images and schematic model of MRN upon DNA binding shows long, parallel oriented coiled-coils or (C) intermolecular coiled-coil interaction. (D) The observed conformational changes are important for DNA-end tethering.

2.4.3. Multiple roles of MRN in eukaryotes

The multitude of features of the MR(N) complex, including enzymatic but also structural roles and the impact of MRN on genome stability, perceivable in various diseases like A-TLD, emphasizes MR(N)'s importance in various processes like DNA metabolism (DSB repair, meiosis, replication), telomere maintenance, immune system development and checkpoint signaling.

MRN in DNA metabolism

For the role of MRN in meiotic recombination various important indications have emerged from studies in *S. cerevisiae*. The essential step in meiosis is the insertion of DSBs catalyzed by Spo11. This initial process is facilitated by MRN in a nuclease independent way (Furuse et al., 1998; Keeney et al., 1997). Subsequent to cleavage, Spo11

remains covalently bound to the 5' strands flanking the DSB and is not released until MRN endonucleolytically cleaves and removes Spo11-DNA oligonucleotides from the DSB site, resulting in an 3' overhanging structure (Neale et al., 2005; Usui et al., 1998). Furthermore, Spo11 removal is Sae2/Com1 dependent and interaction could possibly occur via Rad50 on DNA. Despite this proposal, a direct interaction of MRN and Sae2 could not be observed *in vitro* (Keeney and Neale, 2006; Lengsfeld et al., 2007; Stracker and Petrini, 2011). Additionally, MRN does stimulate the recruitment of DSB processing enzymes like Exo1 (Zakharyevich et al., 2010). Consequently, MRN seems to display a ternary role in meiosis, by: (1.) facilitating DSB cleavage via Spo11, (2.) removal of Spo11 from DSB sites and (3.) stimulating the recruitment of DSB processing enzymes.

Furthermore, the nuclease activity of Mre11 could play a role in dissolving covalently formed topoisomerase 1 and 2 intermediates. This suggestion is based on MRN's function in Spo11 removal and its sensitivity to topoisomerase poisons when Mre11's nuclease is deficient (Stracker and Petrini, 2011).

Considering the DNA tethering feature of MRN it is likely that MRN is one of the early, if not the first, factors in sensing DSBs, emphasizing MRN's role in recombinational repair. The scaffolding function of MRN links homologous chromosomes and prevent their separation during repair (Borde and Cobb, 2009; Hopfner et al., 2002). In *S. cerevisiae*, where the mechanistic details of resection are probably best understood, MRN together with Sae2 is suggested to catalyze the first resection at DSB sites by removal of a short ssDNA fraction, resulting in a short 3' ssDNA tail. Continulative resection, which is required for efficient induction of G2 arrest as well as SSA or HR repair, is carried out either by Exo1 or Dna2 together with the helicase Sgs1. Recruitment of processive nuclease/helicase complexes seems to be, at least in *S. cerevisiae*, stimulated by MRN whereas bulk resection is likely to be independent of MRN's enzymatic function (Shim et al., 2010; Stracker and Petrini, 2011). In mammals, MRN together with CtIP (orthologue of Sae2) is supposed to facilitate analogous function in DSB resection. Whereas Sae2 *in vitro* shows a nuclease activity on its own, such a function couldn't be demonstrated for CtIP and Ctp1 (CtIP orthologue in *S. pombe*), therefore possibly acting as co-factor for MRN (Lengsfeld et al., 2007; Limbo et al., 2007). The initial generation of 3' ssDNA tails by MRN and CtIP in mammalian cells was shown to affect Ku70/80 binding to the DSB, main sensor of DSBs in c-NHEJ. Recently reported data of *S. pombe* also suggest a role of Mre11's nuclease activity and Ctp1 in the release of Ku70/80 (Langerak et al., 2011),

supporting an antagonistic role of MRN and Ku70/80. It is also known that HR is suppressed by Ku via inhibition of MRN, but inhibition mainly takes place in G1 and less in G2/S-phase when sister chromatids are not available, consistent with the fact that MRN is also involved in different NHEJ pathways (Dudley et al., 2005; Stracker and Petrini, 2011). However, the importance of the first resection step in which MRN together with Sae2/CtIP/Ctp1 is active and the regulation of the different pathways is still poorly understood and needs to be investigated.

Finally, MRN has an important function during the process of DNA replication, even though its role is less characterized than in homologous recombination. MRN is proposed to maintain genomic stability during replication by at least three different modes. First, MRN seems to prevent fork associated damage during ordinary replication and under stress. Second, MRN is presumably required in a nuclease-dependent manner to activate ATM upon replication stress promoting HR-mediated fork restart. Third, the scaffolding function of MRN could preserve the fork in its conformation to ensure progression during replication pauses (Borde and Cobb, 2009; Stracker and Petrini, 2011).

MRN in telomere maintenance

The MRN complex is proposed to represent at least two different functions in telomere homeostasis in mammals. First, MRN seems to be involved in telomere resection of the leading strand after replication resulting in a 3' ssDNA tail. This 3' single strand overhang is important to impair c-NHEJ and it is required to form the t-loop, a structure critical for telomere protection and maintenance. MRN is also proposed to play a role in sensing dysfunctional telomeres, leading to activation of ATM and DSB repair by c-NHEJ, resulting in telomere end-joining and thus in loss of chromosome segregation, therefore causing cell death. MRN could also be involved in degradation of the 3' overhang at dysfunctional telomeres to allow c-NHEJ but this suggestion has not been proven so far (Deng et al., 2009; Stracker and Petrini, 2011). In general, the scaffolding function of MRN seems to play a crucial role in telomere maintenance as illustrated in 2.4.2. In contrast to mammals, MRN has an impact on telomere length in *S. cerevisiae*, by recognizing short telomeres and recruiting the enzyme telomerase via Tel1 (ATM homologue) (Sabourin and Zakian, 2008).

MRN in immune system development

Although MRN is not a key player for mammalian c-NHEJ, it is crucial for V(D)J recombination, which is strongly dependent on c-NHEJ (Deriano et al., 2009; Helmink et al., 2009). Furthermore, hypomorphic mutations in Nbs1, which cause the Nijmegen breakage syndrome, results in aberrant immunoglobulin isotype profiles in serum and reduced numbers of mature T cells. Mre11 nuclease deficient mice indicated a dual role for MRN in class switch recombination: (1) as essential component by catalyzing the resection at DSBs to generate ends with compatible microhomology sequences and (2) to activate ATM. In contrast, c-NHEJ seems to be independent of Mre11's nuclease activity. MRN is also thought to play an important role in c-NHEJ by activating ATM and possibly as scaffolding protein (see section 2.4.2) (Dinkelman et al., 2009; Rahal et al., 2010; Rass et al., 2009; Stracker and Petrini, 2011). Nevertheless, it will be essential to elucidate the precise role for MRN in both V(D)J and class switch recombination.

MRN as mediator in checkpoint signaling

MRN not only plays a role in sensing and resection of DSBs or as scaffolding protein, but also in the mediation of checkpoint signaling, therefore controlling repair, cell-cycle arrest and apoptosis (in metazoa) in response to DSBs by recruiting the cell cycle checkpoint phosphoinositide-3-kinase-related protein kinase (PIKK) ATM (Tel1 in yeast). In undamaged cells, ATM exists as an inactive dimer until it is activated by autophosphorylation followed by dimer dissociation, resulting in an active ATM monomer (Bakkenist and Kastan, 2003). The active monomer interacts with a conserved C-terminal sequence motif of Nbs1. This interaction is proposed to take place at DSB sites, since DNA binding by MRN enhances the affinity for ATM. But there is also evidence that ATM and MRN arrive at DSB ends as pre-assembled complex. The exact function of the MRN complex in controlling ATM activation is not fully understood. There are contrary results about the action of MRN in DSB induced autophosphorylation and activation of ATM (Falck et al., 2005; You et al., 2005). However, once activated and recruited to DSB sites by the sensor MRN, ATM acts as transducer and mediates in turn the phosphorylation of several important effector proteins, such as SMC1, Nbs1, Chk2 and histone H2AX. The generated circuit of phosphorylation between sensor, transducer and effector proteins promotes both DNA damage checkpoint signaling as well as accumulation of repair

proteins at DSBs and covalent marking of chromatin during break (Williams et al., 2007; You et al., 2005).

2.4.4. Role of MR in prokaryotes

The prokaryotic MR complex, also identified as SbcD (Mre11) and SbcC (Rad50) in bacteria, shares not only sequence similarities and morphological features with the eukaryotic system, it also displays almost identical enzymatic activities *in vitro* (Bemeleit, 2007; Connelly et al., 1997; Connelly and Leach, 1996; Hopfner et al., 2001; Hopfner et al., 2000a; Paull and Gellert, 1998; Schiller, 2011; Sharples and Leach, 1995; Trujillo and Sung, 2001).

Interestingly, and contrary to eukaryotes (and bacteriophage T4), there is no evidence that bacterial MR is directly involved in generating 3' ssDNA tails in DSB repair necessary for homologous recombination. For that, bacterial cells possess an additional system, called RecBCD. MR and also ExoI are suggested to participate indirect in the RecBCD-catalyzed degradation process, eventually by blunting DNA ends, and thus preparing a substrate for RecBCD. It is not clear if both ExoI and MR act as 3'-5' exonuclease on ssDNA overhangs or if MR shortens 3' overhangs indirect by cleaving hairpin-like structures present in ssDNA. So far, just the efficient degradation of hairpin structures could be demonstrated for the bacterial system *in vitro* and *in vivo*, even though weak degradation of 3' ssDNA tails could be reported for eukaryotic MR(N) (Connelly et al., 1999; Paull and Gellert, 1998, 1999; Zahradka et al., 2009). Moreover, bacterial MR has been directly implicated in genomic stability by elimination of palindromic sequences during replication. Together with RecA, MR was shown to process DNA hairpin structures which arise upon spontaneous DSB formation close to palindromic sequences (Connelly and Leach, 1996; Darmon et al., 2010). Bacterial MR was also shown to act in interstrand-crosslink repair and removing proteins bound to DNA (see section 2.4.2) (Mascarenhas et al., 2006). Besides the HR pathway, a possible bacterial c-NHEJ pathway for DSB repair and MR association needs to be investigated, even though homologs of Ku70/80 in combination with ATP-dependent DNA ligases were found in various species (Cromie et al., 2001).

The archaeal Mre11:Rad50 complex is expected to play a key function in DNA metabolism pathways similarly to the bacterial and eukaryotic homologs, but so far there is no genetic evidence. HR is assumedly the preferred pathway for DSB repair in archaea as homologs for c-NHEJ Ku70/80 were not found in most species. There are no RecBCD homologs in archaea suggesting that Mre11:Rad50 exhibit equivalent functions in the first steps of HR like in eukaryotes. MR is linked in almost all thermophilic archaea to a 3'-5' nuclease called HerA and the helicase NurA which could carry out the initial resection together with MR in HR (Constantinesco et al., 2004; Hopkins and Paull, 2008).

The conservation of Rad50 and Mre11 morphological features and enzymatic activities in all three biological domains, makes the prokaryotic MR complex an ideal candidate for structural as well as biochemical analysis.

2.4.5. The bacterial MR catalytic head complex

Structural analyses of the bacterial Mre11:Rad50 complex have shed more light on its functional characteristics and on the interplay between the nuclease and ATPase subunits of the complex. The crystal structure of the MR catalytic head domain from the thermophilic bacteria *Thermotoga maritima* (*Tm*) has been determined in the ATP-free state (Bemeleit, 2007; Lammens et al., 2011). Unexpectedly, the MR catalytic head is an elongated crescent shaped complex with approx. 60Å x 70Å x 210Å dimensions (Figure 5). Its core is formed by a dimer of the two Mre11 nuclease domains whereas the Rad50 nucleotide binding domains (NBDs) attach to the outside of the nuclease dimer and form the tips of the crescent. The Rad50 coiled-coils protrude from the convex side of the catalytic head, opposite the nuclease active sites. As a result, the angle between the coiled-coils in the nucleotide free conformation is approx. 120°. This architecture fits well the bipolar shapes of full prokaryotic MR and eukaryotic MRN complexes previously visualized by electron and atomic force microscopy (Connelly et al., 1998; de Jager et al., 2001; Hopfner et al., 2001). The NBDs of Rad50 possess the typical ABC ATPase segments, while Mre11 is composed of two functional nuclease modules, consistent of phosphodiesterase and accessory DNA binding capping domain, and the Rad50 binding domain. The Rad50 binding domain contains a helix-loop-helix (HLH) domain that binds to the root of Rad50's coiled-coil (designated as interface 1). The nuclease module and the HLH domain are widely separated and connected by a long, poorly structured linker, that

wraps around Rad50's NBD therefore placing the capping and HLH domains of Mre11 on opposite sites. A second interaction is formed between Mre11's capping domain and the C-terminal part of Rad50's NBDs (designated as interface 2), stabilizing the observed extended domain arrangement between Mre11 and Rad50 in the catalytic head. Finally, small ange x-ray scattering (SAXS) analysis of the bacterial MR complex in solution could verify the elongated shape of the complex in the nucleotide free state (Bemeleit, 2007).

The overall structure explains two functional characteristics of MR which were poorly understood so far. The widely separated Rad50 NBDs allows unobstructed access of DNA to the Mre11 active sites, even if DNA ends are blocked by large proteins. In addition, the structure shows that MR has the potential to undergo major conformational changes, consistent with the observation of large conformational changes identified by scanning force microscopy of human MRN (Moreno-Herrero et al., 2005).

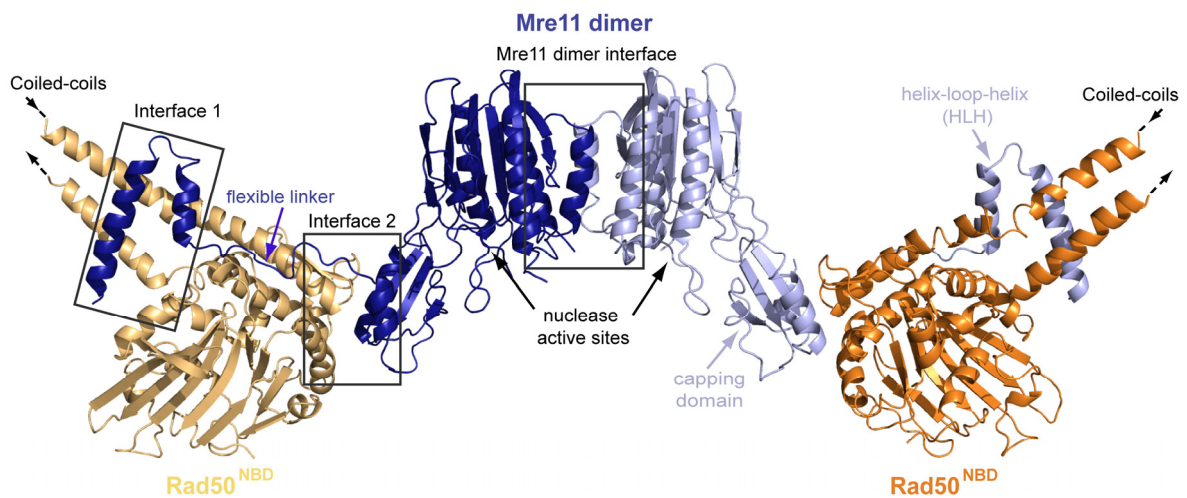


Figure 5: *T. maritima* Mre11:Rad50 catalytic head complex structure in its ATP-free state adapted from Lammens et al., 2011. The catalytic head module of the bacterial MR complex shows an elongated, crescent shape in the absence of ATP. The center of the head module is formed by the Mre11 dimer which binds a Rad50 monomer on each side therefore forming the tips of the crescent. Individual domains and important motifs are highlighted and annotated.

2.4.6. Working model of MR's DNA binding mechanism

Besides *in vivo* analysis of potential DNA binding sites in eukaryotes (Furuse et al., 1998; Usui et al., 1998), structural analysis of archaeal Mre11 bound to DNA revealed new insights into a possible DNA binding mechanism. The crystal structure of dimeric Mre11, including phosphodiesterase and capping domain from the thermophilic archaeon *Pyrococcus furiosus* has been determined bound to two different DNA's, so-called synaptic and branched complex (Figure 6A and B) (Williams et al., 2008).

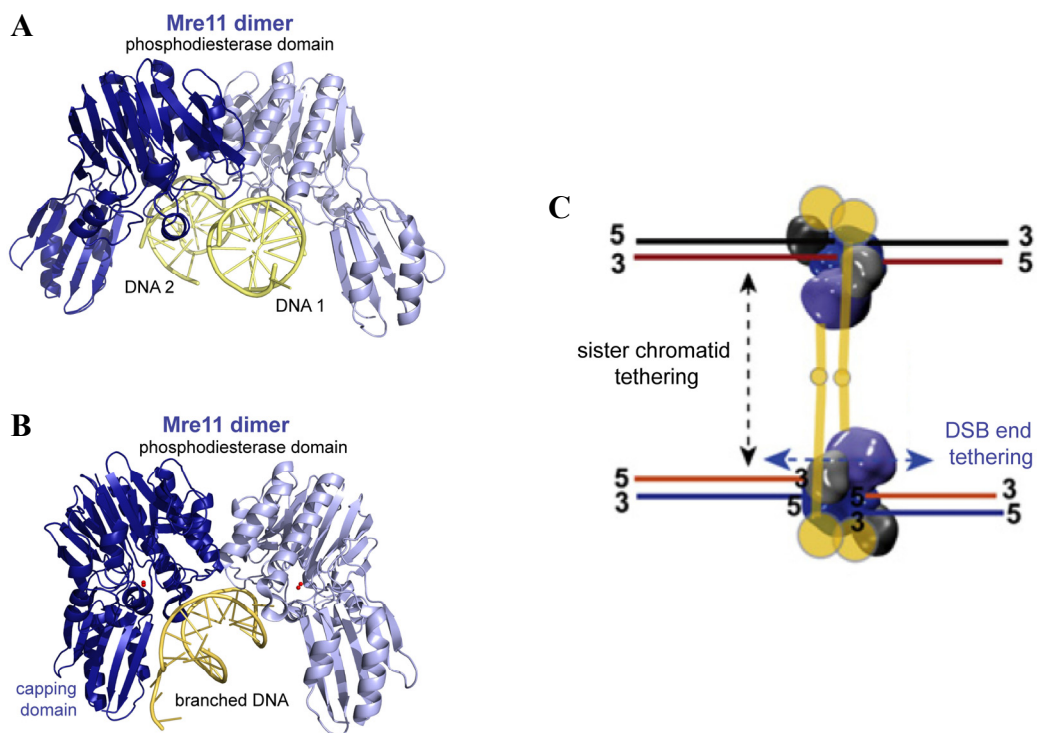


Figure 6: *P. furiosus* Mre11 dimer bound to DNA and hypothetical DNA bridging model adapted from Williams et al., 2008. (A) Mre11 dimer bound to synaptic DNA indicate symmetrically bound dsDNA ends. Synaptic DNA ends are designated as DNA 1 and DNA 2. **(B)** Mre11 dimer bound to branched DNA. The ssDNA-dsDNA junction is bound asymmetric by Mre11 dimer and capping domain interactions. **(C)** Presumed model of MR bridging short-range and long-range DNA ends. Mre11 phosphodiesterase dimer colored in blue, Mre11 capping domain colored in black, and Rad50 colored in orange.

Whereas the synaptic complex is mimicking two DSB ends arising upon DNA damage, the branched complex (ssDNA-dsDNA junction) could represent a DNA structure occurring at a collapsed replication fork. The synaptic DNA is bound symmetrically by Mre11, meaning one dsDNA end to each nuclease domain. In contrast the ssDNA-dsDNA junction

is bound asymmetrically, implicating the capping domain in ssDNA binding of branched DNA. Nevertheless, both DNA's illustrate analogous but not equivalent core DNA binding contacts. In addition, at least some of the DNA-Mre11 binding contacts are conserved to the predicted DNA binding motif in *S. cerevisiae* (Usui et al., 1998; Williams et al., 2008).

Based on the structural insights of Mre11's DNA binding site it is conceivable that upon ATP binding MR encloses DNA in a ring shape conformation (Figure 6C). Therefore the MR complex could keep two opposed short-range DSB ends in close proximity but also link sister chromatids by Rad50 hook-dependent long-range tethering. Taken together, it seems like the MR complex harbors flexible and diversified DNA-bridging capabilities and makes use of distinct modes of long-range and short-range DNA tethering to sense, coordinate, process, and allows access for variable DNA ends to repair proteins involved in HR (Williams et al., 2008).

2.5. Objectives

The MR complex plays a crucial role in many processes including DSB sensing and repair processing. Even though various enzymatic and also architectural functions have been determined for the MR complex in *vitro* and *in vivo*, the functional interplay and actual working mechanism has been unclear so far. Besides the controversial role of Rad50's ATPase function it is unknown why DSB recognition by MR(N) has no clear biochemical preference for DNA ends or hairpins and binds DNA also at internal sites. Moreover Mre11's endonuclease activity was shown to play a crucial role in MR's functionality whereas the 3'-5'-exonuclease activity seems to have a rather dispensable role (Williams et al., 2008). Even though the catalytic head of the bacterial MR complex could be determined in its ATP-free state only low resolution images indicate gross conformational rearrangements upon ATP and/or DNA binding.

Therefore the aim of this work was to analyze the interplay and the conformational changes of the prokaryotic Mre11:Rad50 complex upon ATP and/or DNA binding. To this end, it was an ambition to determine a high resolution structure of the bacterial *Thermotoga maritima* (*Tm*) Rad50 nucleotide binding domain bound to an ATP analog and besides this, the structure of the complete *Tm*Mre11:Rad50 catalytic head domain in its nucleotide bound state. High-resolution crystal structures were combined with small-angle x-ray scattering data to clearly define the conformation of the nucleotide bound MR complex in solution. In addition, to understand MR's DNA binding mechanism in more detail, the precise study of its DNA affinity was also necessary.

3. Materials and Methods

3.1. Materials

All chemicals used in this work were of the highest available grade obtained from Sigma-Aldrich (Deisenhofen), Carl Roth (Karlsruhe), or Merck (Darmstadt), unless otherwise stated. Enzymes for molecular biology were purchased from Fermentas (St. Leon-Rot) or New England Biolabs (Frankfurt). HPSF purified oligonucleotides for molecular cloning and RP-HPLC purified oligonucleotides for *in vitro* activity assays were obtained from Eurofins MWG Operon (Ebersberg) and Thermo Fisher Scientific (Ulm), respectively. Chromatographic media and columns were purchased from GE Healthcare (Munich). Crystallization screens and tools were from Hampton Research (Laguna Niguel, USA), NeXtal (QIAGEN; Hilden), and the Max-Planck-Crystallization Facility (Martinsried).

3.1.1. Oligonucleotides

Table 1: DNA oligonucleotides used for molecular cloning and site directed mutagenesis. Recognition sites of restriction endonucleases are underlined. Bold nucleotides correspond to added sequences encoding linker regions, affinity tags or start/stop codons, red nucleotides correspond to mutated codons. *Tm*, *Thermotoga maritima*; *Pf*, *Pyrococcus furiosus*; aa, amino acid; fwd, forward; rev, reverse; C-His₆, C-terminal hexahistidine tag.

Amplified gene fragment/ mutation	Sequence (5'-3' direction)	Restriction site
<i>TmRad50</i> aa 1-190 fwd	AAAAAAAA <u>CATATG</u> CGCCCTGAACGCCTCACCGTTAGAAA CTTTCTCGG	NdeI
<i>TmRad50</i> aa 1-190 Linker rev	CCGCACCGCCCGCACCGCCT GAGGATATCTCGTTCTCCA GCT	---
<i>TmRad50</i> aa 686-852 Linker fwd	GGCGGTGCGGGCGGTGCGGGCGGT AGTCTGGAGAAGA AACTAAAAGAGA	---
<i>TmRad50</i> aa 686-852 rev	AAAAAAAAAGCGGCCGCTCACTCATTCAACCAACTCCTC	NotI
<i>TmMre11</i> aa 7-385 fwd	AAAAAAAAAGCGGCCGCTAACTTTAAGAAGGAGATATACA ATG AAAATTCTGCACACATCCGACTGGCACCTC	NotI
<i>TmMre11</i> aa 7-385 rev	TTTTTT <u>GCTCAGCTC</u> AGGCCTCACTCTTTTTCACCTCAT	Bpu1102I
<i>TmMre11</i> ^{H94Q} fwd	CAGGAAACCA AG GATTGGAAGGGGTTGAAACTCTT	---

<i>TmMre11</i> ^{H94Q} rev	CTTCCAATCCTGGTTTCTGGAAGTACAACCAC	---
<i>TmMre11</i> aa 343-385 fwd	AAAAAAAAGCGGCCGCTAACTTTAAGAAGGAGATATAGT AATGAAAAGAAGAAGCTGGACAAGCTTGATT	NotI
<i>TmMre11</i> aa 343-385 C-His ₆ rev	TTTTTTGCTCAGCTTAGTGGTGGTGGTGGTGGTGGCCGG CCTCACTCTTTTTCACCTCAT	Bpu1102I
<i>TmMre11</i> ^{F291S} fwd	GAAAAGCATAAGGGATTCTGCAGGAATTTTCCTG	---
<i>TmMre11</i> ^{F291S} rev	CAGGAAAATTCCTGCAGGAATCCCTTATGCTTTTC	---
<i>TmMre11</i> ^{Y277R} fwd	CGTTGAAAACCTCTCTACCGCAAAAAGATAGACACCT	---
<i>TmMre11</i> ^{Y277R} rev	GAGGTGTCTATCTTTTTCGGTAGAGAGTTTCAACG	---
<i>TmRad50</i> ^{W758A} fwd	GGTTTTATCATAAAAAGATGCGGGTATCGAAAGACCAG	---
<i>TmRad50</i> ^{W758A} rev	CTGGTCTTTCGATACCCGCACTCTTTTATGATAAAACC	---
<i>TmRad50</i> ^{I760C} fwd	CATAAAAGATTGGGGTTCGAAAGACCAGCGAGG	---
<i>TmRad50</i> ^{I760C} rev	CCTCGTGGTCTTTCGCAACCCCAATCTTTTATG	---
<i>TmRad50</i> ^{N64C} fwd	GATTACGTGAACAGGTTCGCGCCGTCGATGGAAC	---
<i>TmRad50</i> ^{N64C} rev	GTTCCATCGACGGCGCACCTGTTACGTAATC	---
<i>TmRad50</i> ^{D804C} fwd	GGGTTTTCCAGTCTCTGACACGGAGAACAAAGAG	---
<i>TmRad50</i> ^{D804C} rev	CTCTTTGTTCTCCGTGCAAGAGACTGGAAAACCC	---
<i>TmRad50</i> ^{H830C} fwd	GATCGTTTTATCACGTGCGACAGGGAGTTCTC	---
<i>TmRad50</i> ^{H830C} rev	GAGAACTCCCTGTCGCAAGTGATGAAAACGATC	---
<i>PfRad50</i> aa 1-215 fwd	CTATACTCATATGAAGTTGGAGAGAGTGACTGTGA	NdeI
<i>PfRad50</i> aa 1-215 Linker rev	TGCAGATCCTGAACCAGATGCTATCTCTGGAGAACTTG AATAA	---
<i>PfRad50</i> aa 689-882 Linker fwd	GCATCTGGTTCAGGATCTGCAGAAAAGAGGAGAGACAC AATAAA	---
<i>PfRad50</i> aa 689-882 rev	ACTATTCTGCGGCCGCTCAAGAGACCACCTCCACC	NotI
<i>PfMre11</i> aa 1-426 fwd	CTATACTCATATGAAGTTTGCTCACTTAGCCGATAT	NdeI
<i>PfMre11</i> aa 1-426 rev	ATATATTGCGGCCGCTCATCTAGCACCACCAAGCCAGCTA TCAAG	NotI
<i>PfRad50</i> ^{E823Q} fwd	GCCTCCTGATTTTAGATCAGCCAACGCCTTATTTAG	---
<i>PfRad50</i> ^{E823Q} rev	CTAAATAAGGCGTTGGCTGATCTAAAATCAGGAGGC	---
<i>PfMre11</i> ^{H85Q} fwd	CTATAGAAGGGAATCAGGACAGAACACAGAGAGG	---
<i>PfMre11</i> ^{H85Q} rev	CTCTCTGTGTTCTGTCTGATTCCCTTCTATAG	---

Table 2: DNA oligonucleotides used for *in vitro* activity assays. DNA sequences are adjusted to (Guy and Bolt, 2005). For annealing, the oligonucleotides were mixed with a 1.1fold molar excess of the unlabeled oligonucleotide in annealing buffer (40 mM Tris pH 7.5, 100 mM NaCl, 10 mM MgCl₂), incubated in a thermocycler (Biometra T personal) for 5 min at 95°C, and cooled down to 4°C at a cooling rate of 0.1°C/s. In the case of ds40mer either strand 1 and 2 or strand 1 and 3 were annealed. The particular label, 6-FAM or fluorescein (FLC), are highlighted in green. ds, double stranded; ss, single stranded;

Name	Sequence (5'-3' direction)
ss40mer	strand 1: 6-FAM – TT
ds40mer	strand 1: FLC - ATTCTGGCTTGCTAGGACATGCTGTCTAGAGACTATCGAT
	strand 2: ATCGATAGTCTCTAGACAGCATGTCCTAGCAAGCCAGAAT
	strand 3: FLC - ATCGATAGTCTCTAGACAGCATGTCCTAGCAAGCCAGAAT
ds50mer	strand 1: 6-FAM - ATCGATAGTCTCTAGACAGCATGTCCTAGCAAGCCAGAATTCGGCAGCGT
	strand 2: ACGCTGCCGAATTCTGGCTTGCTAGGACATGCTGTCTAGAGACTATCGAT

3.1.2. Plasmids

Table 3: Plasmids used for recombinant protein expression in *E. coli*. *Tm*, *Thermotoga maritima*; *Pf*, *Pyrococcus furiosus*; aa, amino acid; HLH, helix-loop-helix domain; NBD, nucleotide binding domain; C(N)-His₆, C(N)-terminal hexahistidine tag; L8(7), Linker of 8 and 7 amino acids, respectively;

Name of expression construct	Encoded fragment	Restriction sites	Tag	Vector
p <i>TmMre11</i> ^{HLH} :Rad50 ^{NBD} (from D.J. Bemeleit, AG Hopfner)	<i>TmRad50</i> : aa 1-190/ L8 ^{GGAGGAGG} /686-852 and <i>TmMre11</i> : aa 343-385	NdeI/NotI NotI/Bpu1102I	C ^{Mre11} -His ₆	pET-29b
p <i>TmMre11</i> :Rad50 ^{NBD} (from D.J. Bemeleit, AG Hopfner)	<i>TmRad50</i> : aa 1-190/ L8 ^{GGAGGAGG} /686-852 and <i>TmMre11</i> : aa 7-385	NdeI/NotI NotI/Bpu1102I	---	pET-29b
p <i>TmMre11</i> ^{H94Q} :Rad50 ^{NBD} (from C.B. Schiller, AG Hopfner)	<i>TmRad50</i> : aa 1-190/ L8 ^{GGAGGAGG} /686-852 and <i>TmMre11</i> : aa 7-385 ^{H94Q}	NdeI/NotI NotI/Bpu1102I	N ^{Rad50} -His ₆	pET-28b ^{TEV}
p <i>TmMre11</i> ^{H94Q, F291S} :Rad50 ^{NBD}	<i>TmRad50</i> : aa 1-190/ L8 ^{GGAGGAGG} /686-852 and <i>TmMre11</i> : aa 7-385 ^{H94Q, F291S}	NdeI/NotI NotI/Bpu1102I	N ^{Rad50} -His ₆	pET-28b ^{TEV}
p <i>TmMre11</i> ^{H94Q, Y277R} :Rad50 ^{NBD}	<i>TmRad50</i> : aa 1-190/ L8 ^{GGAGGAGG} /686-852 and <i>TmMre11</i> : aa 7-385 ^{H94Q, Y277R}	NdeI/NotI NotI/Bpu1102I	N ^{Rad50} -His ₆	pET-28b ^{TEV}
p <i>TmMre11</i> ^{H94Q} :Rad50 ^{NBD, W758}	<i>TmRad50</i> : aa 1-190/ L8 ^{GGAGGAGG} /686-852 ^{W758A} and <i>TmMre11</i> : aa 7-385 ^{H94Q}	NdeI/NotI NotI/Bpu1102I	N ^{Rad50} -His ₆	pET-28b ^{TEV}

p <i>TmMre11</i> ^{H94Q} :Rad50 ^{NBD, I760C}	<i>TmRad50</i> : aa 1-190/ L8 ^{GGAGGAGG} /686-852 ^{I760C} and <i>TmMre11</i> : aa 7-385 ^{H94Q}	NdeI/NotI NotI/Bpu1102I	N ^{Rad50} -His ₆	pET-28b ^{TEV}
p <i>TmMre11</i> ^{H94Q} : Rad50 ^{NBD, N64C, I760C}	<i>TmRad50</i> : aa 1-190/ L8 ^{GGAGGAGG} /686-852 ^{I760C, N64C} and <i>TmMre11</i> : aa 7-385 ^{H94Q}	NdeI/NotI NotI/Bpu1102I	N ^{Rad50} -His ₆	pET-28b ^{TEV}
p <i>TmMre11</i> ^{H94Q} : Rad50 ^{NBD, D804C, H830C}	<i>TmRad50</i> : aa 1-190/ L8 ^{GGAGGAGG} /686-852 ^{D804C, H830C} and <i>TmMre11</i> : aa 7-385 ^{H94Q}	NdeI/NotI NotI/Bpu1102I	N ^{Rad50} -His ₆	pET-28b ^{TEV}
p <i>TmMre11</i> ^{H94Q, F291S} : Rad50 ^{NBD, D804C, H830C}	<i>TmRad50</i> : aa 1-190/ L8 ^{GGAGGAGG} /686-852 ^{D804C, H830C} and <i>TmMre11</i> : aa 7-385 ^{H94Q, F291S}	NdeI/NotI NotI/Bpu1102I	N ^{Rad50} -His ₆	pET-28b ^{TEV}
p <i>TmMre11</i> ^{H94Q} : Rad50 ^{NBD, D804C, H830C}	<i>TmRad50</i> : aa 1-190/ L8 ^{GGAGGAGG} /686-852 ^{D804C, H830C} and <i>TmMre11</i> : aa 7-385 ^{H94Q, F291S}	NdeI/NotI NotI/Bpu1102I	---	pET-29b
p <i>PfMre11</i> :Rad50 ^{NBD, E823Q}	<i>PfRad50</i> : aa 1-215/ L7 ^{ASGSGSA} /689-882 ^{E823Q} and <i>PfMre11</i> : aa 1-426	NdeI/NotI NotI/AscI AarI/AscI	---	pKP-29
p <i>PfMre11</i> ^{H85Q} :Rad50 ^{NBD, E823Q}	<i>PfRad50</i> : aa 1-215/ L7 ^{ASGSGSA} /689-882 ^{E823Q} and <i>PfMre11</i> : aa 1-426 ^{H85Q}	NdeI/NotI NotI/AscI AarI/AscI	---	pKP-29
pAK400-FITC-E2wt (Pedrazzi et al., 1997)	scFv fragment FITC-E2	SfiI	C-His ₆	pAK400

Table 4: Plasmids used for *in vitro* activity assays.

Name	description	length	Source
ΦX174 RF II	double stranded, nicked, circular form of ΦX174 DNA (relaxed form)	5386 base pairs	New England Biolabs (Frankfurt)
ΦX174 Virion	single stranded, circular, viral DNA	5386 bases	New England Biolabs (Frankfurt)
pBluescript II KS +	double stranded, supercoiled DNA	2958 base pairs	Fermentas (St. Leon-Rot)

3.1.3. Strains

Table 5: *E. coli* strains used for molecular cloning and recombinant protein expression. The *E. coli* XL1 blue strain was used for molecular cloning, the *E. coli* Rosetta (DE3) and BL21 Star (DE3) strains were used for recombinant protein expression.

Strain	Genotype	Source
XL1- Blue	<i>recA1 endA1 gyrA96 thi-1 hsdR17 supE44 relA1 lac</i> [F' <i>proAB lacI^fZΔM15 Tn10</i> (Tet ^R)]	Stratagene (Heidelberg)
Rosetta (DE3)	F ⁻ <i>ompT hsdS_B</i> (r _B ⁻ m _B ⁻) <i>gal dcm</i> (DE3) pRARE (Cam ^R)	Novagen (Madison, USA)
BL21 Star (DE3)	F ⁻ <i>ompT hsdS_B</i> (r _B ⁻ m _B ⁻) <i>gal dcm rne131</i> (DE3)	Invitrogen (Karlsruhe)

3.1.4. Media and antibiotics

Lysogeny Broth (LB) liquid media as well as LB agar plates (1% (w/w) NaCl, 1% (w/v) Bacto-tryptone, 0.5% (w/v) yeast extract and ± 1.5% agar) were prepared according to standard protocols (Sambrook and Russell, 2001). Respective antibiotics were added to the media using following concentrations: kanamycin (50 µg/ml) and chloramphenicol (34 µg/ml).

3.1.5. Preparation of sodium orthovanadate solution

Since vanadium is a transition metal, it exists in aqueous solutions in different oxidation states (4+, 5+), resulting in vanadyl and vanadate ionic species, respectively. Vanadyl, metavanadate, orthovanadate, and decavanadate are interconverted depending on the concentration, pH, and redox potential of the solution. Therefore the preparation of a 150 mM sodium orthovanadate stock solution was carried out in water adjusted to pH ~10. To ensure the presence of vanadate monomers, the solution was boiled until it became translucent followed by readjustment of the pH to 10. Orange color observed before boiling is due to decavanadate. Recurring cycles of boiling and readjustment lead to a stable pH of 10, therefore resulting in a stable solution containing orthovanadate.

3.2. Molecular biology methods

Common molecular biology procedures were carried out according to standard protocols if not indicated differently (Sambrook and Russell, 2001). Commercially available kits and enzymes were used following the manufacturer's instructions.

3.2.1. Molecular cloning

Constructs of bacterial and archaeal Mre11 and Rad50 (MR) were designed using sequence alignments of MR from several species generated by ClustalW (Larkin et al., 2007), as well as secondary structure predictions with JPRED (Cole et al., 2008) and PSIPRED (Bryson et al., 2005), and coiled-coil predictions considered by the COILS server (Lupas et al., 1991).

DNA Oligonucleotides for molecular cloning were designed using the program GeneRunner (<http://www.generunner.net/>) and contained individually restriction sites and additional sequences encoding linker regions or hexahistidine affinity tags for protein purification (Table 1). The corresponding genes of Mre11 and Rad50 were amplified by polymerase chain reaction (PCR) from *Thermotoga maritima* MSB8 (*Tm*) or *Pyrococcus furiosus* (*Pf*) genomic DNA using the Phusion[®] Flash High-Fidelity PCR Master Mix (Finnzymes, Espoo, Finland). A typical PCR reaction contained 10-50 ng template DNA and 50 pmol of each DNA oligonucleotide in a total volume of 20 μ l. The standard PCR program used is shown in Table 6.

Table 6: Standard PCR program used for molecular cloning. X°C, depending on melting temperature of used oligonucleotide.

Cycle step	temperature	time	Cycles
1. Initial denaturation	98°C	10 sec	1
2. Denaturation	98°C	1 sec	30
3. Annealing	X°C	5 sec	
4. Extension	72°C	15 sec/1 kb	
5. Final extension	72°C	1 min	1
	4°C	hold	

TmRad50^{NBD} was engineered by fusing the N-terminal (aa 1-190) and C-terminal (aa 686-852) segments by an 8 amino acid linker (GGAGGAGG) in a single open reading frame of pET-29b or pET-28b^{TEV} with NdeI/NotI. Either *TmMre11* (aa L7M-385) or *TmMre11*^{HLH} (aa 343-385) were cloned downstream the *Rad50*^{NBD} gene with NotI/Bpu1102I, respectively.

PfRad50^{NBD} was engineered by fusing the N-terminal (aa 1-215) and C-terminal (aa 689-882) segments by an 7 amino acid linker (ASGSGSA) in a single open reading frame of pKP-29 with NdeI/NotI. Likewise *PfRad50*^{NBD}, *PfMre11* (aa 1- 426) was cloned into pKP-29. To facilitate coexpression of Mre11 and *Rad50*^{NBD}, *PfRad50*^{NBD} was transformed/subcloned with NotI/AscI and AarI/AscI from pKP-29_*PfRad50*^{NBD} into pKP-29_*PfMre11* downstream the Mre11 gene.

All constructs were analysed via DNA sequencing by Eurofins MWG Operon (Ebersberg) or GATC Biotech (Kempten) and are listed in Table 3.

3.2.2. Site directed mutagenesis

DNA Oligonucleotides with single and multiple nucleotide substitutions were designed with the help of the program PrimerX (<http://www.bioinformatics.org/primerx/>) (Table 1). Mre11:Rad50 mutants described in this thesis were generated by Site Directed Mutagenesis using Overlap Extension PCR and the Phusion[®] Flash High-Fidelity PCR Master Mix (Finnzymes, Espoo, Finland). Usually an Overlap Extension PCR exists of two separated PCR steps. In the first PCR reaction, two fragments containing either the 5' or 3' region of the mutation site together with an overlapping region are generated. In a second step, to allow subsequent hybridization of the overlapping regions and therefore extension of the full length PCR product, relevant DNA oligonucleotides are added with a hold of 5 PCR cycles to the second PCR reaction. Both PCR and further cloning steps were carried out analogous to 3.2.1. Constructs were analysed via DNA sequencing by Eurofins MWG Operon (Ebersberg) or GATC Biotech (Kempten) and are listed in Table 3.

3.2.3. Transformation of *E. coli*

E. coli strains used for transformation are listed in Table 5. Chemically competent cells were prepared based on the methodology from Hanahan (Hanahan, 1983). For transformation, 10 ng of plasmid DNA or 100 ng of ligated DNA were added to 75 μ l of chemically competent *E. coli* cells. Subsequent incubation on ice for 15 min, cells were heat-shocked at 42°C for 1 min and cooled down on ice for 2 min. After adding 900 μ l of LB medium, the cells were incubated under aerobic conditions at 37°C for 45 min. Either 50 μ l or in the case of a ligation reaction the whole cell suspension were plated on LB-agar plates containing the respective antibiotics and incubated at 37°C overnight.

3.3. Protein biochemistry methods

3.3.1. Protein expression in *E. coli*

For recombinant protein expression either *E. coli* Rosetta (DE3) or *E. coli* BL21 Star (DE3) (Table 5) cells containing the plasmid of interest (Table 3) were grown in LB media under aerobic conditions at 37°C to an OD₆₀₀ of 0.6-0.8. Protein expression was induced by addition of 0.5 mM IPTG and carried out at 18°C overnight. Cells were harvested by centrifugation the next morning, frozen in liquid nitrogen and stored at -80°C until further use.

3.3.2. Purification of recombinant proteins

Purification of recombinant MR protein was dependent on the character and on the tag-labeling of the particular protein. Respective buffers and their compositions are listed in Table 7.

Cells containing recombinant *TmMre11:Rad50*^{NBD} protein without tag were resuspended in buffer A and disrupted by sonication. The cell lysate was cleared by centrifugation and the supernatant was heated up to 60°C for 10 min to remove heat labile *E. coli* proteins. Further purification was performed by ammonium sulfate precipitation (40%, 60%) and hydrophobic interaction chromatography Phenyl HP column with buffer B

and C. Subsequently HiTrap Q HP anion exchange chromatography with buffer D and E, and Superdex 200 size-exclusion chromatography with buffer F was performed.

His₆-labeled *TmMre11:Rad50*^{NBD} protein was purified following initial resuspension of harvested cells in buffer G and disruption by sonication. The cell lysate was cleared by centrifugation and the supernatant was incubated at 60°C for 10 min. After Ni-NTA affinity chromatography (Qiagen) in buffer H-J, the proteins were purified by Superdex 200 size-exclusion chromatography in buffer F.

Cells containing recombinant His₆-labeled *TmMre11*^{HLH}:*Rad50*^{NBD} protein were resuspended in buffer K and disrupted by sonication. The cell lysate was cleared by centrifugation and the supernatant was heated up to 60°C for 10 min. Further purification was performed by affinity chromatography Ni-NTA column (Qiagen) in buffer K-M and by Superdex 200 size-exclusion chromatography with buffer N.

For purification of *PfMre11:Rad50*^{NBD} cells, containing recombinant protein, were resuspended in buffer A and disrupted by sonication. The cell lysate was cleared by centrifugation and the supernatant was incubated at 60°C for 10 min. After ammonium sulfate precipitation, Sephacryl 300 size-exclusion chromatography in high salt buffer O was performed. Following this, the protein was purified by HiTrap SP FF ion-exchange chromatography in buffer P and Q and by Superdex 200 size-exclusion chromatography in buffer R.

Purification of the fluorescein binding scFv fragment FITC:E2 was carried out on the basis of C-terminal His₆ tag. First, harvested cells were resuspended in buffer H and disrupted by sonication. After the cell lysate was cleared by centrifugation the protein was purified by affinity chromatography Ni-NTA column (Qiagen) with buffers H, I and S and by HiTrap Q HP anion exchange with buffer T and U. As final step, a Superdex 200 size-exclusion chromatography in buffer F was performed.

Table 7: Buffers used for purification of recombinant protein. When stated, 5 mM β -Mercaptoethanol was added to the buffers when cysteine mutants were purified.

Name	Composition
Buffer A	20 mM Tris pH 7.6, 500 mM NaCl, 5 mM EDTA, (\pm 5 mM β -Mercaptoethanol)
Buffer B	20 mM Tris pH 7.5, 3 M KCl, 1 mM EDTA, (\pm 5 mM β -Mercaptoethanol)
Buffer C	20 mM Tris pH 7.5, 1 mM EDTA, (\pm 5 mM β -Mercaptoethanol)
Buffer D	20 mM Tris pH 8.3, 50 mM NaCl, 1 mM EDTA, (\pm 5 mM β -Mercaptoethanol)
Buffer E	20 mM Tris pH 8.3, 1 M NaCl, 1 mM EDTA, (\pm 5 mM β -Mercaptoethanol)
Buffer F	200 mM NaCl, 20 mM Tris pH 7.8, (\pm 5 mM β -Mercaptoethanol)
Buffer G	20 mM Tris pH 7.6, 500 mM NaCl, (\pm 5 mM β -Mercaptoethanol)
Buffer H	50 mM NaH_2PO_4 pH 7.8, 200 mM NaCl, 10 mM imidazole (\pm 5 mM β -Mercaptoethanol)
Buffer I	50 mM NaH_2PO_4 pH 7.8, 1 M NaCl, 30 mM imidazole (\pm 5 mM β -Mercaptoethanol)
Buffer J	50 mM NaH_2PO_4 pH 7.8, 200 mM NaCl, 250 mM imidazole (\pm 5 mM β -Mercaptoethanol)
Buffer K	50 mM NaH_2PO_4 pH 7.0, 300 mM NaCl, 10% (v/v) glycerol, 10 mM imidazole, 2 mM β -Mercaptoethanol
Buffer L	50 mM NaH_2PO_4 pH 7.0, 1.5 M NaCl, 10% glycerol, 30 mM imidazole, 2 mM β -Mercaptoethanol
Buffer M	50 mM NaH_2PO_4 pH 7.0, 100 mM NaCl, 250 mM imidazole, 2 mM β -Mercaptoethanol
Buffer N	200 mM NaCl, 5 mM Tris pH 7.8
Buffer O	20 mM Tris pH 7.6 and 2 M LiCl
Buffer P	20 mM MES pH 7.0, 100 mM Potassium acetate, 5 mM EDTA
Buffer Q	20 mM MES pH 7.0 1 M Potassium acetate, 5 mM EDTA
Buffer R	20 mM Tris pH 7.6, 200 mM NaCl, 5 mM MgCl_2
Buffer S	50 mM NaH_2PO_4 pH 7.8, 200 mM NaCl, 150 mM imidazole
Buffer T	20 mM Tris pH 8.0, 50 mM NaCl, 0.1 mM EDTA
Buffer U	20 mM Tris pH 7.8, 1 M NaCl

3.3.3. Denaturing polyacrylamide gel electrophoresis (SDS-PAGE)

Protein samples were analyzed by discontinuous Polyacrylamide Gel Electrophoresis analogous to the protocol of Laemmli (Laemmli, 1970) using the vertical Mini-PROTEAN 3 System (BioRad). Depending on the molecular weight of the particular protein, gels containing 10%, 12% and 15% acrylamide in the separating gel were used. Prior to loading, samples were mixed with 1 fold Loading Dye (4fold: 110 mM Tris pH 6.8, 16% (v/v) glycerol, 4% (w/v) SDS, 5% (v/v) β -mercaptoethanol, 0.6% (w/v) bromphenol blue). Subsequent to electrophoresis at 200V-230V in running buffer (25 mM Tris, 192 mM glycine, 0.1% (w/v) SDS), gels were stained in Coomassie staining solution (7% (v/v) acetic acid, 50% (v/v) ethanol, 0.2% (w/v) Coomassie Brilliant Blue R-250) and destained with deionised water. As molecular weight standard the *PAGE RULERTM PRESTAINED PROTEIN LADDER* #SM0671 (Fermentas) was used.

3.3.4. Dimerization of *TmMre11^{HLH}:Rad50^{NBD}*

Dimerization of *TmMre11^{HLH}:Rad50^{NBD}* was carried out by mixing 54 mg/ml (580 μ M) protein with 14 mM of the ATP analog AMPPNP. The dimerization process reached its maximum after 3 days of incubation at 4°C. To quantify the amount of dimerized protein, an aliquot of the mixture was loaded onto a S200 5/150 GL column and analyzed by analytical Gel filtration (see section 3.3.5).

3.3.5. Analytical size exclusion chromatography

In order to determine the oligomeric state and homogeneity of purified proteins or to analyze Protein-Protein and DNA-Protein interactions of the bacterial MR complex, samples were loaded onto a Superdex 200 5/150 GL or Superose 6 PC 3.2/30 gel filtration column respectively and analyzed by analytical gel filtration. Examined interaction partners and their corresponding chromatography running buffers are listed in Table 8.

Table 8: Analyzed Protein-Protein and DNA-Protein interactions and their corresponding buffer conditions. *Tm*, *Thermotoga maritima*; HLH, helix-loop-helix domain (aa 343-385); NBD, nucleotide binding domain (aa 1-190/L8/686-852); (1), interaction partner 1; (2), interaction partner 2; (3), interaction partner 3.

Interaction partner	Chromatography running buffer
(1) <i>TmMre11</i> ^{HLH} : <i>Rad50</i> ^{NBD (Mono)} (2) <i>TmMre11</i> ^{HLH} : <i>Rad50</i> ^{NBD (Mono)}	50 mM Tris pH 7.8, 100 mM NaCl, 5 mM MgCl ₂ , 100 μM MnCl ₂
(1) <i>TmMre11</i> ^{F291S} : <i>Rad50</i> ^{NBD, D804C, H830C} (2) ds plasmid DNA (ΦX174 RF II)	50 mM Tris pH 7.8, 200 mM NaCl, 10 mM MgCl ₂ , 1 mM MnCl ₂
(1) <i>TmMre11</i> ^{F291S} : <i>Rad50</i> ^{NBD, D804C, H830C} (2) ss plasmid DNA (ΦX174 Virion)	50 mM Tris pH 7.8, 200 mM NaCl, 10 mM MgCl ₂ , 1 mM MnCl ₂
(1) <i>TmMre11</i> : <i>Rad50</i> ^{NBD (S-S)} (2) FITC-E2 (3) ds40mer (strand 1 and 3)	50 mM Tris pH 7.8, 300 mM NaCl, 10 mM MgCl ₂ , 1 mM MnCl ₂

3.3.6. Crosslinking via Bis-Maleimidoethane (BMOE)

The double-mutant *TmMre11*:*Rad50*^{NBD, I760C, N64C} complex was purified under reducing conditions (5 mM β-Mercaptoethanol; 3.3.2) and rebuffered into crosslinking buffer containing 50 mM Tris pH 7.8, 200 mM NaCl, 10 mM MgCl₂, 1 mM MnCl₂ using a HiTrap Desalting column. The protein was concentrated to 1 mg/ml (5.5 μM) and mixed with either 5 mM AMPPNP or 5 mM ATP and 16.5 μM BMOE (Bis-Maleimidoethane) (Pierce). The crosslinking agent was dissolved to a concentration of 10 mM in DMSO just before use and diluted to 50 μM BMOE stock solution in crosslinking buffer. After 1 min incubation at 60°C, 50 mM cysteine was added to stop the reaction. Subsequently the samples were run on SDS-PAGE followed by Coomassie blue staining (3.3.3).

3.3.7. Disulfide bridging via copper sulfate (CuSO₄)

For disulfide bond formation the *TmMre11*^{H94Q}:*Rad50*^{NBD, D804C, H830C} and *TmMre11*^{H94Q, F291S}:*Rad50*^{NBD, D804C, H830C} mutant complexes were purified under reducing conditions (5 mM β-Mercaptoethanol; 3.3.2) and rebuffered into crosslinking buffer as described for the BMOE crosslink (3.3.6). The proteins were concentrated to 4 mg/ml

(21.5 μM), mixed with 5 mM ATP and 50 μM CuSO_4 and incubated at 25°C for 3h. Formation of the disulfide bond (denoted S-S) was analyzed by SDS-PAGE using a nonreducing Loading Dye (4fold: 110 mM Tris pH 6.8, 16% (v/v) glycerol, 4% (w/v) SDS, 0.6% (w/v) bromphenol blue) (3.3.3).

3.4. Structural biology methods

3.4.1. Crystallization

Crystals of $TmMre11^{\text{HLH}}:\text{Rad50}^{\text{NBD}}:\text{AMPPNP}$ were grown by the sitting drop vapor diffusion method at 19°C. Crystals were set up in commercial 96-well format screens by the Max-Planck-Crystallization Facility (Martinsried). Prior to crystallization set up, 5 mM AMPPNP was added to the protein solution. By mixing 200 nl of protein solution at 10.5 mg/ml protein concentration with 200 nl of the reservoir solution containing 20% (w/v) PEG-2000 MME, 0.2 M Trimethylamine N-oxide and 0.1 M Tris pH 8.5, protein crystals appeared after 9 days of incubation. After 5 additional days the crystals reached a maximum size of 300 x 100 x 25 μM . Prior to flash freezing in liquid nitrogen, crystals were transferred to reservoir solution supplemented with 10% (v/v) 2,3-butandiol.

To get insights about the transition state expected for phosphoryl transfer in Rad50, $TmMre11^{\text{HLH}}:\text{Rad50}^{\text{NBD}}$ was co-crystallized with ADP and the orthovanadate anion $[\text{VO}_4]^{3-}$ which mimics the conformation of the leaving phosphate group. Crystals were set up in commercial 96-well format sitting drop screens by the Max-Planck-Crystallization Facility (Martinsried). Prior to crystallization set up, 5 mM ADP, 8.5 mM sodium orthovanadate solution (3.1.5) and 2.5 mM MgCl_2 was added to the protein solution. By mixing 200 nl of protein solution at 10.5 mg/ml protein concentration with 200 nl of the reservoir solution containing 25% (v/v) PEG 1500 and 0.1 M MMT buffer pH 9.0, protein crystals appeared after 2 days of incubation at 19°C. Prior to flash freezing in liquid nitrogen, crystals were transferred to reservoir solution supplemented with 10% (v/v) 2,3-butandiol.

Prior to crystallization set up, the $Mre11^{\text{H94Q, F291S}}:\text{Rad50}^{\text{NBD, D804C, H830C}}$ complex of *T. maritima* was disulfide bridged as described in 3.3.7. Subsequently crystals of $Mre11^{\text{H94Q, F291S}}:\text{Rad50}^{\text{NBD, D804C, H830C}}$ (S-S) were grown by the sitting drop vapor diffusion

method at 20°C. Crystals were set up manually in commercial 96-well format sitting drop screens. By mixing 1 µl of protein solution at 4 mg/ml protein concentration with 1 µl of the reservoir solution containing 2.2 M ammonium sulfate and 0.2 M di-ammonium tartrate, protein crystals appeared after 9 days of incubation. After 2 additional days the crystals reached a maximum size of 70 x 70 x 50 µM. Prior to flash freezing in liquid nitrogen, crystals were transferred to reservoir solution supplemented with 10% (v/v) sucrose and 10% (v/v) xylitol.

TmMre11^{core} (aa 7-325) crystals were grown by the sitting drop vapor diffusion method at 19°C. Trials were set up in commercial 96-well format sitting drop screens by the Max-Planck-Crystallization Facility (Martinsried). By mixing 200 nl of protein solution at 3 mg/ml protein concentration with 200 nl of the reservoir solution containing 20% (w/v) PEG 3350, 0.2 M sodium sulfate, 0.1 M Bis-tris propane pH 6.5, protein crystals appeared after 12 days of incubation. Prior to flash freezing in liquid nitrogen, crystals were transferred to reservoir solution supplemented with 15% (v/v) 2,3-butandiol.

An overview of protein preparation buffers, protein concentrations, crystallization solutions and cryo protectants for all crystallized proteins are summarized in Table 9.

Table 9: Overview of crystallization conditions for various *T. maritima* Mre11(:Rad50^{NBD}) constructs.

Crystallised protein	Preparation buffer	c (Protein)	Crystallization solution	Cryo reagent
<i>TmMre11</i> ^{HLH} :Rad50 ^{NBD} , AMPPNP	5 mM Tris pH 7.8, 200 mM NaCl,	10.5 mg/ml	20% (w/v) PEG-2000 MME, 0.2 M Trimethylamine N-oxide, 0.1 M Tris pH 8.5	10% (v/v) 2,3- butandiol
<i>TmMre11</i> ^{HLH} :Rad50 ^{NBD} , ADP[VO ₄] ³⁻	5 mM Tris pH 7.8, 200 mM NaCl,	10.5 mg/ml	25% (v/v) PEG 1500, 0.1 M MMT buffer pH 9.0	10% (v/v) 2,3- butandiol
<i>TmMre11</i> ^{H94Q,F291S} : Rad50 ^{NBD, D804C, H830C (S-S)} , ATP	50 mM Tris pH 7.8, 200 mM NaCl, 10 mM MgCl ₂ , 1 mM MnCl ₂ , 50 µM CuSO ₄ , 5 mM ATP	4 mg/ml	2.2 M ammonium sulfate, 0.2 M di-ammonium tartrate	10% (v/v) sucrose and 10% (v/v) xylitol
<i>TmMre11</i> ^{core}	5 mM Tris pH 7.8, 200 mM NaCl	3 mg/ml	20% (w/v) PEG 3350, 0.2 M sodium sulfate, 0.1 M Bis-tris propane pH 6.5	15% (v/v) 2,3- butandiol

3.4.2. Data collection

Data from native $TmMre11^{HLH}:Rad50^{NBD}:AMPPNP$ and $TmMre11^{HLH}:Rad50^{NBD}:ADP[VO_4]^{3-}$ crystals were collected to a resolution of 1.9 Å and 2.9 Å respectively at the beamline ID14-1 and ID14-4 at the European Synchrotron Radiation Facility (ESRF, Grenoble, France). The crystals containing AMPPNP belonged to space group P1 with $a=49.3$ Å, $b=68.8$ Å and $c=71.4$ Å, whereas crystals containing $ADP[VO_4]^{3-}$ belonged to space group $P2_1$ with $a=69.4$ Å, $b=51.8$ Å and $c=134.3$ Å. Both crystal forms contained one $TmMre11^{HLH}_2:Rad50^{NBD}_2$ complex molecule in the asymmetric unit.

Data from native $TmMre11^{core}$ crystals were collected to a resolution of 2.8 Å at the X06SA beamline Swiss Light Source (SLS, Villigen, Switzerland). The crystals of $TmMre11^{core}$ belonged to space group $P6_122$ with a , $b=138.9$ Å and $c=123.1$ Å and contained one Mre11 “core” monomer (aa 7-325) in an asymmetric unit.

Data from native $TmMre11^{H94Q, F291S}:Rad50^{NBD, D804C, H830C (S-S)}$ crystals were collected to a resolution of 2.6 Å at the X06SA beamline Swiss Light Source (SLS, Villigen, Switzerland). Crystals of the disulfide bridged complex belonged to space group $P3_221$ with a , $b=121.5$ Å and $c=134.9$ Å and contained half of the $Mre11_2:Rad50^{NBD}_2$ complex in an asymmetric unit.

All collected data were integrated and scaled with XDS (Kabsch, 1993).

3.4.3. Structure determination, model building and refinement

The structure of the $Mre11^{HLH}:Rad50^{NBD}:AMPPNP$ complex was determined by molecular replacement with Phaser (McCoy, 2007) using several fragments (Rad50 residues: 1-142, 143-190/686-792, 793-850; Mre11 residues: 343-385) of the nucleotide unbound $TmMre11:Rad50^{NBD}$ complex (PDB entry: 3QG5) as search model. Prior to model building and refinement, 5% of the reflections for monitoring the free R -value were randomly omitted. The initial model was automatically rebuilt using ARP/wARP (Langer et al., 2008) and Buccaneer (Cowtan, 2006) and manually completed with COOT (Emsley and Cowtan, 2004). After corrections for bulk solvent and overall B -values, the model was refined by iterative cycles of positional and B-factor and TLS refinement with PHENIX (Adams et al., 2002) and manual model building with COOT. The coordinates of the

TmMre11^{HLH}:Rad50^{NBD}:AMPPNP complex structure were submitted to the PDB and assigned PDB ID code 3QF7.

The structure of the *Mre11*^{HLH}:Rad50^{NBD}: ADP[VO₄]³⁻ complex was determined by molecular replacement with Phaser using the previously solved Rad50^{NBD} dimer of *TmMre11*^{HLH}:Rad50^{NBD} (see above) in its AMPPNP bound state without ligand as search model. Prior to model building and refinement, 5% of the reflections for monitoring the free *R*-value were randomly omitted. Refinement was carried out against the previously built *TmMre11*^{HLH}:Rad50^{NBD}:AMPPNP model omitting AMPPNP, coiled-coil and HLH region using the refinement program autoBUSTER and by manual model building with COOT.

The structure of *TmMre11*^{core} was determined by molecular replacement with Phaser using *TmMre11* (residues M7-325) of the nucleotide unbound *Mre11*:Rad50^{NBD} complex (PDB entry: 3QG5) as search model. Prior to model building and refinement, 5% of the reflections for monitoring the free *R*-value were randomly omitted. The initial model was automatically rebuilt using PHENIX and after corrections for bulk solvent and overall *B*-values, the model was refined with PHENIX and manually completed with COOT. The coordinates of the *TmMre11*^{core} structure were submitted to the PDB and assigned PDB ID code 3THN.

The structure of the *TmMre11*^{H94Q, F291S}:Rad50^{NBD, D804C, H830C (S-S)} complex was determined by molecular replacement with Phaser using two fragments (Rad50: residues 1-163 and 720-852) of the previously solved structures *TmMre11*^{HLH}:Rad50^{NBD} and *TmMre11*^{core}(residues M7-325) (see above) as search models. Prior to model building and refinement, 5% of the reflections for monitoring the free *R*-value were randomly omitted. The model was manually built using COOT. After corrections for bulk solvent and overall *B*-values, the model was refined by iterative cycles of positional and B-factor and TLS refinement with PHENIX and manual model building with COOT. The coordinates for the *TmMre11*^{H94Q, F291S}:Rad50^{NBD, D804C, H830C (S-S)} complex structure in its ATP/ADP bound state were submitted to the PDB and assigned PDB ID code 3THO.

All figures were prepared with PyMOL (DeLano Scientific).

3.4.4. Small angle x-ray scattering

Small angle x-ray scattering (SAXS) data were collected at the EMBL X33 beamline at the DORIS storage ring (Deutsches Elektronen Synchrotron (DESY), Hamburg, Germany) using a MAR345 two-dimensional image plate detector and at the ID14-3 BioSAXS beamline at the European Synchrotron Radiation Facility (ESRF, Grenoble, France) using a Pilatus 1M detector. Scattering patterns from solutions of *TmMre11:Rad50*^{NBD, I760C, N64C} (+BMOE) (3.3.6), *TmMre11*^{H94Q, F291S}:*Rad50*^{NBD, D804C, H830C (S-S)} and *PfMre11:Rad50*^{NBD} (w/ or w/o ATP γ S) at concentrations between 1 and 10 mg/ml were measured in SAXS buffer containing 50 mM Tris pH 7.7, 200 mM NaCl, 5 mM MgCl₂. Various programs of the ATSAS software package (Konarev et al., 2006) were used to process and evaluate SAXS data. Initial data processing was carried out with PRIMUS (Konarev et al., 2003) and the radius of gyration (R_G) was calculated using the Guinier approximation and the low resolution ($qxR_G < 1.3$) data. The program GNOM (Svergun, 1992) was used to determine P(r)-functions and subsequent maximum interelectron distances D_{max} . CRY SOL (Svergun et al., 1995) was utilized to compute theoretical SAXS-curves from crystallographic coordinate files and for comparison with the experimental data. *Ab initio* structure modeling was based on the DAMMIN (Svergun, 1999) reciprocal space fitting algorithm, assuming twofold particle symmetry. All figures were prepared using the program UCSF CHIMERA (Pettersen et al., 2004).

3.5. *In vitro* activity assays of Mre11:Rad50

3.5.1. ATP hydrolysis assay

The ATP hydrolysis activity was analyzed by the BIOMOL GREENTM assay (BIOMOL Research Labs, Inc.) using 500 μ M ATP and 5 μ M of the purified protein of interest. The mixtures were incubated either at 60°C or at 25°C for 10 min in buffer containing 50 mM Tris pH 7.7, 100 mM NaCl, 10 mM MgCl₂, 5 mM MnCl₂ and subsequently incubated on ice and centrifuged at 15,000 rpm for 1 min. Afterwards the suitable amount of BIOMOL GREENTM reagent was added to the supernatants, incubated 25 min at 25°C and OD₆₂₀ was measured. Amounts of released free phosphate in the

supernatants were obtained by subtracting the background phosphate following the manufacturer's instruction.

3.5.2. Electrophoretic mobility shift assay (EMSA)

DNA binding reactions for EMSAs were carried out with the nuclease deficient Mre11^{H94Q} mutant of the respective complexes.

For the binding analysis of the *Tm*Mre11:Rad50^{NBD} (denoted *Tm*MR^{NBD}) complex various concentrations of the protein (0, 0.5, 2.0, 4.0 and 6.0 μ M respectively) and 6-FAM labeled blunt end ds50mer DNA (10 nM) (Table 2) were used in 20 mM Tris pH 7.5, 100 mM KCl, 5 mM MgCl₂, 5 mM MnCl₂ and 5% glycerol. The mixture was incubated at room temperature for 5 min in a total volume of 10 μ l. The DNA was resolved by electrophoresis on a step gradient native acrylamide gel (4% and 6.5%) in TB buffer and visualized by scanning with a Typhoon System (Amersham Biosciences) using the green-excited (532 nm) fluorescence mode.

The binding reaction of the disulfide bridged *Tm*Mre11^{F291S}:Rad50^{NBD, H830C, D804C (S-S)} (denoted *Tm*MR^{NBD (S-S)}) complex was carried out with various amounts of the protein (0, 2.5, 5.0, 30, 40 and 50 μ g respectively) and 0.5 μ g of the ds plasmid DNA Φ X174 RF II (Table 4). For comparison of the binding activities of *Tm*MR^{NBD (S-S)} and *Tm*MR^{NBD} either with or w/o 5 mM AMPPNP, various amounts of the protein (0, 5, 10, 20, 40 and 60 μ g respectively) and 0.5 μ g of the ds plasmid DNA Φ X174 RF II (Table 4) were used. The binding reactions of *Tm*MR^{NBD (S-S)} and *Tm*MR^{NBD} w/o ATP analog were performed with fluorescein labeled blunt end ss40mer or ds40mer DNA (strand 1 and 2; 100 nM; Table 2) and various concentrations of the protein (0, 1.0, 2.5, 5.0, 7.5, 10 and 15 μ M respectively). All of the latter mixtures were incubated in 50 mM Tris pH 7.8, 100 mM NaCl, 5 mM MgCl₂ and 100 μ M MnCl₂ at room temperature for 15min in a total volume of 20 μ l. The DNA was resolved by electrophoresis on an agarose gel (0.5%) in TAE buffer and either stained with ethidium bromide (non fluorescent labeled DNA) and visualized with an UV-Imaging System (Intas) or visualized by scanning with a Typhoon System (Amersham Biosciences) using the green-excited (532 nm) fluorescence mode.

Comparison of the DNA affinity of *Tm*Mre11^{HLH}:Rad50^{NBD (Mono)}, *Tm*Mre11^{HLH}:Rad50^{NBD (Dimer)} and *Tm*MR^{NBD (S-S)} was carried out with various

concentrations of the protein (0, 0.25, 0.50, 1.0, 2.0 and 3.0 mg/ml respectively) and 0.025 $\mu\text{g}/\mu\text{l}$ of the ds plasmid DNA ΦX174 RFII (Table 4). Comparison of the plasmid ssDNA ΦX174 Virion (Table 4) binding activity of $Tm\text{Mre11}^{\text{HLH}}:\text{Rad50}^{\text{NBD (Dimer)}}$ and $Tm\text{MR}^{\text{NBD (S-S)}}$ was carried out with 2 fold protein and DNA concentrations. The samples were incubated in 50mM Tris pH 7.8, 100mM NaCl, 5mM MgCl_2 at room temperature for 15 min in a total volume of 20 μl . $Tm\text{MR}^{\text{NBD (S-S)}}$ samples contained additionally 100 μM MnCl_2 , whereas $Tm\text{Mre11}^{\text{HLH}}:\text{Rad50}^{\text{NBD (Dimer)}}$ additionally contained 1 mM of the ATP analog AMPPNP. The DNA was resolved by electrophoresis on an agarose gel (0.5%) in TAE buffer, stained with ethidium bromide and visualized with a UV-Imaging System (Intas).

3.5.3. Nuclease activity assay

Mre11 nuclease activity was tested using a fluorescein 5' labeled ds40mer (strand 1 and 3) (Table 2). For each reaction, 80 nM DNA was incubated with 24 μM of $Tm\text{Mre11}:\text{Rad50}^{\text{NBD}}$ in 20 μl reaction buffer containing 100 mM NaCl, 50 mM Tris pH 7.8, 10 mM MgCl_2 , 100 μM MnCl_2 at 60°C for 90 min. The reaction was stopped by addition of 0.5% SDS and 1 mg/ml proteinase K following incubation at 50°C for 20 min. Subsequently the sample was mixed with 1fold loading dye (6fold: 16% (v/v) formamide, 16% (v/v) glycerol, 10 mM EDTA, 10 mM Tris pH 7.8, 0.03% (w/v) bromphenol blue, 0.03% (w/v) xylene cyanol) and incubated at 95°C for 5 min. Reaction products were resolved by electrophoresis on a denaturing 20% acrylamide gel in TB buffer containing 7 M Urea and visualized with a Typhoon System (Amersham Biosciences) using the green-excited (532 nm) fluorescence mode.

3.5.4. Endonuclease activity assay

Endonucleolytic cleavage of DNA was performed using 0.07 mg/ml of purified $Tm\text{Mre11}:\text{Rad50}^{\text{NBD}}$ and 70 ng/ μl of circular double stranded plasmid DNA (pBluescript II KS+) (Table 4) in 80 mM NaCl, 25 mM HEPES pH 7.0, 5 mM MgCl_2 , 5 mM MnCl_2 , 1 mM DTT. After incubation at 65°C for 45 min, reactions were stopped by the addition of 1% SDS and 1 mg/ml proteinase K and incubation for 20 min at 50°C. Specific nicking of pBluescript II KS+ on the basis of the nicking enzyme Nt. Bsp QI (New England Biolabs)

was performed as control following the manufacturer's instructions. Reaction products were mixed with 1fold loading dye (6fold: 10 mM Tris pH 7.6, 60 mM EDTA, 60% (v/v) glycerol, 0.03% (w/v) bromphenol blue, 0.03% (w/v) xylene cyanol) and subsequently resolved by electrophoresis on a 1% agarose gel in TAE buffer, stained with ethidium bromide and visualized with a UV-Imaging System (Intas).

3.5.5. Protein-DNA encircling assay

To test if Mre11:Rad50^{NBD} of *T. maritima* can be crosslinked by disulfide bond formation around double stranded or single stranded plasmid DNA (Φ X174 RF II; Φ X174 Virion) (Table 4), 0.04 mg/ml DNA was added to the *Tm*Mre11^{F291S}:Rad50^{NBD, D804C, H830C} protein solution right before CuSO₄ treatment and disulfide bridging respectively (3.3.7). Subsequently the samples were loaded onto a Superose 6 PC 3.2/30 gel filtration column and the elution fractions were concentrated by precipitation with 10% TCA and analyzed by SDS-PAGE followed by Coomassie blue staining (3.3.3).

3.5.6. Antibody DNA binding assay

Blocking of DNA ends for electrophoretic mobility shift assays (EMSAs) was carried out with 100 nM of 5' fluorescein labeled ds40mer (strand 1 and 3) (Table 2) and 14 μ M of the single-chain (sc) anti-fluorescein antibody Fv fragment FITC-E2 in buffer 50 mM Tris pH 7.8, 100 mM NaCl, 5 mM MgCl₂, 100 μ M MnCl₂, 3% glycerol and a total volume of 10 μ l. After 10 min incubation various concentrations of the nuclease deficient *Tm*Mre11^{H94Q, F291S}:Rad50^{NBD, D804C, H830C (S-S)} protein (0, 1.75, 3.50, 7.0 and 14.0 μ M respectively) were added to the samples and incubated for another 10 min. The DNA was resolved by electrophoresis on an agarose gel (0.5%) in TB buffer and visualized with a Typhoon scanner (Amersham Biosciences) using the green-excited (532 nm) fluorescence mode. To verify complete DNA blocking by the scFv, an aliquot of the DNA-scFv mixture was loaded onto a S200 5/150 GL Gel filtration column. To verify if *Tm*Mre11^{H94Q, F291S}:Rad50^{NBD, D804C, H830C (S-S)} can be trapped onto ds DNA, 50 μ M of the protein was incubated for 10 min with 500 nM 5' fluorescein labeled ds40mer in buffer containing 50 mM Tris pH 7.8, 300 mM NaCl, 10 mM MgCl₂, 1 mM MnCl₂. Subsequently 5 μ M of the fluorescein binding scFv fragment FITC-E2 was added to the DNA-protein mixture and

incubated for another 10 min. The samples were loaded onto a S200 5/150 GL Gel filtration column and corresponding elution fractions examined by agarose gel electrophoresis (1%).

3.6. Bioinformatic methods

3.6.1. Structure based sequence alignment

The archaeal Rad50 NBD domain of *Pyrococcus furiosus* (*Pf*) was aligned against the previously solved bacterial Rad50 NBD domain of *Thermotoga maritima* (*Tm*) with the program FATCAT (Ye and Godzik, 2004) using the pdb-coordinates of *Pf*Rad50^{NBD} (PDB entry: 1F2U) and *Tm*Mre11^{HLH}:Rad50^{NBD} (chain A and B) as input file.

4. Results

4.1. Mre11^{HLH}:Rad50^{NBD} of *T. maritima*

4.1.1. Cloning and purification of Mre11^{HLH}:Rad50^{NBD}

To get insights into how ATP might impact on the orientation of the coiled-coil domain and Mre11 interaction, an expression construct of *T. maritima* Mre11:Rad50 was designed (see section 3.2.1). The construct spans the nucleotide binding domain of Rad50 including approx. 50 amino acids of the Mre11 binding coiled-coil region (aa 1-190 and aa 686-852; denoted as Rad50^{NBD}) and Mre11's helix-loop-helix domain (aa 343-385; denoted as Mre11^{HLH}) (Figure 7A). The two ends of the shortened coiled-coils were covalently fused by a short, 8 amino acid linker containing glycine and alanine residues in alternating sequence namely GGAGGAGG. To prevent apase hydrolysis of ATP, a substitution of the glutamic acid residue 798^{Rad50} to glutamine (E798Q) was introduced. Residue 798 is located in the Walker B motif of Rad50's ATPase domain and this substitution was shown to block ATP hydrolysis whereas ATP binding stays unaffected (Hung et al., 1998).

In view of the fact that *T. maritima* belongs to the thermophilic bacteria, Mre11^{HLH}:Rad50^{NBD} was first purified by heat denaturation of contaminant *E. coli* proteins. Subsequent purification based on the plasmid encoded C-terminal hexahistidine tag was carried out via Ni-NTA affinity chromatography and gel filtration chromatography (see section 3.3.2). The purified protein was analyzed by analytical gel filtration and SDS-PAGE (Figure 7B and C). According to the calibration of the column, Mre11^{HLH}:Rad50^{NBD} eluted as monomeric fraction, when purified without ATP or ATP analog (Figure 7B). The stable protein was approx. 95% pure as validated by SDS-PAGE and the rate of yield conformed 9 mg protein per liter expression culture (Figure 7C). Therefore Mre11^{HLH}:Rad50^{NBD} was suitable for crystallization and biochemical analysis (see below).

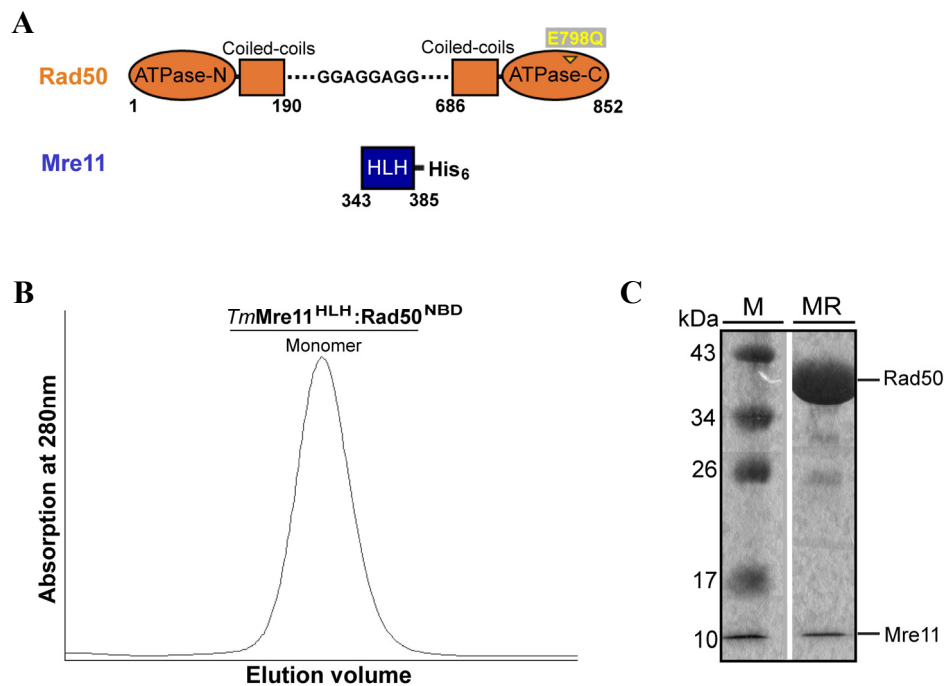


Figure 7: Construct design and purification of *T. maritima* Mre11^{HLH}:Rad50^{NBD}. (A) Construct design of Mre11^{HLH}:Rad50^{NBD} with Rad50 colored in orange and Mre11 colored in blue. The yellow triangle indicates the E798Q substitution in the ATPase domain of Rad50. ATPase-N(C), N(C)-terminal ATPase domain; His₆, hexahistidine tag. (B) Analytical size exclusion chromatography of purified Mre11^{HLH}:Rad50^{NBD} was carried out on a Superdex 200 5/150 GL gel filtration column. Respective elution profile indicates a monomeric state of the protein in the absence of ATP or ATP analog. (C) Validation of purified Mre11^{HLH}:Rad50^{NBD} on a 15% SDS-Gel proves the purity of the protein complex. M, molecular weight marker; MR, Mre11^{HLH}:Rad50^{NBD}.

4.1.2. Crystallization and structure determination of Mre11^{HLH}:Rad50^{NBD}:AMPPNP

To achieve the ATP bound, dimeric state of *T. maritima* Mre11^{HLH}:Rad50^{NBD} with engaged NBD's, ATP was added to the purified monomeric fraction prior to crystallization setup. To stabilize the dimeric state during crystallization and consequently prevent self hydrolysis of ATP, non-hydrolysable analogs like ATP γ S and AMPPNP were used.

Crystallization setups of Mre11^{HLH}:Rad50^{NBD} with ATP γ S and AMPPNP yielded crystals in various conditions (Figure 8A and B). However, crystals containing AMPPNP grew larger in size and to a greater extent in all three dimensions. A single crystal from an initial screen occurred in 20% (w/v) PEG-2000 MME, 0.2 M Trimethylamine N-oxide, 0.1 M Tris pH 8.5 and reached a maximum size of 300 x 100 x 25 μ M (Figure 8B). The crystal formed in space group P1 and contained one AMPPNP bound Rad50^{NBD} dimer together

with Mre11's HLH domain per asymmetric unit. Data were collected to a resolution of 1.9 Å at beamline ID14-1 at the European Synchrotron Radiation Facility (ESRF) (Figure 8C). Due to large structural differences of the NBD domain from the open, nucleotide free Mre11:Rad50^{NBD} complex (PDB entry: 3QG5) and the engaged, AMPPNP bound form, the final structure determination required several attempts of molecular replacement and various short fragments of the open *T. maritima* Mre11:Rad50^{NBD} complex were used. The achieved electron density was of a sufficient quality that the majority of the model could be built automatically. Subsequent recurring cycles of manual model building and refinement yielded the following R-factors: 15.7% for R_{work} and 19.1% for R_{free} . The final model covers in addition to the amino acid sequence of Rad50^{NBD} and Mre11^{HLH}, two molecules of the ATP analog AMPPNP and two molecules of Mg^{2+} . A summary of the crystallographic data and refinement statistics of *T. maritima* Mre11^{HLH}:Rad50^{NBD} bound to AMPPNP are illustrated in Table 10.

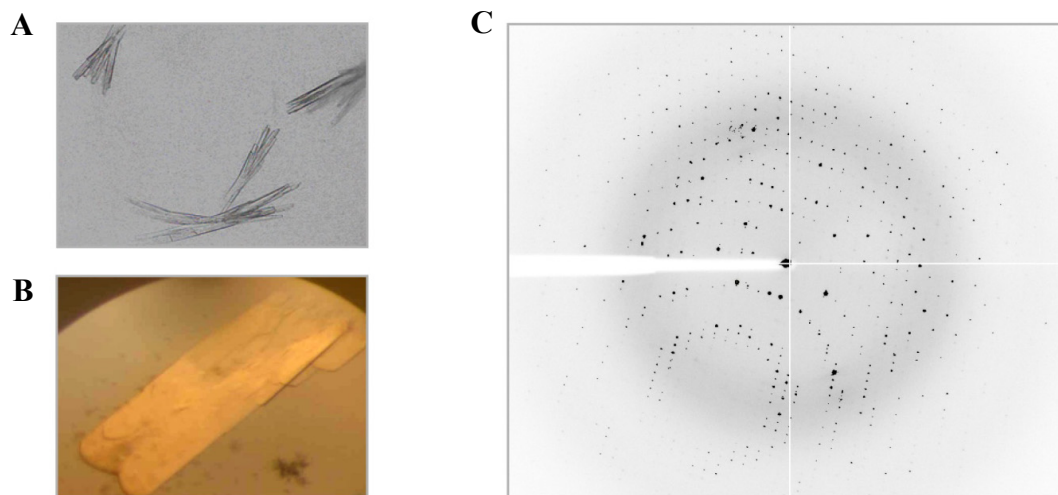


Figure 8: Crystallization of *T. maritima* Mre11^{HLH}:Rad50^{NBD} in nucleotide bound state and data collection of relevant crystals. (A) Mre11^{HLH}:Rad50^{NBD} co-crystallized with ATP γ S lead to rather small branched needle crystals. **(B)** Initial native crystal of Mre11^{HLH}:Rad50^{NBD} bound to AMPPNP occurred in 20% (w/v) PEG-2000 MME, 0.2 M Trimethylamine N-oxide, 0.1 M Tris pH 8.5 and reached a maximum size of 300 x 100 x 25 μm . **(C)** Exemplarily shown image of diffraction pattern of Mre11^{HLH}:Rad50^{NBD} bound to AMPPNP signifies a high resolution data collection.

Table 10: Summary of crystallographic data and refinement statistics of the *T. maritima* Mre11^{HLH}:Rad50^{NBD} complex in its AMPPNP bound state. Data were collected at ID14-1 at the ESRF. Numbers in parentheses correspond to the high resolution shell from 2.03 -1.9 Å.

<i>TmMre11^{HLH} : Rad50^{NBD}:AMPPNP</i>		<i>TmMre11^{HLH} : Rad50^{NBD}:AMPPNP</i>	
Data collection		Refinement	
Space group	P1	Resolution (Å)	45.63 – 1.90
Cell dimensions		No. reflections	64744
a, b, c (Å)	a=49.3	$R_{\text{work}} / R_{\text{free}}$	15.70 / 19.10
	b=68.8	No. atoms	
	c=71.4	Overall	7005
α, β, γ (°)	98.5	Protein	6382
	111.1	AMPPNP	62
	91.9	Magnesium	2
Wavelength (Å)	0.933400	Water	559
Resolution (Å)	50.0-1.9	B-factors (Å²)	
R_{sym} (%)	3.4 (16.9)	Overall	26.90
$I / \sigma I$	24.93 (7.10)	Protein	33.88
Completeness (%)	94.6 (89.9)	AMPPNP	15.05
Redundancy	3.49 (3.51)	Water	39.15
		R.m.s deviations	
		Bond lengths (Å)	0.008
		Bond angles (°)	1.097

4.1.3. Crystal structure of Mre11^{HLH}:Rad50^{NBD} bound to AMPPNP

Although the archaeal Rad50 ATPase domain had been crystallized as an ATP bound dimer before (Hopfner et al., 2000b), this structure lacked the coiled-coil domain and could not give insights into how ATP might impact on the orientation of the coiled-coil domain and the interaction with Mre11. The bacterial *T. maritima*

Mre11^{HLH}:Rad50^{NBD} structure in the presence of AMPPNP offers a much more detailed view of nucleotide coordination and hydrolysis (Figure 9A-C).

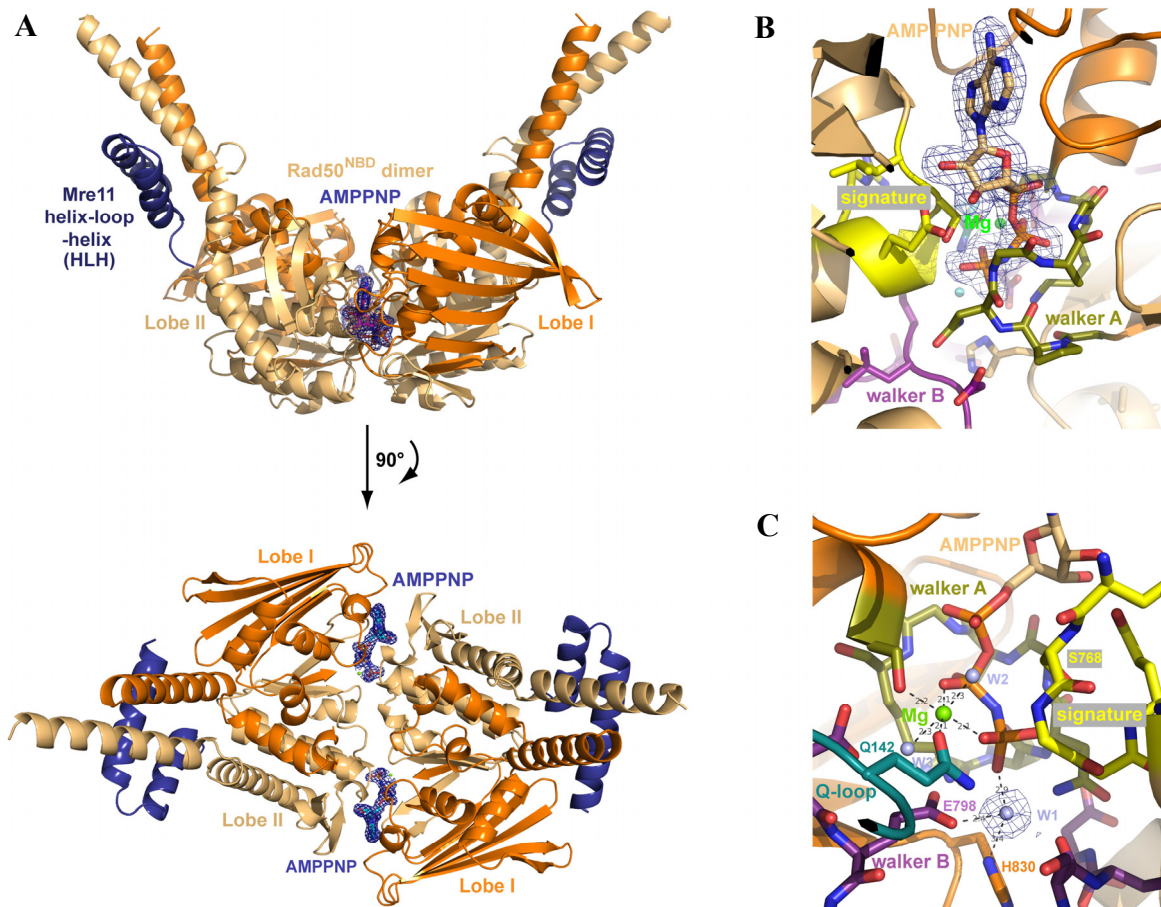


Figure 9: Structure of the *T. maritima* AMPPNP bound Rad50^{NBD} dimer in complex with the HLH domain of Mre11 (Lammens et al., 2011). (A) Two perpendicular views of a ribbon representation of the AMPPNP bound Rad50^{NBD} dimer (orange) in complex with the C-terminal helix-loop-helix (HLH) region of Mre11 (blue). AMPPNP is highlighted and shown with the final $2F_o-F_c$ electron density (contoured at 1σ and colored blue). Lobe I is mainly consisting of the N-terminal ABC segment, whereas lobe II consists mainly of the C-terminal part. (B) and (C) Two views of the ATP binding site with 1.9 \AA $2F_o-F_c$ electron density around AMPPNP (B) or the nucleophilic water (designated as W1) (C). Individual domains and important motifs are highlighted and color coded as following: signature motif (yellow), Walker A (olive), Walker B (purple), Q-loop (turquoise) and Mg^{2+} ion (green sphere). Selected side chains are shown as color-coded sticks.

The Mre11^{HLH}:Rad50^{NBD} structure shows a compact shape with engaged Rad50^{NBD} domains and dimensions of approx. $40 \times 70 \times 100 \text{ \AA}$. The NBDs of Rad50 sandwich two nucleotides and Mg^{2+} in the typical head to tail orientation of lobe I and lobe II. The Walker A motifs bind the three phosphates of the AMPPNP moieties, while the Signature

motifs of the opposing NBDs coordinates the γ -phosphates. Mg^{2+} is coordinated by oxygens from β and γ phosphate, two water molecules and side chain oxygens of S37 (Walker A) and Q142 (Q-loop). A bound water molecule (W1) is suitably located for nucleophilic attack on the γ -phosphate, positioned and activated by hydrogen bonds to E798 (Walker B), H830 (His-switch) and the main chain oxygen of S802 (opposing D-loop) (Figure 9C).

Rad50 binds the C-terminal HLH domain of Mre11 in an interface comprising area of 1334 \AA^2 (designated as interface 1) (Figure 10). Interface 1 is formed by αH and αI of the Mre11 HLH domain binding perpendicularly across Rad50's coiled-coil (Figure 10A). αH^{Mre11} binds only one coiled-coil helix (αH^{Rad50}), while αI^{Mre11} reaches across both coiled-coil helices (αG^{Rad50} and αH^{Rad50}). Interestingly, αH^{Mre11} binds to αH^{Rad50} at a pronounced kink and extended loop, located directly opposite the start of αG^{Rad50} at the other side of the coiled-coil. Thus, the coiled-coil is attached to the NBD not with a continuous helix, but with a structure that may allow for movements between the coiled-coil and Mre11 binding site and the globular part of the ATPase.

The HLH motif and coiled-coil domains bind to each other via an array of aromatic and hydrophobic residues (Figure 10C). αH^{Mre11} and αH^{Rad50} interact through eight aromatic residues (Mre11: Y351, F352, F355, Y358; Rad50: Y707, F714, Y717, F718). The interface is further stabilized mainly by hydrophobic interactions between αI^{Mre11} and αG^{Rad50} but also some specific hydrogen bonds and salt bridges, e.g. between E379^{Mre11} and K180^{Rad50} (Figure 10C). The hydrophobicity in the motifs of interface 1 is highly conserved in all known homologues (Figure 10B). *In vivo* analysis of interface 1 in *S. cerevisiae* also revealed that mutations within the Mre11 HLH motif predicted to affect interface 1 (*ScMre11*: L474R, I487R, I491R) result in sensitivity to methylmethanesulfonate, hydroxyurea and camptothecin (Lammens et al. 2011).

Given that the helix following the Q-loop and the subsequent coiled-coiled domains are well ordered with clearly interpretable electron density, comparison of nucleotide bound and -free states of the interaction site between Mre11 and Rad50 is feasible (Figure 10D and E). Superposition of the Mre11^{HLH}:Rad50^{NBD}:AMPPNP and the nucleotide free Mre11:Rad50^{NBD} complex (PDB entry: 3QG5) on Rad50's lobe II point towards both the coiled-coil structure of Rad50^{NBD} and the interaction interface 1 being largely unaltered upon nucleotide binding (Figure 10D).

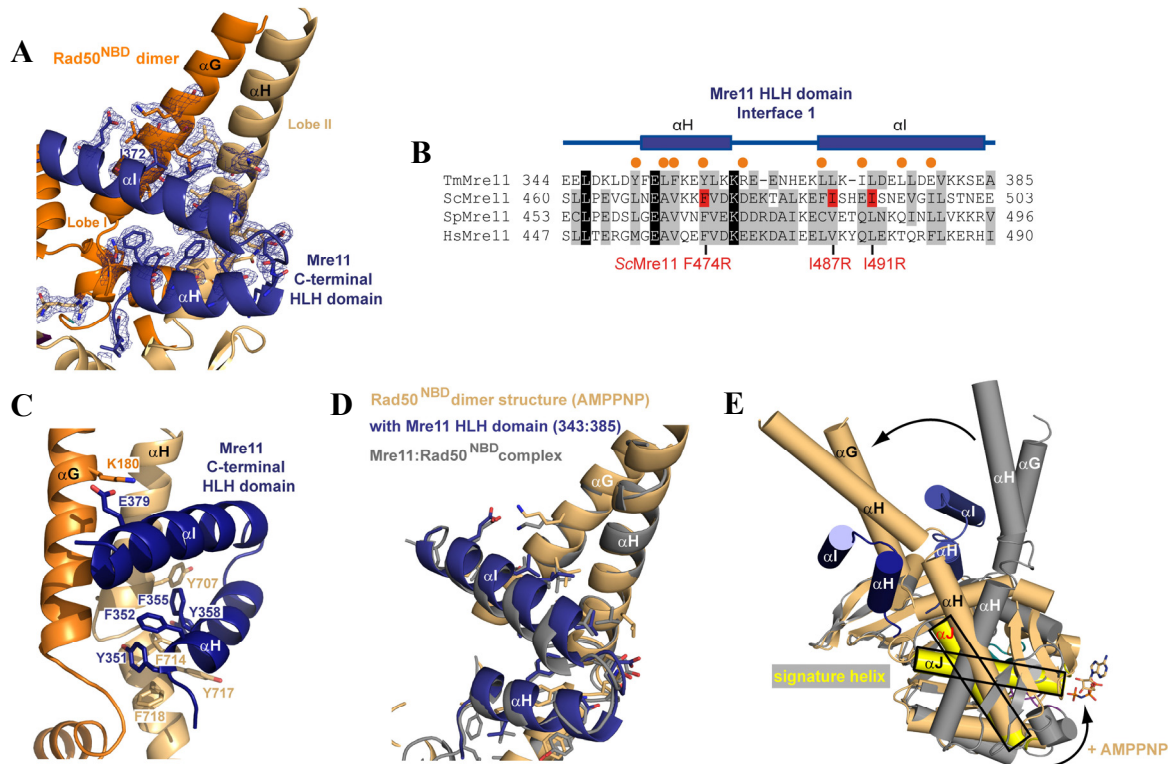


Figure 10: Detailed view of *T. maritima* Mre11^{HLH}:Rad50^{NBD} interface 1 and conformational changes upon nucleotide binding. (A) Detailed view of the Mre11 HLH motif (blue) and its interaction with the base of the Rad50 coiled-coil (orange). Selected side chains are shown as color-coded sticks and the 2F_o-F_c electron density map contoured at 1.0 σ, is shown in blue around the interacting residues. (B) Sequence alignment of the Mre11 HLH domain (αH and αI) involved in Rad50^{NBD} binding (interface 1). Orange spheres represent residues implicated in Mre11^{HLH}:Rad50^{NBD} interaction. Yeast mutations (*ScMre11*: F474R, I487R, I491R) introduced to analyze interface 1 *in vivo* are highlighted in red (Lammens et al. 2011). (C) Close up view of aromatic and hydrophobic interactions of αH^{Mre11} and αH^{Rad50} and salt bridge formation of αI^{Mre11} and αG^{Rad50}. Relevant residues are labeled and shown as color-coded sticks. (D) Superposition of Rad50^{NBD} from the open Mre11:Rad50^{NBD} (PDB entry: 3QG5; grey) and AMPPNP bound (blue/orange) crystal structures at Lobes II shows that the coiled-coil structure and interaction interface 1 is not directly modulated by AMPPNP binding. Selected side chains are shown as color-coded sticks. (E) Superposition of the nucleotide free (PDB entry: 3QG5; grey) and AMPPNP bound forms of Rad50^{NBD} via Lobe I shows that AMPPNP binding induces a large, approx. 50° rotation between Lobe I and Lobe II, leading to a rigid body movement (arrow) of the HLH and coiled-coil domain with respect to the ATP binding interface of Rad50.

ATP binding not only tightly engages the two Rad50 NBDs, but induces a second conformational change within the NBDs, resulting in an approx. 50° rotation of the signature motif helix (Figure 10E) with respect to the Walker motifs. This rotation is the result of Q142 (Q-loop) binding to Mg²⁺, inducing a conformation within the NBDs that enables tight NBD-NBD engagement. As a consequence, the coiled-coil and the interacting HLH domain of Mre11 undergo a “rigid body” rotation by approx. 50° with respect to ATP binding lobe I.

Formation of the engaged NBDs strongly affects the angle between the two coiled-coils protruding from the DNA binding catalytic head, consistent with scanning force microscopy of human MRN, where DNA binding was shown to alter the angle between two coiled-coils of about 60°. Comparing the angle between coiled-coils in the open nucleotide free conformation (~120°) and the ATP-bound closed state (~60°) there is also a difference of about 60°.

4.1.4. Crystallization and structure determination of Mre11^{HLH}:Rad50^{NBD}:ADP[VO₄]³⁻

To gain insights into the mechanism of phosphoryl transfer and therefore insights into the transition state of Rad50's ATPase, *T. maritima* Mre11^{HLH}:Rad50^{NBD} was co-crystallized with ADP and the orthovanadate anion [VO₄]³⁻. The vanadate ion adopts trigonal bipyramidal coordination and has very similar size and charge to inorganic phosphate. Therefore the vanadate ion is suitable to mimic the conformation of the γ -phosphate group at the transition state expected for phosphoryl transfer (Smith and Rayment, 1996).

Crystal setup of Mre11^{HLH}:Rad50^{NBD} bound to ADP[VO₄]³⁻ yielded crystals in several conditions that were epitaxial twinned (Figure 11A). Crystals formed in space group P2₁ and contained the Rad50^{NBD} dimer bound to ADP[VO₄]³⁻ plus Mre11's HLH domains per asymmetric unit. Data were collected to a resolution of 2.9 Å at ID14-4 at the European Synchrotron Radiation Facility (ESRF) (Figure 11B). In fact, the collected data were of a low quality and low completeness caused by high mosaicity and, anisotropy. However, the structure of the Mre11^{HLH}:Rad50^{NBD}:ADP[VO₄]³⁻ complex was solved by molecular replacement using the previously solved Mre11^{HLH}:Rad50^{NBD} structure in its AMPPNP bound state without ligand (see section 4.1.2). The difference density observed for the coiled-coil and HLH domain was rather weak and not suitable for model building. Therefore iterative cycles of refinement were carried out against the Mre11^{HLH}:Rad50^{NBD}:AMPPNP model omitting AMPPNP, coiled-coil and HLH region and yielded in following R-factors: 28.87% for the R_{work} and 32.80% for the R_{free}. A summary of the crystallographic data and refinement statistics of *T. maritima* Mre11^{HLH}:Rad50^{NBD} bound to ADP[VO₄]³⁻ are presented in Table 11.

Table 11: Summary of crystallographic data and refinement statistics of the *T. maritima* Mre11^{HLH}:Rad50^{NBD} complex bound to ADP[VO₄]³⁻. Data were collected at the ID14-4 at the ESRF. Numbers in parentheses correspond to the high resolution shell from 3.04-2.90 Å. Refinement was carried out against the Mre11^{HLH}:Rad50^{NBD} model without ligand, Rad50 coiled-coil and Mre11 HLH region.

<i>TmMre11^{HLH}: Rad50^{NBD}:ADP[VO₄]³⁻</i>		<i>TmMre11^{HLH}: Rad50^{NBD}:ADP[VO₄]³⁻</i>	
Data collection		Refinement	
Space group	P2 ₁	Resolution (Å)	44.24-2.90
Cell dimensions		No. reflections	21525
a, b, c (Å)	a=69.4	<i>R</i> _{work} / <i>R</i> _{free}	28.87/32.80
	b=51.8	No. atoms	
	c=134.3	Protein	4832
α, β, γ (°)	90.0	B-factors (Å²)	
	98.6	Protein	111.46
	90.0	R.m.s deviations	
Wavelength (Å)	0.9395	Bond lengths (Å)	0.010
Resolution (Å)	50.0-2.9	Bond angles (°)	1.180
<i>R</i> _{sym} (%)	5.4 (84.2)		
<i>I</i> / σ <i>I</i>	18.34 (2.04)		
Completeness (%)	90.0 (99.1)		
Redundancy	4.05 (4.07)		

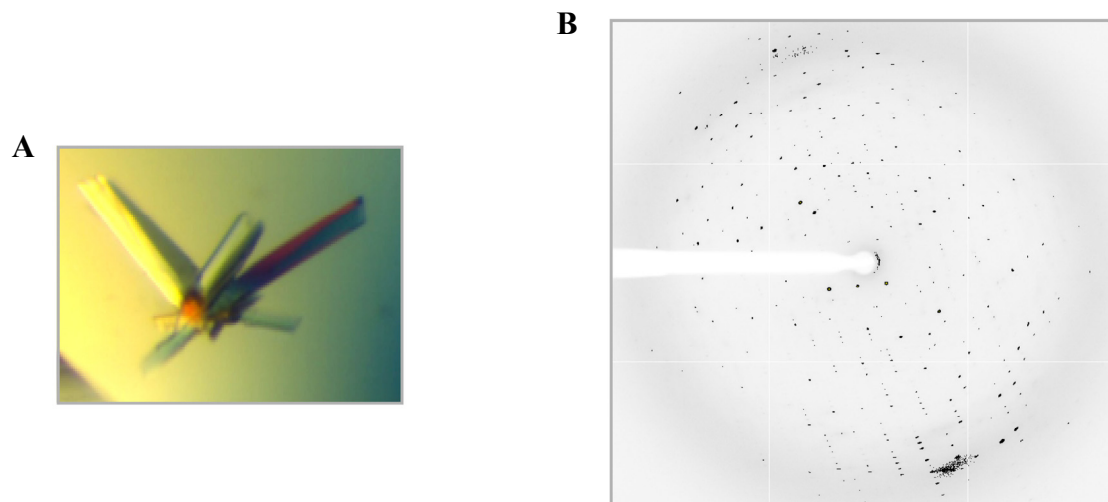


Figure 11: Crystallization and data collection of relevant *T. maritima* Mre11^{HLH}:Rad50^{NBD}:ADP[VO₄]³⁻ crystals. (A) Initial native crystal of Mre11^{HLH}:Rad50^{NBD} bound to ADP[VO₄]³⁻ occurred in 0.1 M MMT buffer pH 9.0 and 25% (v/v) PEG 1500 and were epitaxially twinned. **(B)** Exemplarily shown image of diffraction pattern of Mre11^{HLH}:Rad50^{NBD}:ADP[VO₄]³⁻ indicates the low quality of the obtained data, mainly induced by high mosaicity and anisotropy of the crystal.

The obtained R-factor of 28.87% and 32.80% for R_{work} and R_{free} is still out of acceptable ranges and may improve with some rebuilding, e.g. of the coiled-coil and HLH domain and/or better data. However, the refined model fits very well into the $2F_o - F_c$ density map. The only major difference density $\geq 3.0 \sigma$ present after refinement clearly belongs to the co-crystallized ligand (Figure 12A). As seen in the close up view the vanadate ion is coordinated equally to the γ -phosphate of the AMPPNP by the signature motifs of the opposing NBDs (Figure 12B). Likewise, the entire ATPase domain shows no large structural alterations upon approaching phosphoryl transfer. Consequently, the transition from the ATP bound to the phosphoryl transfer state does not seem to have impact on the conformation of Rad50's ATPase domain.

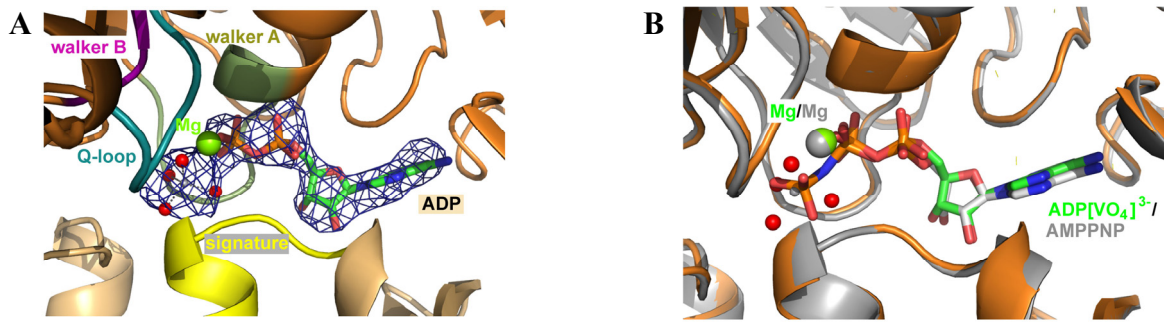


Figure 12: Structure of the *T. maritima* Mre11^{HLH}:Rad50^{NBD} complex bound to ADP[VO₄]³⁻ and illustration of its transition state. (A) Close up view of the ATP binding site of Mre11^{HLH}:Rad50^{NBD} with the F_o-F_c map (contoured at 2.0 σ and colored in blue) refined against the model without ligand showing a clearly defined electron density for ADP and the trigonal [VO₄]³⁻ ion (vanadate, gray sphere; oxygen, red spheres). Individual domains and important motifs are highlighted and annotated. **(B)** Superposition of the ATP binding region of Mre11^{HLH}:Rad50^{NBD} in AMPPNP (grey) and ADP[VO₄]³⁻ (orange) bound state. The vanadate ion (vanadate, gray sphere; oxygen, red spheres) mimics the conformation of the γ -phosphate group at the transition state expected for phosphoryl transfer. The close up view of the two nucleotide bound states shows no structural alteration of the ATP binding domain upon upcoming phosphoryl transfer.

4.2. Mre11:Rad50^{NBD} of *T. maritima*

4.2.1. Cloning and enzymatic characterization of Mre11:Rad50^{NBD}

Mre11:Rad50^{NBD} of *T. maritima* covers the nucleotide binding domain of Rad50 including approx. 50 amino acids of the Mre11 binding coiled-coil region (aa 1-190 and aa 686-852; denoted as Rad50^{NBD}) and nearly full length Mre11 (aa M7-385; denoted as Mre11), including phosphodiesterase, capping and helix-loop-helix (HLH) domain (see section 3.2.1). The two ends of Rad50's shortened coiled-coils are covalently fused by a short linker as described earlier for the Mre11^{HLH}:Rad50^{NBD} construct (see section 4.1.1). Mre11 lacks the first 6 amino acids of the N-terminus as sequence alignment with various bacterial and archaeal Mre11 revealed weak homology in this unstructured region. Construct design and cloning was done in previous work by Christian Schiller and Derk Bemeleit (AG Hopfner, Gene Center, Munich).

To clarify the functionality of the Mre11:Rad50^{NBD} complex, enzymatic activity assays including analysis of ATP hydrolysis, DNA affinity and nucleolytic cleavage of DNA were performed (Figure 13). To prevent unintentional ATP hydrolysis and nuclease

activity during DNA binding experiments, both a nuclease deficient (H94Q^{Mre11} substitution) and an ATPase deficient (E798Q^{Rad50} substitution) mutant were designed.

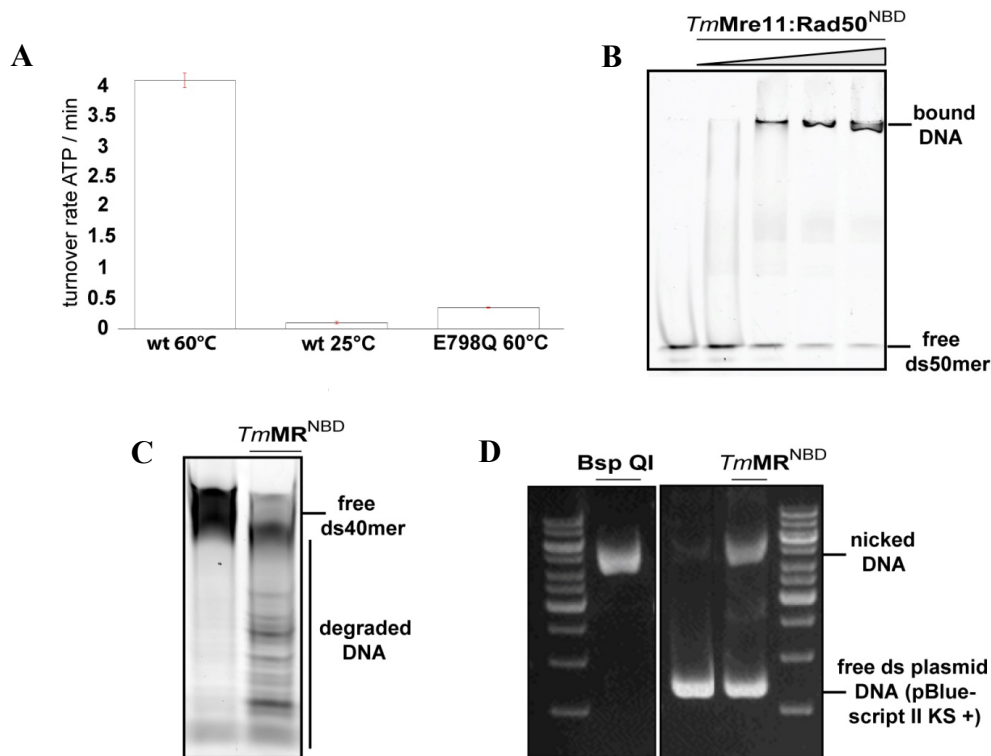


Figure 13: Enzymatic characterization of *T. maritima* Mre11:Rad50^{NBD}. (A) ATP hydrolysis activity of thermophilic Mre11:Rad50^{NBD} (denoted as wt) at 60°C or 25°C reveals temperature dependent activity of the protein. A Walker B motif mutant (E798Q) in Rad50 rules out contaminating activities. Error bars depict +/- standard deviation of three independent experiments. (B) DNA affinity of Mre11:Rad50^{NBD} using Electrophoretic Mobility Shift Assay (EMSA). Following protein concentrations (0, 0.5, 2.0, 4.0 and 6.0 μM respectively) were analyzed and 10 nM of 6-FAM 5' -labeled double stranded DNA (50mer) was used. (C) (Exo)nuclease activity of thermophilic Mre11:Rad50^{NBD} at 60°C shows degradation of 5' -fluorescein labeled double stranded DNA (D) Analysis of endonuclease activity of thermophilic Mre11:Rad50^{NBD} at 60°C confirm endonucleolytic cleavage on double stranded plasmid DNA (pBluescript II KS +) containing secondary structures like hairpins. Resulting nicked DNA was proven by the nicking enzyme Nt. Bsp QI.

Given that *T. maritima* belongs to the thermophilic bacteria with an optimum growth at approx. 80°C enzymatic activities were mainly examined at higher temperatures. ATP hydrolysis at 25°C revealed no measurable turnover rate of ATP per min whereas at 60°C approx. 4 ATP per min were hydrolyzed by Mre11:Rad50^{NBD} (Figure 13A). Beside the functionality of the ATPase, Mre11:Rad50^{NBD} showed a moderate, temperature independent, affinity to double stranded DNA as observed by Electrophoretic Mobility

Shift Assay (EMSA) (Figure 13B). In addition, short double stranded DNA oligomers were degraded by Mre11:Rad50^{NBD} and secondary DNA structures like hairpins were endonucleolytically cleaved resulting in nicked DNA (Figure 13C and D). Briefly, the Mre11:Rad50^{NBD} complex of *T. maritima* showed complete functionality with a characteristically rather moderate enzymatic activity (Hopfner et al., 2000a).

4.2.2. Analysis of Mre11:Rad50^{NBD} interface 2

Although *T. maritima* Mre11:Rad50^{NBD} showed enzymatic activity and the structure of the open, nucleotide free complex could be determined due to previous work by Katja Lammens and Derk Bemeleit (AG Hopfner, Gene Center, Munich), attempts to crystallize the complex in presence of AMPPNP, ATP γ S or other ATP analogs failed. This was likely because of equilibrium between ATP bound (closed) and free (open) states which could be observed and examined via SAXS (Lammens et al., 2011). To come up with a solution to adjust the equilibrium in direction to the nucleotide bound (closed) state, the structures of AMPPNP bound Mre11^{HLH}:Rad50^{NBD} with engaged NBDs and the nucleotide free Mre11:Rad50^{NBD} complex were compared.

Beside the earlier described interface 1 (see section 4.1.3), Rad50 binds Mre11 in a second, smaller area comprising 686 Å² (designated as interface 2) (Figure 14A and B). Interface 2 is formed between one face of Mre11's capping domain and the bottom side of Rad50's Lobe II. This interface is predominantly polar, although W758^{Rad50} and I760^{Rad50} bind a small hydrophobic patch at the core of this interface (F291^{Mre11}). Interestingly, a part of the interface is mediated by the signature motif, which becomes bound by ATP in the engaged conformation of the NBDs (Figure 14A). Consequently, interface 2 could transiently stabilize the open conformation, as seen in the crystal structure of the nucleotide free Mre11:Rad50^{NBD} complex (PDB entry: 3QG5).

To test the possibility that destabilizing interface 2 could increase the efficiency of the transition into the nucleotide bound, closed form, several mutations were introduced in Mre11 and Rad50 to weaken the interaction in this particular interface (F291S^{Mre11}, Y277R^{Mre11}, I760C^{Rad50}, W758A^{Rad50}) (Figure 14A and B).

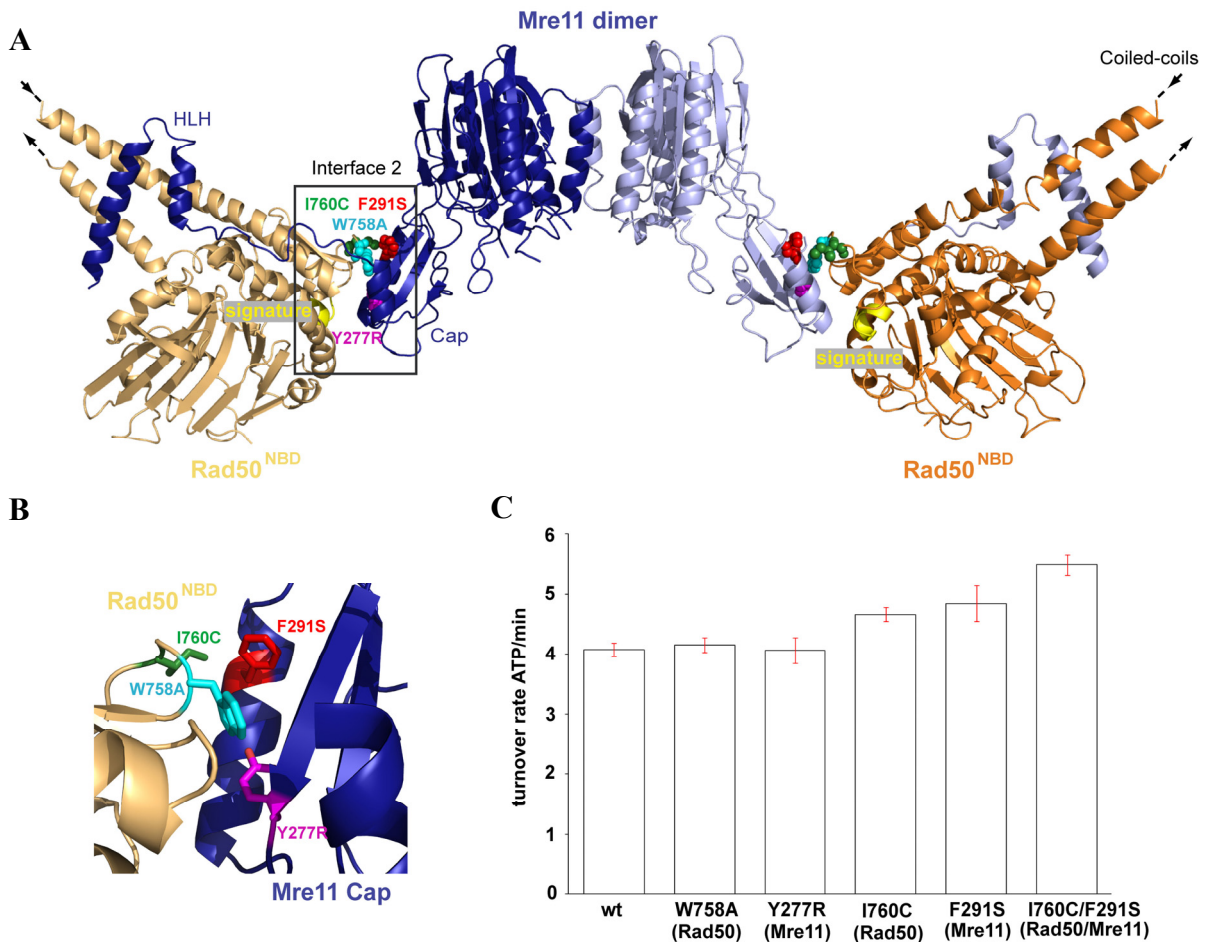


Figure 14: Analysis of *T. maritima* Mre11:Rad50^{NBD} interface 2. (A) Ribbon representation of Mre11:Rad50^{NBD} (PDB entry: 3QG5) in front view orientation (Mre11 shown in blue, Rad50 shown in orange). Interface 2 is depicted by a black box. Mutated residues in interface 2 are illustrated as spheres and highlighted in red (F291S^{Mre11}), green (I760C^{Rad50}), cyan (W758A^{Rad50}) and magenta (Y277R^{Mre11}), respectively. The signature motif is highlighted and colored in yellow. (B) Close up view of interface 2 showing the four residues selected for mutational analysis. Color coded corresponding to Figure 14A. (C) ATP hydrolysis activity of five interface 2 Mre11:Rad50^{NBD} mutant complexes compared to wildtype (wt) activity at 60°C. The I760C^{Rad50} mutant as well as the F291S^{Mre11} mutant possess a slightly increased ATPase activity (116% and 121% compared to wt), whereas the I760C^{Rad50}/F291S^{Mre11} double mutant shows 130% of the wt activity. Error bars depict +/- standard deviation of three independent experiments.

Analysis of the ATP hydrolysis activity of respective mutants revealed a slight, but statistical significant increase in activity for the F291S^{Mre11} and I760C^{Rad50} mutants (116% and 121% compared to wt activity respectively) and even more (130% of wt activity) when both F291^{Mre11} and I760^{Rad50} were mutated. Since ATP hydrolysis by Rad50^{NBD} requires formation of a tightly engaged NBD dimer with sandwiched ATP molecules, these data support the suggestion that weakened interface 2 leads to an adjustment of equilibrium in direction of the nucleotide bound, closed state.

4.2.3. ATP induced engagement of Rad50 NBDs

Even though mutations in *T. maritima* Mre11:Rad50^{NBD} interface 2 seemed to adjust equilibrium in direction to the closed, ATP bound state, attempts to obtain a homogeneous population with engaged NBDs by addition of various amounts of ATP γ S, AMPPNP, ADP plus BeF₃ or using a Walker B E798Q mutation in combination with ATP, had been unsuccessful.

To trap Mre11:Rad50^{NBD} in the ATP bound conformation, the earlier described cysteine mutation I760C^{Rad50} together with N64C^{Rad50} was used for site-specific crosslinking (Figure 15). Both residues are predicted to be far apart in the nucleotide free form (approx. 110 Å) but come close together in the ATP bound dimer of Rad50^{NBD} (approx. 8 Å) (Figure 15A). This enables crosslinking analysis with the short bifunctional sulfhydryl directed crosslinker Bis-Maleimidoethane (BMOE) (Figure 15C) (see section 3.3.6). To independently verify the clamping movement of the NBDs another pair of cysteine residues were introduced in Rad50^{NBD}. D804C and H830C are located within the His-switch and D-loop region in the ATPase domain of Rad50 and are perfectly suited for disulfide bond formation (Figure 15A and B) (see section 3.3.7).

Using I760C^{Rad50} plus N64C^{Rad50} the two NBDs could be crosslinked very efficiently in the presence (approx. 65%), but not in the absence of ATP (Figure 16A). To see whether the crosslinked protein has a structure similar to the ATP bound Mre11:Rad50^{NBD} complex, BMOE crosslinked protein was prepared in the presence of ATP, purified by gel filtration to remove unbound ATP and concentrated to perform small angle x-ray scattering (SAXS) experiments (see section 3.4.4). Nucleotide free and ATP γ S bound Mre11:Rad50^{NBD} was previously analyzed via SAXS by Katja Lammens and Derk Bemeleit, enabling comparison of crosslinked protein to the ATP bound and unbound form (Lammens et al., 2011). Indeed, the solution structure of the crosslinked protein is very similar to the ATP γ S bound protein (Figure 16B and C), validating the idea that the crosslink stabilizes the closed conformation. This proves that addition of ATP or ATP analogs induces a conformation in MR's catalytic head with engaged NBDs, thereby the transient interface 2 is disrupted.

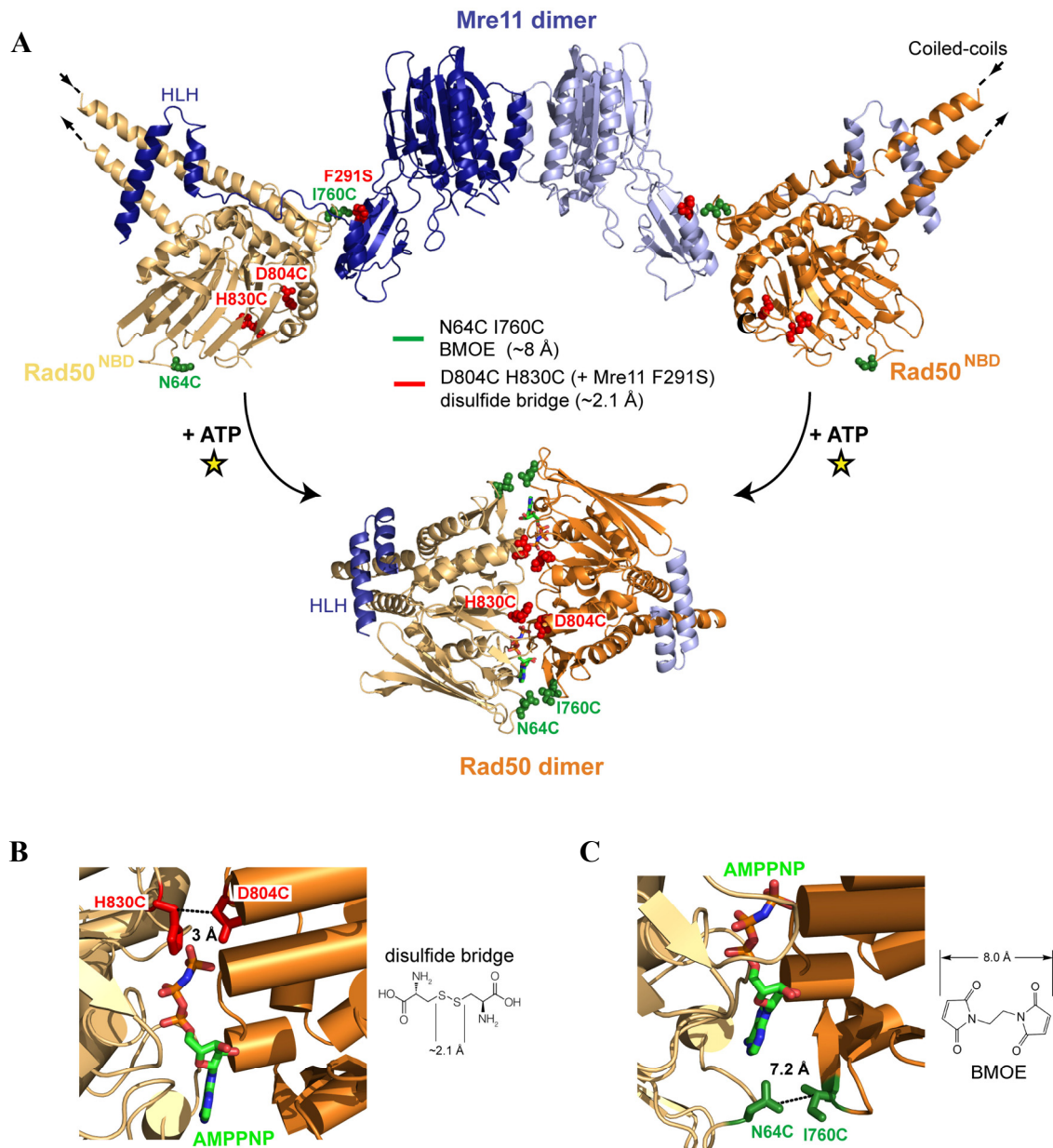


Figure 15: Cysteine mutations introduced in *T. maritima* Mre11:Rad50^{NBD} to enable site-specific crosslinking and disulfide bonding. (A) Cysteine mutations introduced in Rad50^{NBD} to test formation of the ATP bound Rad50 dimer, are illustrated as colored spheres. Sites are widely separated in the open form (upper crystal structure; PDB entry: 3QG5), but perfectly oriented for crosslinking (I760C, N64C, colored green) or disulfide bonding (D804C, H830C, colored red) in the ATP bound form (lower crystal structure; Mre11^{HLH}:Rad50^{NBD}). F291S^{Mre11} (colored red) was additionally mutated for enhanced disulfide bonding by weakened interface 2. Mre11 and Rad50 are color coded according to Figure 9 and Figure 14. (B) Close up view of residues D804 and H830 (colored as red sticks) in Rad50^{NBD} selected for cysteine mutation. The distance between the two residues is suitable to form disulfide bonds (inset: disulfide bridge). (C) Close up view of residues I760 and N64 in Rad50^{NBD} (colored green) selected for cysteine mutation. The distance between the two residues is suitable for crosslinking with a short bifunctional sulfhydryl directed crosslinker (inset: BMOE).

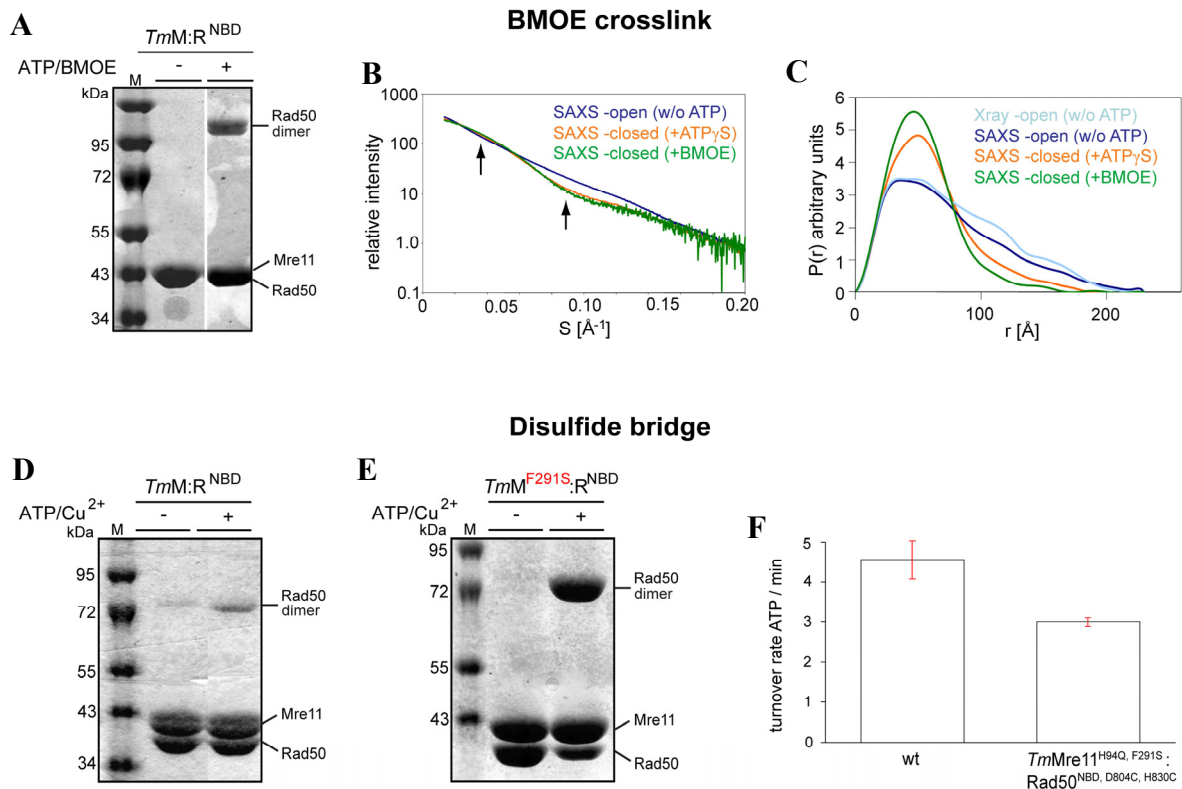


Figure 16: Analysis of site-specific crosslinking and disulfide bridging of *T. maritima* Mre11:Rad50^{NBD}. (A) Non-reducing coomassie stained SDS-PAGE of the Mre11:Rad50^{NBD, N64C, I760C} crosslinking experiment using Bis-Maleimidoethane (BMOE). The crosslinker forms a covalently connected Rad50^{NBD} dimer in an ATP dependent manner. Approx. 65% of Mre11:Rad50^{NBD} can be trapped in the ATP bound state on the basis of this method. (B) Superposition of experimental SAXS curves of Mre11:Rad50^{NBD} in the nucleotide free (blue) or ATPγS bound (orange) state and Mre11:Rad50^{NBD, I760C, N64C} crosslinked with BMOE (green). The scattering curve of the crosslinked complex shows an even larger alteration in profile (black arrows), indicating a more compact and globular shape of the complex. (C) Electron pair distance distribution function P(r) in the absence of nucleotide corresponds well to the crystal structure derived P(r) (PDB entry: 3QG5). The BMOE crosslinking leads to an increase of short distances and decrease of long distances. Some residual long distances indicate a residual heterogeneous mixture that fits the data where approx. 35% of the complex is not crosslinked. (D) Formation of ATP bound engaged Rad50^{NBD, D804C, H830C} is tested by ATP/Cu²⁺ dependent disulfide bond formation and validated by non-reducing Coomassie stained SDS-PAGE. (E) Modulating the Mre11:Rad50^{NBD} interface 2 by Mre11^{F291S} results in dramatically increased disulfide bond formation efficiency, consistent with the idea, that interface 2 stabilizes the open form and is disrupted in the closed form. (F) ATP hydrolysis activity of the Mre11^{H94Q, F291S}:Rad50^{NBD, D804C, H830C} mutant complex compared to wildtype (wt) activity at 60°C. According cysteine mutations in the His-switch and D-loop region lead to a slight decrease of ATP hydrolysis activity (66% compared to wt, respectively). Error bars depict +/- standard deviation of six independent experiments.

The proposed clamp movement can also be seen by ATP induced formation of a disulfide bond between D804C^{Rad50} and H830C^{Rad50}, which are ideally positioned at opposite interface loops in the ATP bound form of NBDs (Figure 16D). Although D804C^{Rad50} and H830C^{Rad50} are located within the His-switch and D-loop region which

play a role in ATP dependent dimer formation of NBDs and in positioning of the attacking water molecule, the cysteine mutations only slightly decrease ATP hydrolysis activity and the proteins remained approx. 68% active (Figure 16F).

The high efficiency of I760C^{Rad50}/N64C^{Rad50} in the presence of BMOE compared to the disulfide bond could arise from the fact that I760^{Rad50} is located in interface 2. If interface 2 stabilizes the open form, destabilizing interface 2 will increase the efficiency of formation of the closed form. To test this idea, the earlier described mutation F291S (F291^{Mre11} interacts with I760^{Rad50} in interface 2) was additionally introduced into Mre11. While efficient disulfide bond formation is still not observed in the absence of ATP, the NBDs can now be efficiently crosslinked (approx. 65%) by disulfide bond formation (Figure 16E). Disulfide bridged Mre11^{F291S}:Rad50^{NBD, D804C, H830C} is subsequent designated as Mre11:Rad50^{NBD (S-S)}.

The ability to trap Mre11:Rad50^{NBD} in its nucleotide bound state was a keystone for further analysis of the closed conformation. Due to the fact that the formation of the disulfide bridged Mre11:Rad50^{NBD (S-S)} complex was not dependent on chemical crosslinking (BMOE) further investigations were done on the basis of the disulfide bonded protein.

4.3. Mre11:Rad50^{NBD} of *T. maritima* trapped in its ATP/ADP bound state

4.3.1. Crystallization and structure determination of Mre11:Rad50^{NBD (S-S)}

To trap *T. maritima* Mre11^{F291S}:Rad50^{NBD, D804C, H830C} in the nucleotide bound, closed state, the complex was disulfide bridged in the presence of ATP prior to crystallization setup. This stabilization facilitated the crystallization process. Crystals appeared after approx. 9 days in several high salt conditions containing ammonium sulfate (Figure 17A). Single crystals grew in all three dimensions and reached a maximum size of 70 x 70 x 50 μ M. After optimization these crystals diffracted to 2.6 Å resolution in space group P3₂21 at beamline X06SA at the Swiss Light Source (SLS) (Figure 17B and C). Each asymmetric unit contained half a M₂R^{NBD (S-S)}₂ complex and the complete heterotetrameric complex was generated via a crystallographic two-fold axis.

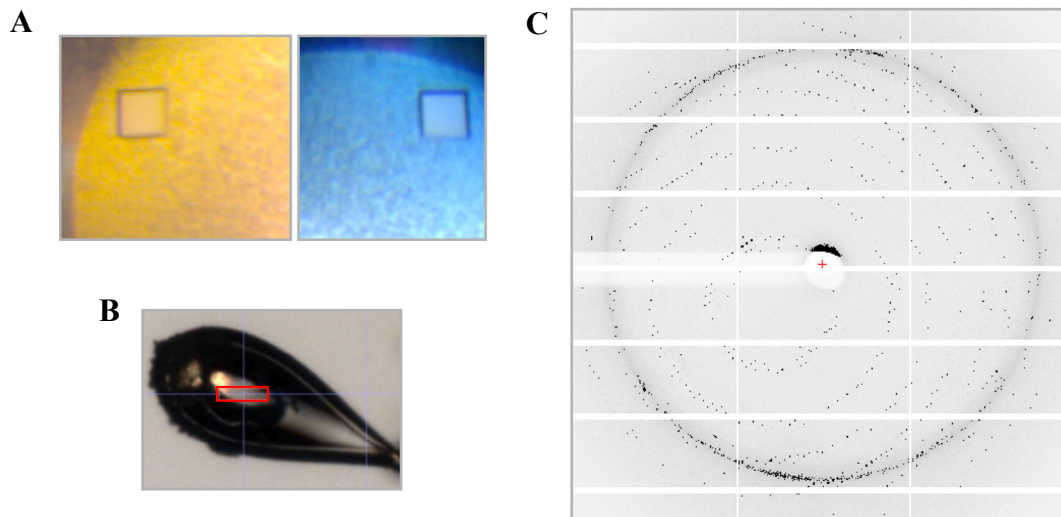


Figure 17: Crystallization of *T. maritima* Mre11:Rad50^{NBD (S-S)} and data collection of relevant crystals. (A) Optimized native crystals of Mre11:Rad50^{NBD (S-S)} occurred in 2.2 M ammonium sulfate and 0.2 M diammonium tartrate and reached a maximum size of 70 x 70 x 50 μM . (B) Flash frozen Mre11:Rad50^{NBD (S-S)} crystal in nylon cryo loop (Hampton Research). The image was taken firsthand of data collection at beamline X06SA at the SLS. The red box indicates the position of x-ray exposure and data collection of the crystal. (C) Exemplarily shown diffraction pattern of the Mre11:Rad50^{NBD (S-S)} crystal indicates high quality data to 2.6 \AA resolution.

Due to large structural differences between the open, nucleotide free (PDB entry: 3QG5) and the closed, nucleotide bound form, molecular replacement was performed with several small Rad50^{NBD} fragments of the previously solved Mre11^{HLH}:Rad50^{NBD}:AMPPNP structure (see section 4.1.2). Although two 3-dimensional structures of the *Tm*Mre11 dimer are provided by the Protein Data Bank (PDB entry: 2Q8U and 3QG5 respectively), several loops and some important regions were missing in these structures. In order to obtain a suitable model to search for the Mre11 dimer by molecular replacement the core domain of *T. maritima* Mre11 (aa M7-325) was crystallized. Crystals of Mre11^{core} formed in space group P6₂21 and diffracted to 2.8 \AA resolution at beamline X06SA at the Swiss Light Source (SLS). Each asymmetric unit contained one Mre11 monomer and the Mre11 dimer was generated by a two-fold axis. Crystallographic data and refinement statistics for *T. maritima* Mre11^{core} are presented in Table 12.

Table 12: Summary of crystallographic data and refinement statistics of the *T. maritima* Mre11^{core} domain bound to manganese. Data were collected at the X06SA beamline at the SLS. Numbers in parentheses correspond to the high resolution shell from 2.89-2.81 Å.

<i>TmMre11^{core}</i>		<i>TmMre11^{core}</i>	
Data collection		Refinement	
Space group	P6 ₁ 22	Resolution (Å)	46.06-2.81
Cell dimensions		No. reflections	17309
a, b, c (Å)	a=138.9	$R_{\text{work}} / R_{\text{free}}$	18.69/24.06
	b=138.9	No. atoms	
	c=123.1	Overall	2560
α, β, γ (°)	90	Protein	2543
	90	Manganese	2
	120	Water	12
Wavelength (Å)	1.000	Sulfate	2
Resolution (Å)	46.06-2.81	B-factors (Å²)	
R_{sym} (%)	11.5 (54.8)	Overall	36.43
$I / \sigma I$	17.82 (4.57)	Protein	37.36
Completeness (%)	98.2 (98.3)	Water	28.26
Redundancy	8.48 (8.52)	R.m.s deviations	
		Bond lengths (Å)	0.008
		Bond angles (°)	1.230

On the basis of Rad50^{NBD} (Mre11^{HLH}:Rad50^{NBD}) and Mre11^{core} the structure of Mre11:Rad50^{NBD(S-S)} could be determined by molecular replacement. Some parts including e.g. the coiled-coil region and the Mre11 C-terminus (aa 326-383) were built manually. Iterative cycles of manual model building and refinement yielded in following R-factors: 20.9% for R_{work} and 24.6% for R_{free} . The final model covers half a tetrameric Mre11:Rad50^{NBD} complex, one ADP molecule, 2 Mn²⁺ and one Mg²⁺ ion, nine sulfate and one phosphate ion. Crystallographic data and refinement statistics of *T. maritima* Mre11:Rad50^{NBD(S-S)} are illustrated in Table 13.

Table 13: Summary of crystallographic data and refinement statistics of the *T. maritima* Mre11:Rad50^{NBD (S-S)} complex in its ATP/ADP bound state. Data were collected at the X06SA beamline at the SLS. Numbers in parentheses correspond to the high resolution shell from 2.77-2.61 Å.

<i>TmMre11 : Rad50^{NBD (S-S)}</i>		<i>TmMre11 : Rad50^{NBD (S-S)}</i>	
Data collection		Refinement	
Space group	P3 ₂ 21	Resolution (Å)	49.12 – 2.60
Cell dimensions		No. reflections	68086
a, b, c (Å)	a=121.5 b=121.5 c=134.9	$R_{\text{work}} / R_{\text{free}}$	20.90 / 24.60
α, β, γ (°)	90.0 90.0 120.0	No. atoms	
Wavelength (Å)	1.000	Overall	5978
Resolution (Å)	50.0-2.6	Protein	5859
R_{sym} (%)	5.4 (54.9)	ADP	26
$I / \sigma I$	19.32 (2.56)	Magnesium	1
Completeness (%)	99.7 (98.4)	Manganese	2
Redundancy	5.1 (4.8)	Water	33
		Sulfate	9
		Phosphate	1
		B-factors (Å²)	
		Overall	66.01
		Protein	66.09
		ADP	45.62
		Water	61.25
		R.m.s deviations	
		Bond lengths (Å)	0.009
		Bond angles (°)	1.240

4.3.2. Crystal structure of Mre11:Rad50^{NBD (S-S)} in its ATP/ADP bound state

The *T. maritima* Mre11:Rad50^{NBD (S-S)} complex structure shows a compact ring shape with striking differences to the previously solved structure of Mre11:Rad50^{NBD} in the ATP free, open state (Figure 18A and B) (Möckel et al., 2011). The core of the complex has dimensions of 75 x 80 x 92 Å and consists of the phosphodiesterase and capping domains of the Mre11 dimer as well as the ATP bound, engaged NBDs of Rad50. The NBDs of Rad50 sandwich two nucleotides and Mg²⁺ in the typical head to tail orientation of lobe I and lobe II (Hopfner et al., 2000b). The formed disulfide bond between the introduced cysteine residues C804^{Rad50} and C830^{Rad50} could be nicely visualized and does not evidently affect the ATPase domain of Rad50 (Figure 18C). Due to the extent of disulfide bridging or crystallization, the ATP used to engage NBDs for oxidative formation of the disulfide bonds was hydrolyzed to ADP (Figure 18D).

Surprisingly, the engaged NBD dimer is situated in the groove of the Mre11 dimer that harbors the nuclease active sites (Figure 18A). It contacts the phosphodiesterase domains and is encompassed by the two capping domains. The buried surface between Mre11 and Rad50 comprises a large area of 3052 Å². However, the new interfaces between capping and phosphodiesterase domains are quite polar and cover a rather small area each which indicates that these interfaces are presumably transient. The C-terminal HLH domain of Mre11 binds tightly across the base of Rad50^{NBD} coiled-coil domains, as seen already in the open form of Mre11:Rad50^{NBD}. This interface consists mostly of hydrophobic interactions and the preservation of this interaction suggests that this interface is unaltered during the conformational cycle and “anchors” Mre11 and Rad50 in a stable but flexible manner.

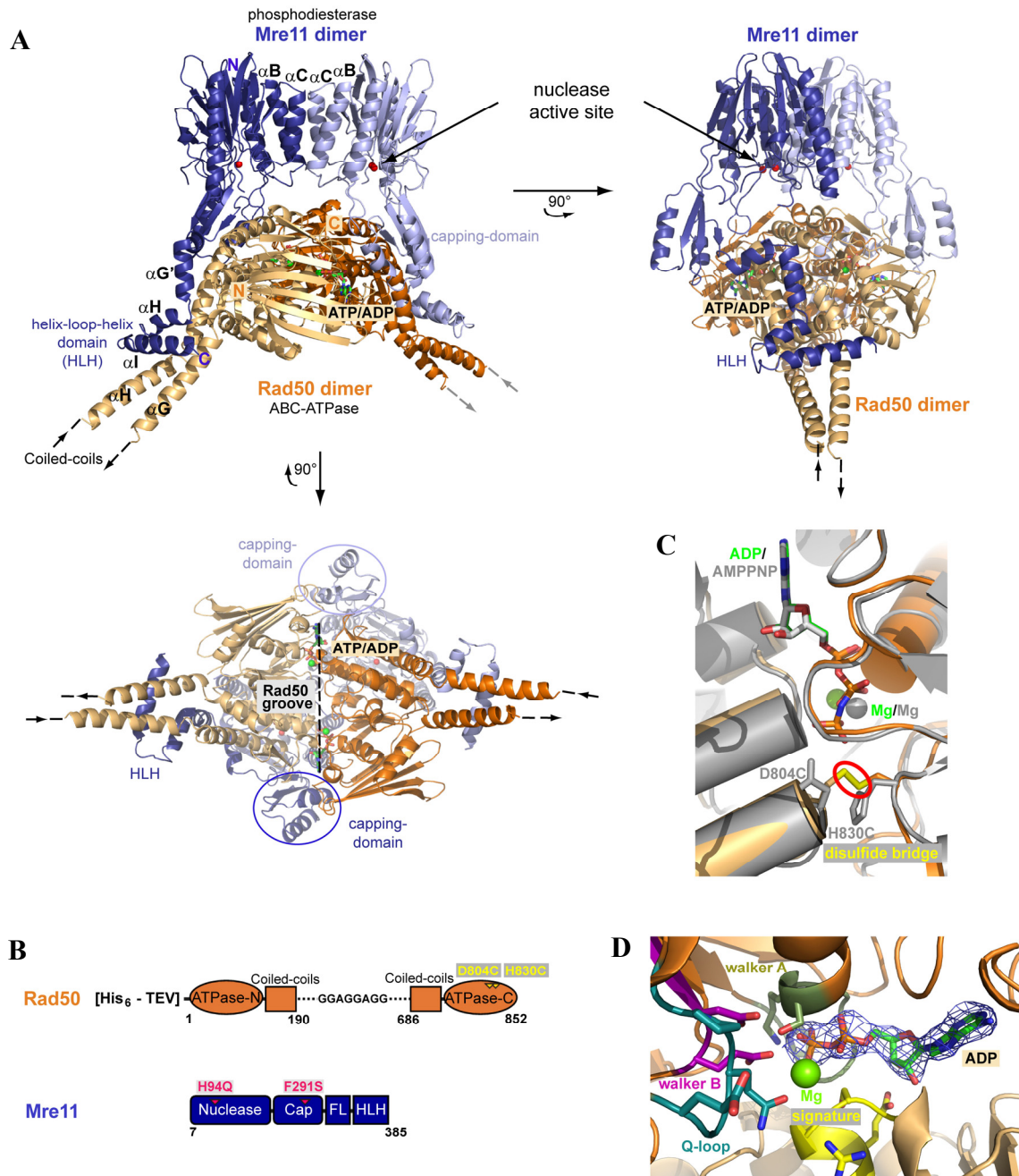


Figure 18: The *T. maritima* Mre11:Rad50^{NBD (S-S)} complex structure in ATP/ADP conformation (Möckel et al., 2011). (A) Ribbon representation of the Mre11:Rad50^{NBD (S-S)} heterotetrameric head module complex shown in three different orientations with Mre11 in blue and Rad50 in orange. Individual domains and important motifs are highlighted and annotated. (B) Construct design of Mre11:Rad50^{NBD} with Mre11 colored in blue Rad50 colored in orange. The yellow triangles signify the introduced cysteine mutations in Rad50^{NBD} (D804C, H830C), the purple triangles indicate the H94Q substitution in the nuclease domain of Mre11 and the interface 2 mutation (F291S). ATPase-N(C), N(C)-terminal ATPase domain; His₆, hexahistidine tag; Nuclease, phosphodiesterase domain; Cap, capping domain; FL, flexible linker; HLH, helix-loop-helix domain. (C) Superposition of the His-switch and D-loop region of the ATPase domain of Mre11:Rad50^{NBD (S-S)} (orange) and Mre11^{HLH}:Rad50^{NBD} (grey). The introduced cysteine residues with the formed disulfide bridge are colored in yellow. (D) Close up view of the ATP-binding site of Mre11:Rad50^{NBD (S-S)} with the initially obtained F₀-F_c map (contoured at 2.0 σ and colored blue) showing a clearly defined electron density for the ADP ligand.

The structural similarity of the resulting engaged NBD dimer to the AMPPNP bound dimers of isolated Rad50 NBDs from both *T. maritima* and *P. furiosus* confirms that the crosslinking traps an ATP like state (Figure 19).

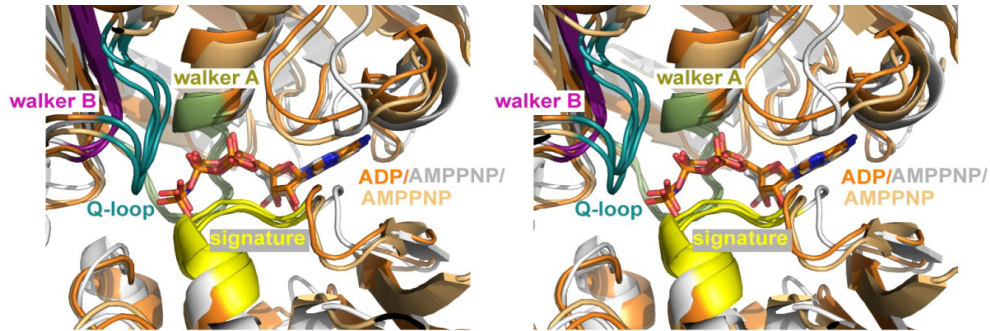


Figure 19: Structural similarity of Rad50 NBDs from bacterial *T. maritima* and archaeal *P. furiosus* (Möckel et al., 2011). Superposition of the ATP binding region of *T. maritima* Mre11:Rad50^{NBD (S-S)} bound to ADP (orange), the Rad50 ATPase domain of *P. furiosus* bound to AMPPNP (grey; PDB entry: 1F2U) and *T. maritima* Mre11^{HLH}:Rad50^{NBD} bound to AMPPNP (beige) presented in stereo view. Individual domains and important motifs are highlighted and annotated.

In summary, ATP engages both NBDs of Rad50 into a dimer that closely fits into the DNA binding/active site groove of the Mre11 dimer. This interaction suggests that ATP binding to Rad50 regulates MR by sterically controlling access to Mre11s nuclease and DNA binding sites.

4.3.3. ATP induced conformational changes of Mre11:Rad50^{NBD}

Comparing *T. maritima* Mre11:Rad50^{NBD} in the nucleotide free (PDB entry: 3QG5) and ATP/ADP bound state revealed a molecular framework for ATP induced conformational changes (Figure 20) (Möckel et al., 2011). The large conformational change within the whole complex induces a globular and compact shape upon ATP binding. The open to closed transition is driven by a large swivel movement of the NBDs, which move from the periphery of the MR catalytic head to its center. Rad50 loses the interaction with the outward facing side of the capping domain but gains a new interaction with the inward facing side. As a result, the angle between the coiled-coils is altered from 120° in the open complex to approx. 90° in the closed conformation. However, the coiled-

coils are almost inverted in their orientation relative to Mre11 and undergo an axial rotation with respect to each other.

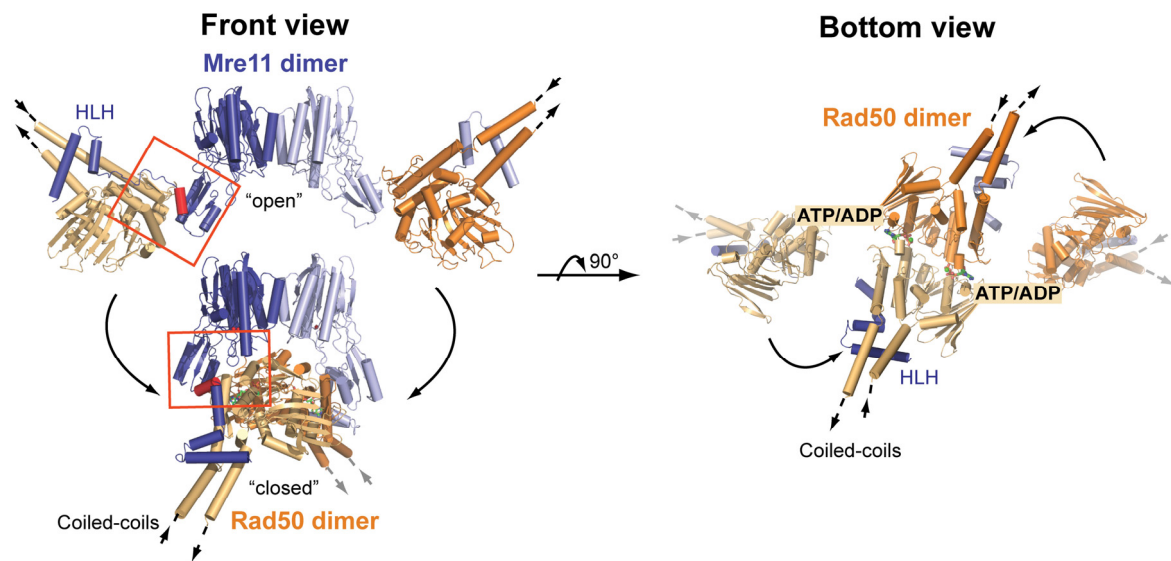


Figure 20: Impression of conformational changes of the *T. maritima* Mre11:Rad50^{NBD} complex upon nucleotide binding (Möckel et al., 2011). Comparison of the Mre11:Rad50^{NBD} complex structures in the open (PDB entry: 3QG5) and ATP bound conformation shown in front and bottom view orientation. The large conformational change within the whole complex induces a globular and compact shape upon ATP binding. Mre11 is colored in blue and Rad50 is colored in orange. Conformational changes in interface 2 are highlighted by red boxes and are correlated to Figure 21.

A detailed view of the conformational changes shows a slight compaction of the Mre11 dimer, driven by the 4 Å inward movement of the capping domains due to their interaction with the Rad50 NBDs and a slight alteration of the Mre11 dimer angle (Figure 21C and D; Figure 22C). Moderate movements of the cap domains in response to DNA binding have been seen by structural analyses of Mre11 in complex with DNA (Williams et al., 2008). At present, the functional role of these rather moderate conformational changes in Mre11 remains to be investigated.

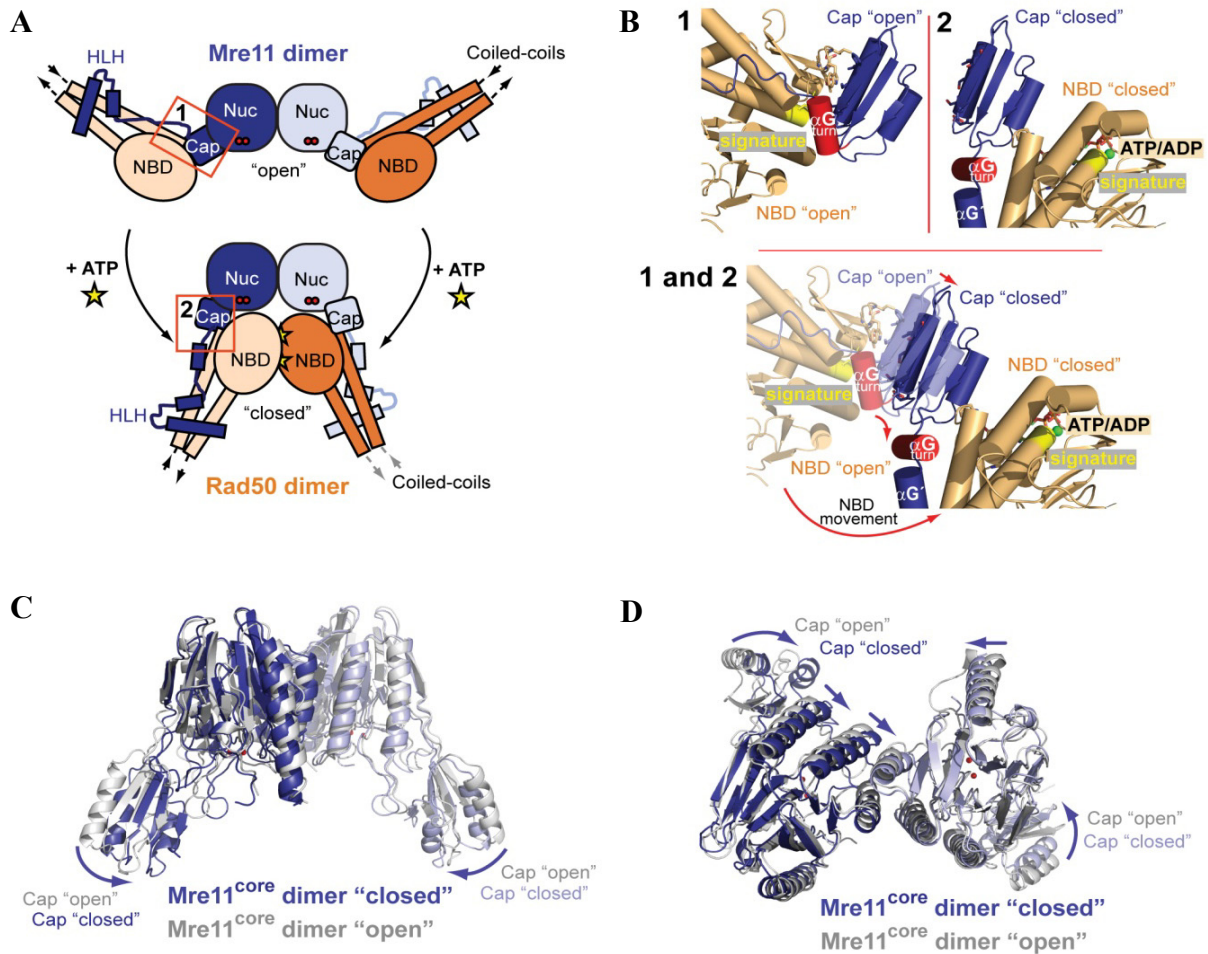


Figure 21: Detailed view of conformational changes of the *T. maritima* Mre11:Rad50^{NBD} complex upon nucleotide binding (Möckel et al., 2011). (A) Schematic representation of the overall domain movement within the complex upon ATP binding. Conformational changes in interface 2 are highlighted and correlated to Figure 20 and Figure 21B. (B) Close up view of the Mre11 capping domain and interface 2 in the open (1) and closed (2) Mre11:Rad50^{NBD} complex. The capping domains move inward by approx. 4 Å due to their interaction with the Rad50 NBDs and helix αG^{tum} rotates by roughly 90° from the open to the closed state. (C) and (D) Superposition of the Mre11 core domains of the nucleotide bound (blue) and unbound (grey) structures. The arrows indicate the rotation of the capping domain towards the nuclease active site upon Rad50 ATP binding. (D) The bottom view highlights the slight changes in the arrangement of the four-helix bundle between the open and closed conformation (straight arrows).

Altogether, the conformational changes can be viewed as a rigid body movement of three modules. One module represents the dimer of Mre11's phosphodiesterase and capping domain (Figure 21C and D). The two other modules are both Rad50 polypeptides together with the HLH domains of Mre11. On closer examination, there are also some notable changes on the secondary structure and subdomain level. The largest conformational rearrangement in this respect is observed in helix αG^{tum} that follows the

capping domain in the primary structure of Mre11 (Figure 20, Figure 21A and B). αG^{tum} rotates approx. 90° from the open to the closed state. This flexibility helps the relocation of the Rad50 molecules from the outward facing sides of the capping domains to the inward facing sides. In addition, the motif following αG undergoes a substantial structural rearrangement: in the open state, it is a flexible, rather unstructured linker connecting the HLH motif and αG^{tum} . Upon relocation of the NBD-HLH module, this region undergoes a disorder-to-order transition and forms $\alpha G'$. As a consequence, a right-angled, loose helix-loop-helix conformation forms at the lateral entry side of Mre11's blocked DNA binding cleft. It may act as a kind of spring to facilitate and allow conformational changes between the flexible modules, but is also positioned to perhaps function in DNA binding (see below).

4.3.4. Anchoring and transient interfaces of Mre11:Rad50^{NBD}

The two observed conformational states (nucleotide free and nucleotide bound form) of *T. maritima* Mre11:Rad50^{NBD} are stabilized by three types of macromolecular interfaces (Figure 22A) (Möckel et al., 2011). The two “anchor” interfaces between the HLH:coiled-coil (interface 1) (Figure 22B) and phosphodiesterase:phosphodiesterase (Mre11 homodimer interface) (Figure 22C) preserve the Mre11₂:Rad50₂ heterotetramer during the conformational cycle and are maintained in the open and closed states. Finally, a third transient interface between the capping domain and NBD and phosphodiesterase and NBD (interface 2) specifically orients Rad50 to Mre11 in the open and closed states (Figure 22D).

The Mre11 dimer interface is a four-helix bundle composed of αB and αC of the two Mre11 phosphodiesterase domains as already described for the nucleotide free form of *T. maritima* Mre11:Rad50^{NBD} (Bemeleit, 2007; Lammens et al., 2011). Comparison of the open Mre11:Rad50^{NBD} and closed Mre11:Rad50^{NBD (S-S)}} dimer interfaces shows a slight change in the arrangement of the four-helix bundle (Figure 22C). The second “anchor” interface between the HLH domain of Mre11 and the coiled-coil of Rad50 (interface 1) is largely unaltered between open and closed states (Figure 22B). This interface is composed of mainly aromatic and hydrophobic residues and is thoroughly described in section 4.1.3, crystal structure of Mre11^{HLH}:Rad50^{NBD} bound to AMPPNP. The hydrophobic pattern in interface 1 is highly conserved in all known homologues (see section 4.1.3) (Figure 10B).

However, it is interesting to note that despite the motif's functional conservation, an additional third Mre11 helix interacts with the Rad50 coiled-coil in archaea (Figure 23A and B) (Lim et al., 2011; Williams et al., 2011).

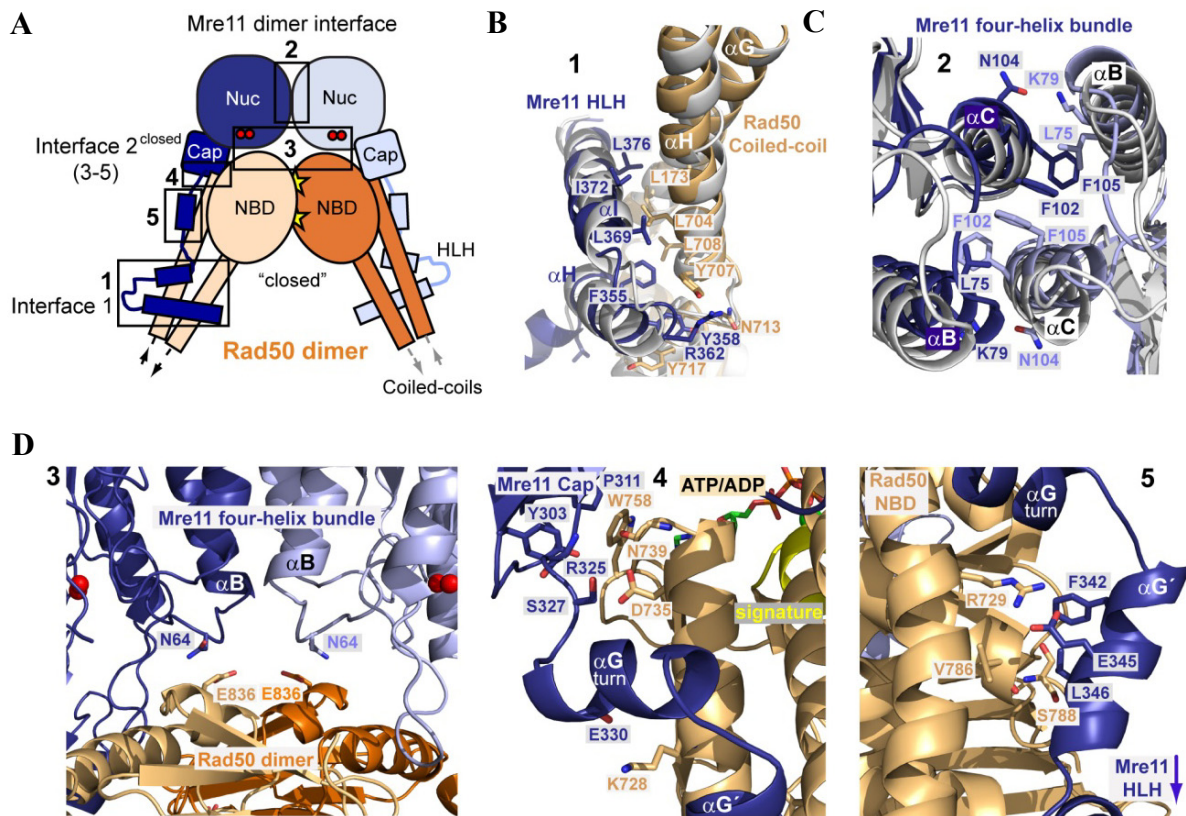


Figure 22: Details of the *T. maritima* Mre11:Rad50^{NBD (S-S)} interfaces (Möckel et al., 2011). (A) Denotation of interfaces. Mre11 is colored in blue, Rad50 is colored in orange. The three types of macromolecular interfaces are highlighted by black boxes. (B) Superposition of interface 1 of the open and closed Mre11:Rad50^{NBD} complex in ribbon representation indicate that the interactions remain unchanged (closed complex is colored according to Figure 22A and the open complex is shown in grey, PDB entry: 3QG5). (C) Superposition of the Mre11 homodimer interface shows slight changes in the arrangement of the four-helix bundle between the open and closed complex. (D) Details of the altered and newly formed interface 2 of the ATP bound Mre11:Rad50^{NBD (S-S)} complex (3-5). Selected side chains are shown as color coded sticks and are annotated.

Large changes in response to ATP binding are seen in interface 2. The interface between the NBDs and the outward facing side of the capping domain (interface 2^{open}) is disrupted and several new interaction sites are formed (interface 2^{closed}) (Figure 22D). Adjacent to the Mre11 four-helix bundle homodimer interface, ($\alpha^{\text{B Mre11}}$) residue N64^{Mre11} contacts E836^{Rad50}, a highly conserved residue in Rad50 (Figure 22D-3). An additional

arginine R832^{Rad50}, disordered in our structure, could provide additional interactions with N64^{Mre11}.

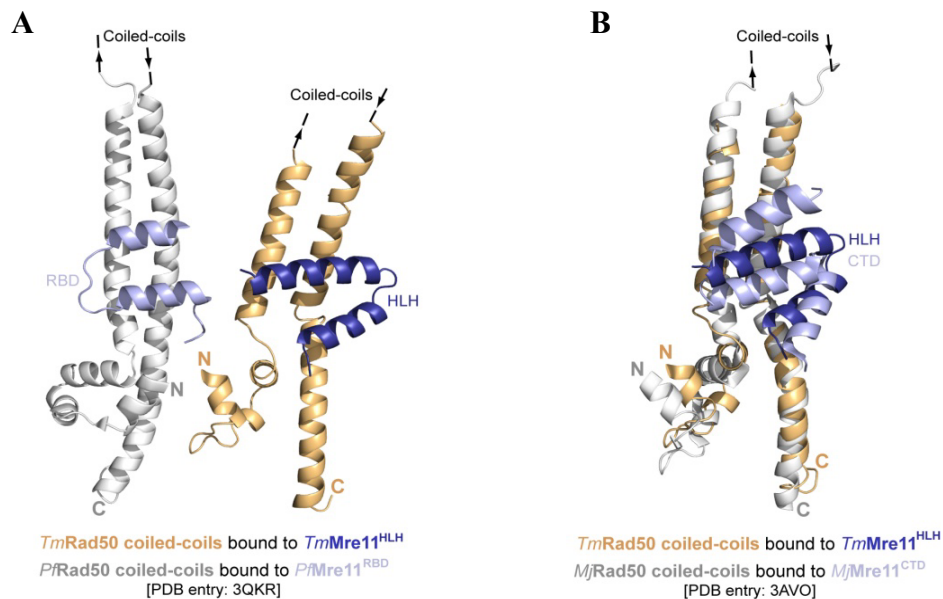


Figure 23: Structural differences observed in interface 1 between bacteria and archaea (Möckel et al., 2011). (A) Comparison of the Rad50 coiled-coil domain bound to Mre11^{HLH} (HLH domain also denoted as RBD in *P. furiosus* and CTD in *M. jannaschii*) of the bacterial *T. maritima* (beige/dark blue) and the archaeal *P. furiosus* (grey/light blue). (B) Superposition of the respective domains of *T. maritima* (color coded according to Figure 23A) and the archaeal *M. jannaschii* (grey/light blue). (A) and (B) Despite the conservation of the helix-loop-helix motif between bacterial and archaeal Mre11, *M. jannaschii* and *P. furiosus* contain a third helix which interacts additionally with the Rad50 coiled-coils.

The capping domains of Mre11 interact with regions in close proximity to the ATP binding site in Rad50 (Figure 22D-4). Residue W758^{Rad50}, situated near the base of a coiled-coil helix, forms a small hydrophobic interface with the inward facing side of the capping domain, flanked by several hydrogen bonds. This residue also stabilizes the interaction of the NBDs with the outward facing site of the capping domain β -sheet.

Additionally some interactions are generated between Rad50 and the newly formed helix $\alpha G'$, in the course of the disorder-to-order transition (Figure 22D-5).

4.3.5. Analysis of Mre11:Rad50^{NBD (S-S)} in solution via small angle x-ray scattering

To confirm the proposed molecular framework for ATP induced conformational changes the structure of *T. maritima* Mre11:Rad50^{NBD (S-S)} in its ATP/ADP bound state was analyzed by comparing the theoretical calculated scattering curves to the experimental SAXS data described in 4.2.3 (Figure 24).

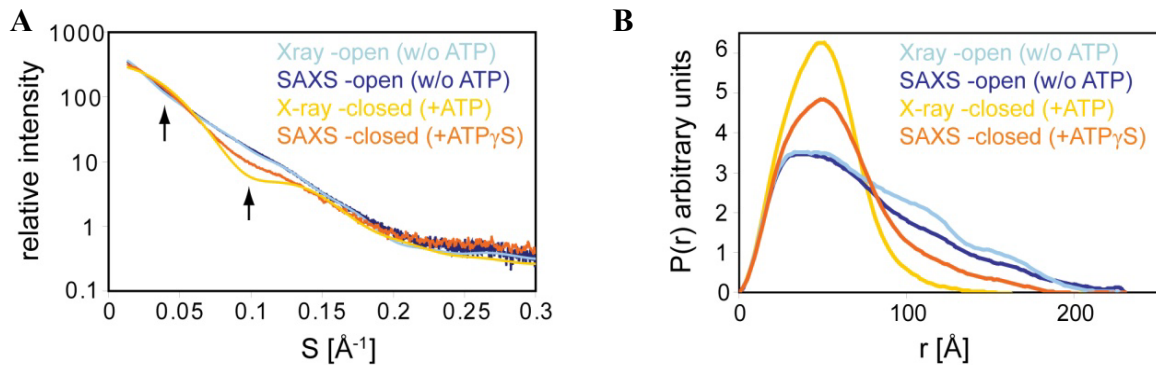


Figure 24: Conformational change between the open and closed *T. maritima* Mre11:Rad50^{NBD} complex. (A) Superposition of experimental and calculated SAXS curves for the open (blue) and closed (orange/yellow) Mre11:Rad50^{NBD} complex. Both conformations exist in solution as indicated by the corresponding experimental and calculated SAXS curves. (B) The electron pair distance distribution function $P(r)$ of the closed and open state corresponds to the respective crystal structure derived $P(r)$ distribution. The structure derived $P(r)$ distribution indicates an increase of short distances and a decrease in long distances. In contrast to the ATP γ S induced Rad50^{NBD} engagement residual long distances which assumed a heterogeneous mixture between the open and closed conformation are not apparent anymore.

Both scattering intensities and $P(r)$ distribution of Mre11:Rad50^{NBD} in the presence of ATP γ S show characteristic features (e.g. shape of curve and radius of maximum in $P(r)$) that are qualitatively but not quantitatively preserved in the scattering intensities and the corresponding $P(r)$ distribution from the crystal structure of the trapped ATP/ADP state (Figure 24A and B). The experimental scattering curves can be interpreted as linear combination of the scattering curves from the two open and closed state crystal structures (Figure 24A). This emphasizes the assumption that Mre11:Rad50 exists in equilibrium between two populated states (open and closed), with ATP shifting the equilibrium towards the closed state. The latter state is also indicated with regards to the $P(r)$ distribution function. Both the structure derived curve and the experimental $P(r)$ distribution function in the presence of ATP γ S illustrate an increase of short distances and

a decrease of long distances compared to the nucleotide free complex (Figure 24B). However, as seen for the ATP γ S induced Rad50^{NBD} engagement the residual long distances indicates a heterogeneous mixture between the open and closed states which are dramatically reduced for the structure based P(r) distribution, stating once more the molecular framework for ATP induced conformational changes.

To validate once more whether the closed, ring-shaped conformation is the biological assembly present in solution, SAXS experiments were performed with the disulfide bridged Mre11:Rad50^{NBD (S-S)} complex. The measurements were performed using three different protein concentrations between 1 and 10 mg/ml. Based on the assumption that both the open and closed form exists in solution and the fact that roughly 65% of the Mre11:Rad50^{NBD} can be efficiently crosslinked by disulfide bond formation, 35% of the open form was subtracted from the experimental Mre11:Rad50^{NBD (S-S)} scattering curve. *Ab initio* shape reconstructions were calculated with a two-fold symmetry by the program DAMMIN (Svergun, 1999). The determined molecular envelope fits nicely to the corresponding structure of Mre11:Rad50^{NBD (S-S)} in its ATP/ADP bound state, confirming the biological assembly in solution, although the envelope is slightly bigger than the crystal structure itself (Figure 25). This is probably due to the conformation of the coiled-coil domains of Rad50 which are likely stabilized in the crystal but might be flexible in solution.

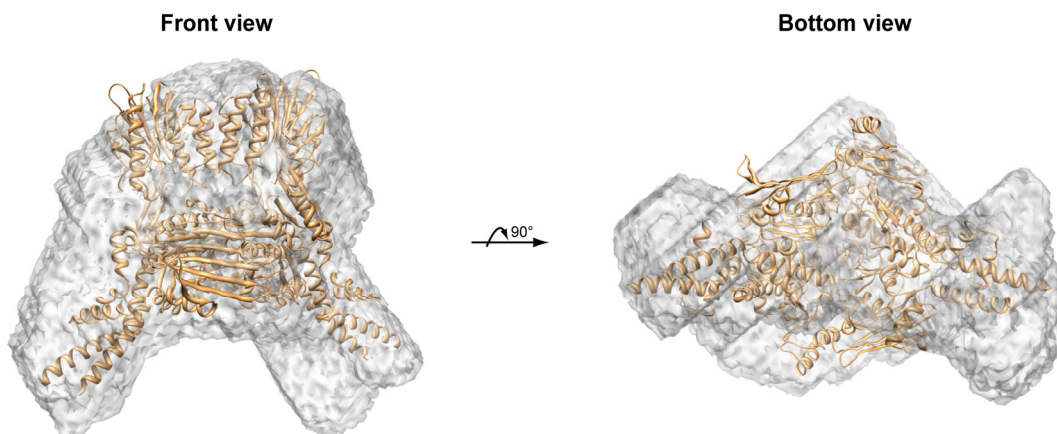


Figure 25: Solution scattering analysis and model reconstruction of *T. maritima* Mre11:Rad50^{NBD (S-S)}. Three dimensional envelopes were calculated with a two-fold axis from a theoretical SAXS curve where 35% of the open form was subtracted from the experimentally obtained Mre11:Rad50^{NBD (S-S)} scattering curve. The *ab initio* model was illustrated with the program UCSF CHIMERA (Pettersen et al., 2004) and superimposed with the crystal structure of the Mre11:Rad50^{NBD (S-S)} complex in its ATP/ADP bound state.

4.4. Analysis of the DNA binding mechanism of *T. maritima* Mre11:Rad50

4.4.1. DNA affinity of the Mre11:Rad50^{NBD} complex in the open and closed state

To test whether ATP binding leads to a structure with increased DNA affinity, the DNA binding capability of *T. maritima* Mre11:Rad50^{NBD} was analyzed in the nucleotide free and bound conformation by Electrophoretic Mobility Shift Assays (EMSAs).

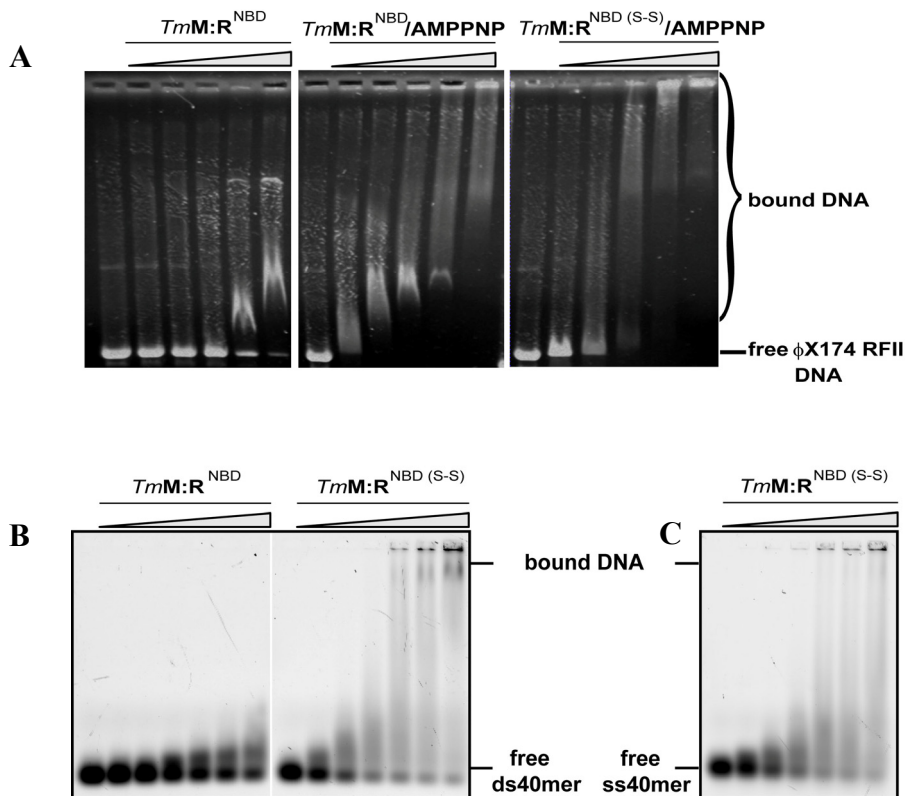


Figure 26: DNA affinity of *T. maritima* Mre11:Rad50^{NBD} in open and closed states. (A) DNA affinity to double stranded Φ X174 RF II plasmid DNA of the Mre11:Rad50^{NBD} complex w/o AMPPNP compared to the disulfide bridged Mre11:Rad50^{NBD (S-S)} complex tested by Electrophoretic Mobility Shift Assay (EMSA). The EMSA indicates that the closed, ATP bound complex resembles the DNA binding conformation. Following protein (0, 0.25, 0.50, 1.0, 2.0 and 3.0 mg/ml respectively) and Φ X174 RF II plasmid DNA (0.5 μ g) concentrations were used. (B) Electrophoretic Mobility Shift Assay shows that the disulfide bonded Mre11:Rad50^{NBD (S-S)} complex has strongly increased affinity to double stranded DNA oligonucleotides compared to the open, nucleotide free complex. (C) Electrophoretic Mobility Shift Assay shows that the disulfide bonded Mre11:Rad50^{NBD (S-S)} complex binds likewise to single and double stranded DNA. (B) and (C) Following protein concentrations (0, 1.0, 2.5, 5.0, 7.5, 10.0 and 15.0 μ M respectively) were analyzed. 100 nM of 6-FAM 5'-labeled double stranded and single stranded DNA (40mer) was used, respectively.

Indeed, the addition of the ATP analog AMPPNP showed a strong effect on binding of Mre11:Rad50^{NBD} to double stranded plasmid DNA (Φ X174 RF II) (Figure 26A). Interestingly, the disulfide bridged Mre11:Rad50^{NBD (S-S)} complex had even higher affinity to double stranded DNA (Figure 26A and B). This could be due to the fact that during the process of disulfide bridging approx. 65% of the complex gets trapped in the closed state whereas in the presence of ATP or analogs a rather small fraction comprises engaged NBDs as validated by SAXS experiments (see section 4.3.5).

The disulfide bridged Mre11:Rad50^{NBD (S-S)} complex binds both double and single stranded DNA with increased affinity (Figure 26C). Although several DNA structures like hairpins, forks and DNA's with various overhangs were analyzed, no obvious preference to certain secondary structures could be found.

Anyway, since Mre11:Rad50^{NBD (S-S)} binds with the same affinity to DNA regardless if AMPPNP is present or not, these data suggests that the engaged, clamp like form presents the DNA binding conformation.

4.4.2. DNA affinity of the single MR components

To see if and how the single components of *T. maritima*, namely Mre11 and Rad50^{NBD}, or the entire Mre11:Rad50^{NBD} may interact with DNA, Mre11^{HLH}:Rad50^{NBD}, lacking the Mre11 “core” domain residues M7-342, in comparison to the whole disulfide bridged Mre11:Rad50^{NBD (S-S)} complex was analyzed (Figure 27A-C) (Möckel et al., 2011). Prior to analysis, Mre11^{HLH}:Rad50^{NBD} was incubated with the nonhydrolysable ATP analog AMPPNP for 3 days at 4°C to allow formation of engaged NBD:NBD dimers (following denoted as Mre11^{HLH}:Rad50^{NBD (Dimer)}). Subsequent assessment of the dimeric state was achieved by analytical gel filtration. Even though the dimer fraction was varying, a minimum level of 75% of Mre11^{HLH}:Rad50^{NBD (Dimer)} was reached (Figure 27C). Although Mre11^{HLH}:Rad50^{NBD (Dimer)} lacks the phosphodiesterase as well as the capping domains of Mre11, previously identified as important dsDNA binding elements (Williams et al., 2008), it binds plasmid dsDNA (Φ X174 RF II) with an affinity that is comparable to that of Mre11:Rad50^{NBD (S-S)}, apart from minor differences in the yield of disulfide bridged protein and dimerization efficiency. DNA binding of the Mre11^{HLH}:Rad50^{NBD} monomer in the absence of ATP could not be detected as expected (Figure 27A). Thus, the ATP

induced high affinity dsDNA binding site of Mre11:Rad50 is located in the NBD-HLH module and requires dimerization of this, either by binding of AMPPNP or by disulfide mediated crosslinking of the ATP bound form followed by ATP hydrolysis to ADP.

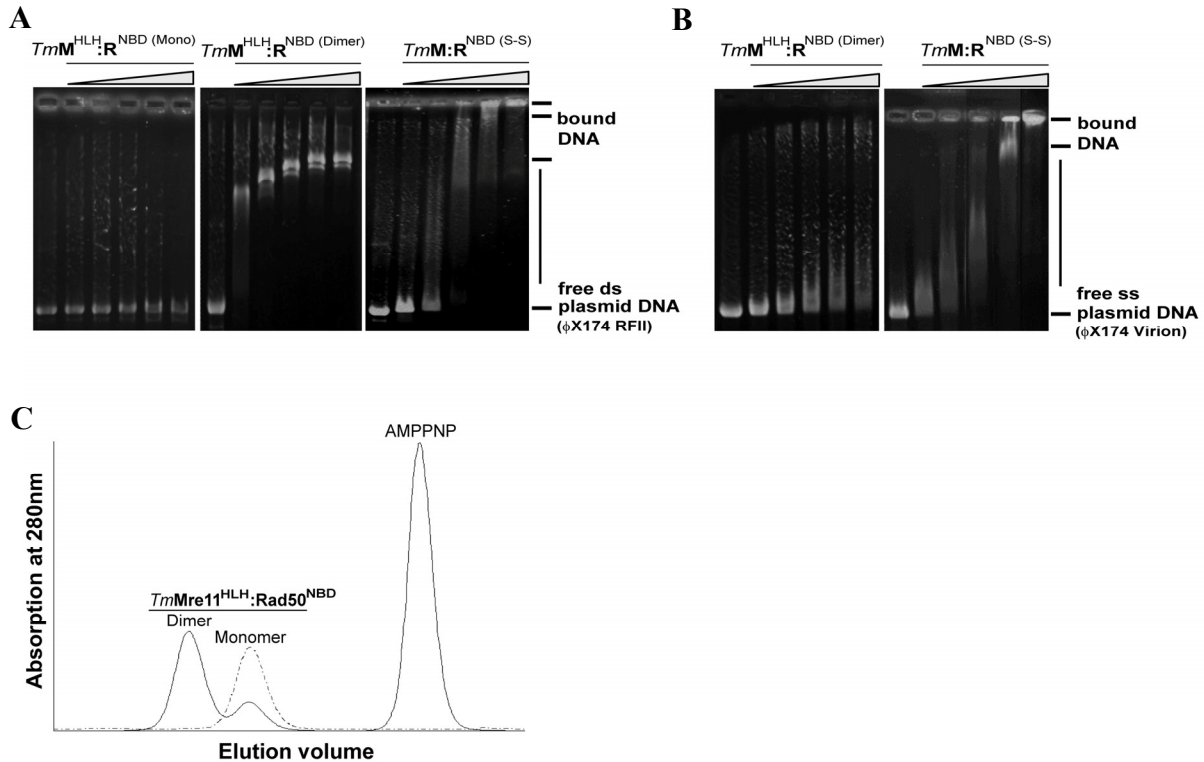


Figure 27: Comparison of the DNA affinity of *T. maritima* Mre11^{HLH}:Rad50^{NBD} and Mre11:Rad50^{NBD} (S-S) using Electrophoretic Mobility Shift Assay (Möckel et al., 2011). (A) While the monomeric Mre11^{HLH}:Rad50^{NBD} protein shows no affinity to double stranded plasmid DNA (ΦX174 RF II), comparable DNA affinities of Mre11^{HLH}:Rad50^{NBD} (Dimer) (lacks Mre11 catalytic core) and the heterotetrameric Mre11:Rad50^{NBD} (S-S) complex could be observed. Following protein (0.125, 0.25, 0.5, 1.0 and 1.5 mg/ml respectively) and ΦX174 RF II plasmid DNA (0.5 μg) concentrations were used. (B) Comparison of the affinity to single stranded DNA (ΦX174 Virion) revealed a weak interaction between Mre11^{HLH}:Rad50^{NBD} (Dimer) and DNA whereas Mre11:Rad50^{NBD} (S-S) showed no difference in binding compared to double stranded plasmid DNA. Analyzed protein (0, 0.25, 0.50, 1.0, 2.0 and 3.0 mg/ml respectively) and ΦX174 Virion plasmid DNA (1.0 μg) concentrations. (C) Gel filtration chromatogram of Mre11^{HLH}:Rad50^{NBD} in the presence (solid line) or absence (dashed line) of AMPPNP using a Superdex 200 5/150 GL gel filtration column. Incubation of monomeric protein with AMPPNP lead to approx. 75% dimerized protein.

In contrast to dsDNA binding, Mre11^{HLH}:Rad50^{NBD} (Dimer) showed almost no affinity for single stranded plasmid DNA (ΦX174 Virion). Thus, the binding site on this module is highly specific to dsDNA. However, the disulfide bridged closed complex not only binds dsDNA with high affinity, but also efficiently bound the ssDNA plasmid (Figure 27B). Thus, the presence of Mre11 nuclease and capping domains created an

additional ssDNA binding site in the complex. Alternatively, short hairpins could form on Φ X174 ssDNA which might be recognized by Mre11:Rad50^{NBD (S-S)} but not by the dsDNA binding site of Mre11^{HLH}:Rad50^{NBD (Dimer)}. It is therefore conceivable that in the ATP bound closed state the NBD-HLH module dimer is responsible for binding to dsDNA while Mre11 nuclease and capping domains might still bind ssDNA but are blocked from binding dsDNA.

4.4.3. Analyzing the molecular clamp mechanism of Mre11:Rad50^{NBD}

A major result of the structural analysis of *T. maritima* Mre11:Rad50^{NBD} is that Rad50 blocks Mre11's DNA binding sites in the ATP bound form (see section 4.3.2). However the possibility remains that, although the crystal structures of the open and closed complex explain the solution SAXS data (see sections 4.2.3 and 4.3.5), DNA induces an additional conformational change enabling it to bind to both Mre11 nuclease and capping domains and NBD-HLH module. For instance, a relatively moderate structural change could lead to double stranded DNA being sandwiched between Rad50 NBDs and the phosphodiesterase domains of Mre11.

To test this possibility, Mre11:Rad50^{NBD} was disulfide bridged in the presence of single and double stranded DNA (Φ X174 Virion and Φ X174 RF II) under conditions where in EMSA most of the DNA is shifted by bound protein (Figure 28A-F). In both cases subsequent gel filtration failed to detect co-elution of DNA and protein. The fact that Mre11:Rad50^{NBD} could not be crosslinked around internal DNA leads to the assumption that the complex does not bind the DNA by encircling it in a ring-like structure.

To confirm this statement DNA binding of *T. maritima* Mre11:Rad50^{NBD (S-S)} was additionally investigated via EMSA and gel filtration with double stranded DNA oligos containing a 5' fluorescein label (Möckel et al., 2011). A single-chain Fv fragment (scFv) of a fluorescein binding antibody can be used to block the DNA ends (Honegger et al., 2005) (Figure 29). To analyze if the disulfide bridged, trapped ATP bound form can still bind dsDNA with both ends blocked by the scFv fragment FITC-E2 (Figure 29A) DNA affinity of Mre11:Rad50^{NBD (S-S)} was tested by adding the complex to the dsDNA with blocked ends and subsequent EMSA (Figure 29B). To exclude incomplete end blocking of the DNA, the interaction between antibody and fluorescein labeled DNA was validated by

analytical gel filtration (Figure 29C). Nevertheless the disulfide bridged, ATP bound complex was still able to bind DNA with blocked ends. Thus, double stranded DNA is likely not to be encircled by Mre11:Rad50.

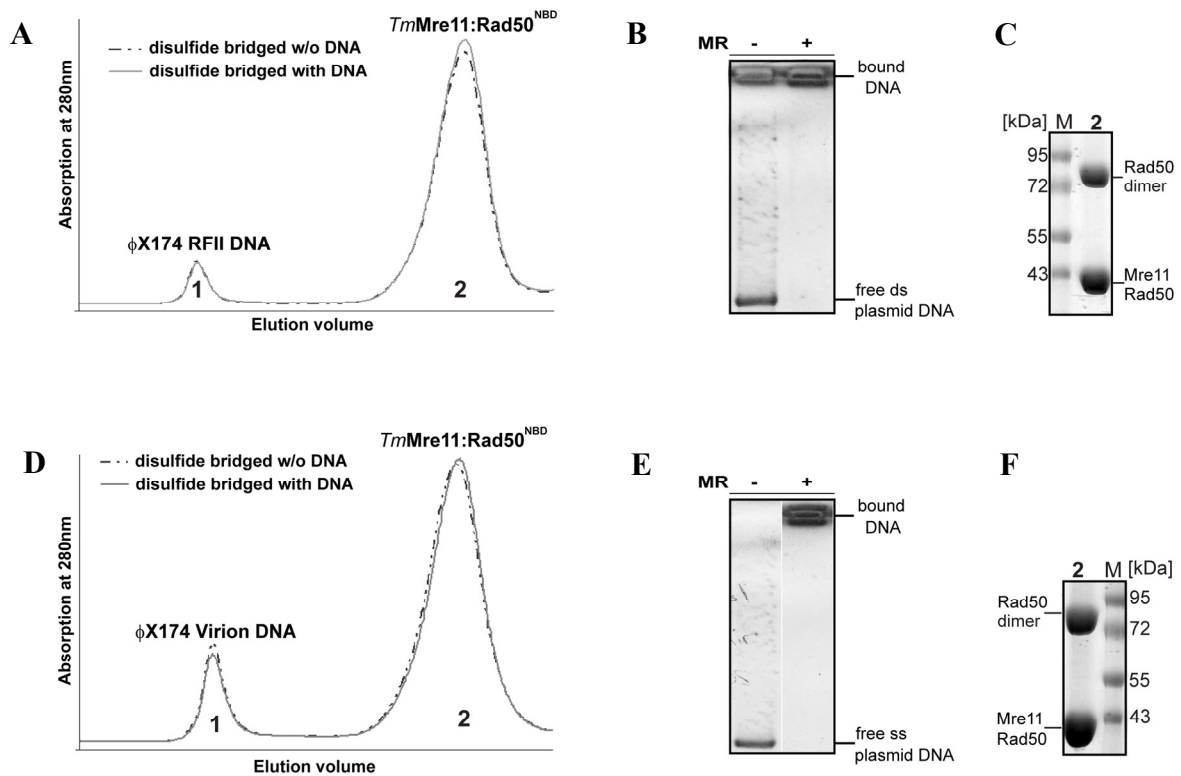


Figure 28: Biochemical analysis of the molecular clamp mechanism of *T. maritima* Mre11:Rad50^{NBD}. (A) Gel filtration chromatogram of the disulfide bridged Mre11:Rad50^{NBD} complex in the presence of ATP and double stranded ϕX174 RF II plasmid DNA was carried out onto a Superose 6 PC 3.2/30 gel filtration column. Disulfide bridging of the complex was carried out either in the presence (solid line) or absence (dashed line) of DNA, prior to gel filtration. The disulfide bridged Mre11:Rad50^{NBD} did not co-elute with the plasmid DNA fraction (peak 1), indicating that the complex cannot form a stable ring around internal DNA. (B) Electrophoretic Mobility Shift Assay (EMSA) shows that the ϕX174 RF II plasmid DNA was completely bound by the Mre11:Rad50^{NBD} complex used in the above described gel filtration chromatography experiment. (C) SDS PAGE presenting the disulfide bridged Mre11:Rad50^{NBD} complex from peak 2 of the gel filtration chromatogram in (A). (D) Gel filtration chromatogram of the disulfide bridged Mre11:Rad50^{NBD} complex in the presence of ATP and single stranded ϕX174 Virion plasmid DNA was carried out onto a Superose 6 PC 3.2/30 gel filtration column. Disulfide bridging of the complex was carried out either in the presence (solid line) or absence (dashed line) of DNA, prior to gel filtration. The disulfide bridged Mre11:Rad50^{NBD} did not co-elute with the plasmid DNA fraction (peak 1), indicating that the complex cannot form a stable ring around internal DNA. (E) EMSA shows that the ϕX174 Virion plasmid DNA was completely bound by the Mre11:Rad50^{NBD} complex used in the above described gel filtration chromatography experiment. (F) SDS PAGE presenting the disulfide bridged Mre11:Rad50^{NBD} complex from peak 2 of the gel filtration chromatogram in (D).

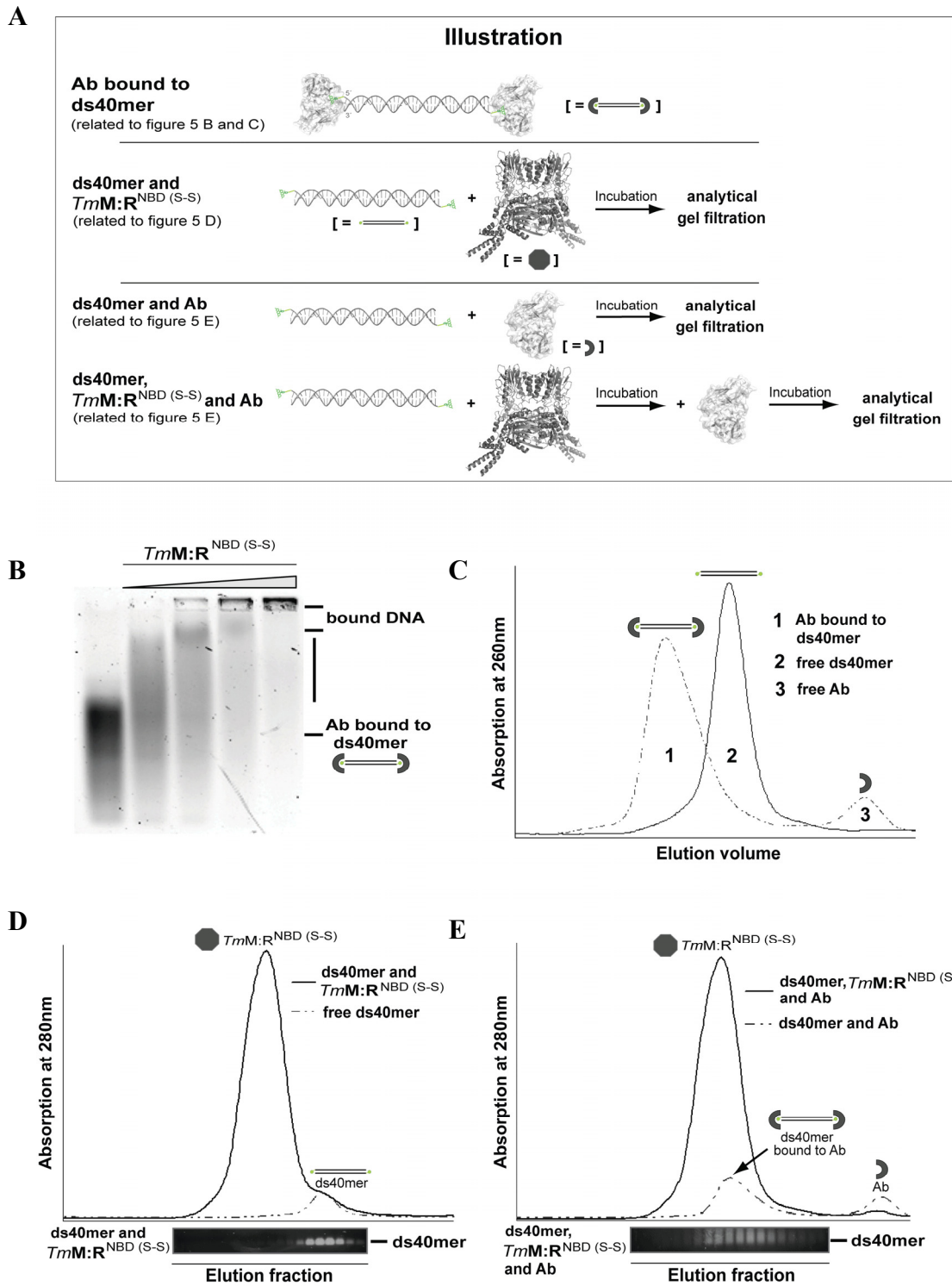


Figure 29: Details of the DNA binding mechanism of *T. maritima* Mre11:Rad50^{NBD (S-S)} via the Antibody DNA Binding Assay (Möckel et al., 2011). (A) Illustration of the Antibody DNA Binding Assay described in Figure 29B–E. (B) Electrophoretic Mobility Shift Assay showing that the nucleotide bound, closed Mre11:Rad50^{NBD (S-S)} complex can still bind to antibody blocked double stranded 40mer DNA. Following protein concentrations were used: 0, 1.75, 3.50, 7.0 and 14.0 μ M. (C) Gel filtration chromatogram of 5' fluorescein labeled ds40mer in the absence (solid line) and presence (dashed line) of the antibody fragment FITC-E2 verified complete blocking of the respective double stranded DNA. The presence of antibody scFV shifted the DNA to larger molecular weights (peak 1) compared to DNA alone (peak 2) and

free scFv (peak 3). **(D)** Gel filtration chromatogram of the 5' fluorescein labeled ds40mer in presence (solid line) and absence (dashed line) of Mre11:Rad50^{NBD (S-S)}. Prior to gel filtration protein and DNA were incubated under conditions where in EMSA most of the DNA is shifted by bound protein. The gel filtration retention volumes were subsequently analyzed by agarose gel electrophoresis. The agarose gel lanes are aligned with the respective fractions of the gel filtration elution. **(E)** Gel filtration chromatogram of the DNA-antibody mixture (dashed line) and the ternary DNA-(Mre11:Rad50^{NBD (S-S)})-antibody complex (solid line). Analysis of the respective elution fractions by agarose gel electrophoresis indicates that the complex could not be trapped on double stranded DNA. All gel filtration experiments were carried out using a S200 5/150 GL column.

To further validate this model, fluorescein labeled dsDNA was first incubated with Mre11:Rad50^{NBD (S-S)}, followed by blocking of the 5' ends by scFv. Subsequently the DNA:protein complex was analyzed by analytical gel filtration and agarose gel electrophoresis (Figure 29D-E). Since the gel filtration retention volume of DNA bound to scFv and/or Mre11:Rad50^{NBD (S-S)} would be shifted in comparison to that of free DNA, it should be possible to detect encircling of MR^{NBD (S-S)} around DNA. However, we did not see any change in retention volume or evidence for a ternary DNA:(Mre11:Rad50^{NBD (S-S)}):antibody complex. Therefore it is unlikely that Mre11:Rad50^{NBD} forms a ring around dsDNA (Figure 29B-E).

4.4.4. Examination of DNA binding via surface analysis of Mre11:Rad50^{NBD}

Beside the biochemical analysis of the DNA binding mechanism of *T. maritima* Mre11:Rad50^{NBD}, the complex was additionally investigated by surface analysis and by comparing the complex with already existing structures where Mre11 is bound to DNA (Williams et al.). Superposition of the nucleotide bound closed *Tm*Mre11:Rad50^{NBD (S-S)} complex with the *P. furiosus* (*Pf*)Mre11 bound to either synaptic or branched DNA (PDB entry: 3DSC and 3DSD respectively) on the Mre11 dimer indicates, that in both cases the dsDNA would interfere with the NBD:NBD domain of *Tm*Rad50. *Pf*Mre11 is not shown for clarity in both illustrations. This matches the biochemical observations that Mre11:Rad50^{NBD} does not bind to DNA by encircling and indicates that the Rad50 dimer needs to harbor an additional dsDNA binding site.

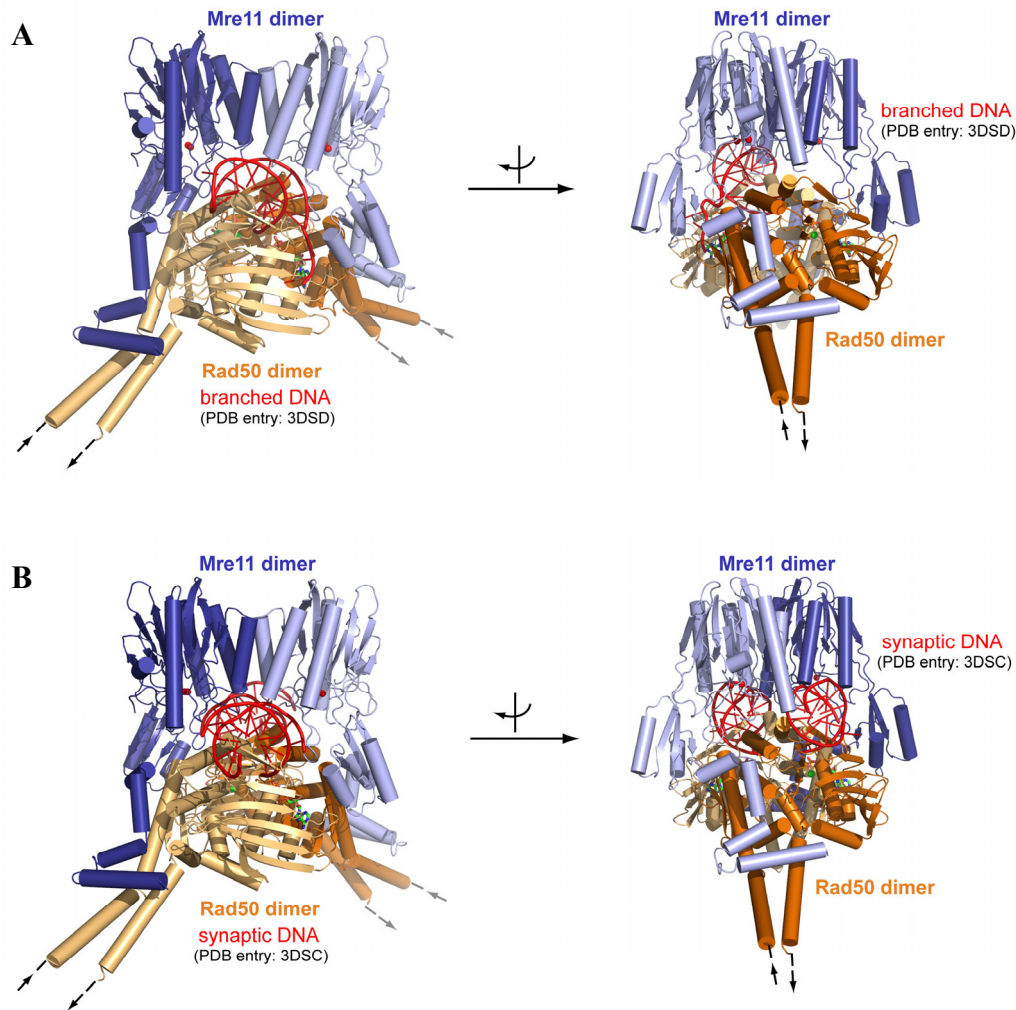


Figure 30: Consideration of Mre11's double stranded DNA binding site in the nucleotide bound closed Mre11:Rad50^{NBD (S-S)} complex. (A) and (B) Superposition of the closed *Tm*Mre11:Rad50^{NBD (S-S)} complex (Mre11 blue and Rad50 orange) and the *Pf*Mre11 dimer bound to synaptic and branched DNA (PDB entry: 3DSC and 3DSD respectively; DNA colored in red). In both instances the Mre11 bound DNA would interfere with the Rad50 domain of the tetrameric, ATP bound complex.

Although the exact nature of the interaction of Mre11:Rad50 with DNA remains to be determined experimentally, some clues can be observed from the analysis of the molecular and the electrostatic surface potential. A positive patch, complementary in size and charge to double stranded DNA backbones, is observed at the surface between the protruding coiled-coil elements (Figure 31A). Alternatively, positively charged surface patches are located on the lateral side of Rad50. These patches may potentially bind dsDNA but in both cases the DNA is rather far away from the cleft between Mre11 and

Rad50, making it at present unclear how DNA binding and DNA processing are functionally coupled.

Alternatively, ATP dependent engagement of the NBDs could unwind dsDNA ends with one of the ssDNA strands binding between Rad50 and Mre11. While Rad50 blocks the dsDNA binding site, there are solvent accessible voids between Rad50 and Mre11 that reach the Mre11 active site and are large enough to accommodate ssDNA (Figure 31B). Thus, at least from a structural point of view, it is conceivable that the closed state can cleave ssDNA either endo- or exonucleolytically.

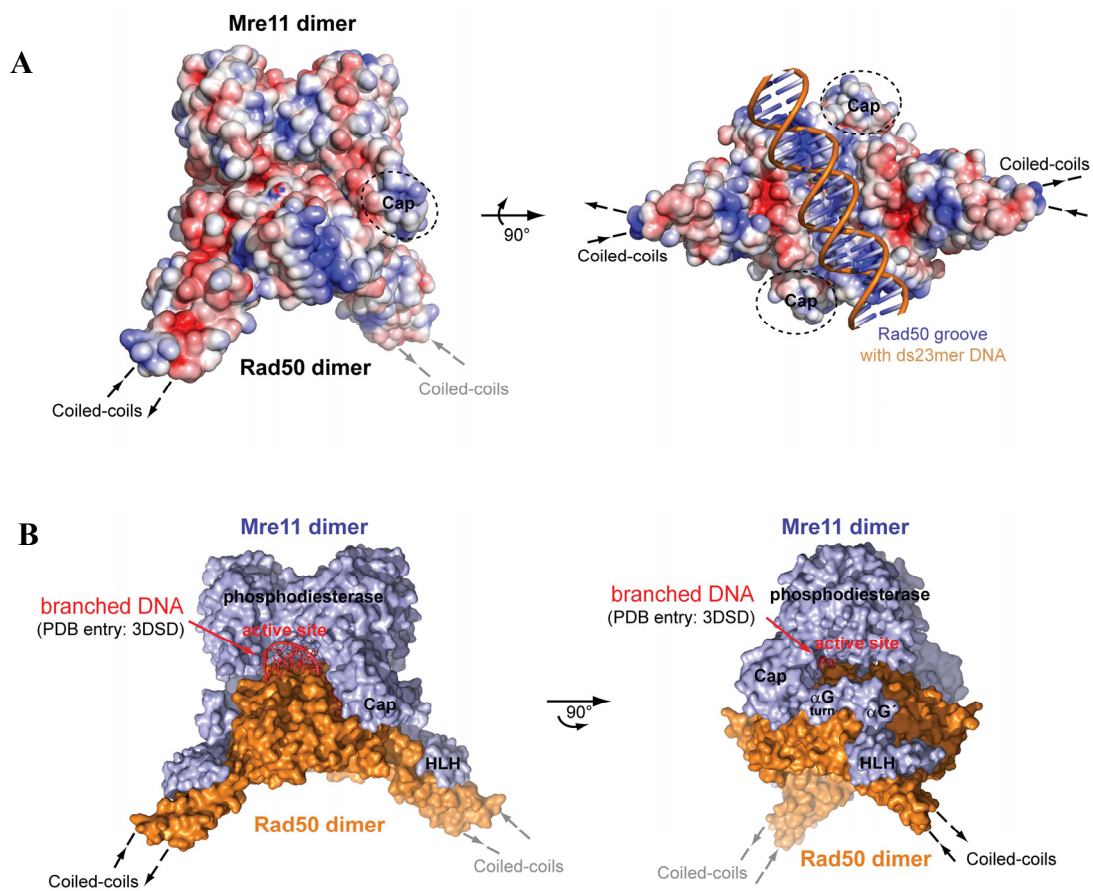


Figure 31: Surface analysis of *T. maritima* Mre11:Rad50^{NBD (S-S)}. (A) Electrostatic surface potential of *T. maritima* Mre11:Rad50^{NBD (S-S)} in front and bottom view orientation was calculated using APBS tools (Baker, 2004) and indicates positively (blue) charged patches located on the lateral side of Rad50 and along the Rad50 groove. Latter one is suitable in size and charge complementary to dsDNA backbones. (B) Superposition of the molecular surface of *T. maritima* Mre11:Rad50^{NBD (S-S)} and the *P. furiosus* Mre11 bound to branched DNA (PDB entry: 3DSD) (DNA colored in red; *Tm*Mre11 and *Tm*Rad50 are colored in blue and orange respectively; *Pf*Mre11 is not shown for clarity). While Rad50 blocks the Mre11 dsDNA binding site in the ATP bound state (left hand view), the surface shows holes between Rad50 and Mre11 that are in principle large enough to harbor ssDNA (right hand view).

5. Discussion

DNA damages, in particular double strand breaks (DSBs) display a huge hazard to genome integrity and therefore cell viability. DSBs can arise as a result of exo- and endogenous sources, thus modifying the DNA either direct or indirect (Borde and Cobb, 2009; Khanna and Jackson, 2001). If repair of these lesions occur inappropriate or, at worst, completely fails the cell has to accomplish various modes of chromosome aberrations or even cell death (Costanzo et al., 2001). The Mre11:Rad50:Nbs1 (MRN; MRX in *S. cerevisiae*; MR in prokaryotes; also known as SbcCD in bacteria) complex describes such a keystone complex, involved in DSB sensing, nucleolytic processing of DNA ends, recruitment of DSB processing enzymes, damage signaling and participates as a scaffolding protein (Mirzoeva and Petrini, 2001; Sharples and Leach, 1995). MR is highly conserved in sequence throughout all domains of life, emphasizing its impact on genome maintenance. Disregarding Nbs1, which is restricted to eukaryotes, MR has conserved morphological features and enzymatic activities, suggesting a conserved framework and mechanism in all living organisms. The catalytic core consists of the Mre11 nuclease dimer and two molecules of the Rad50 ABC ATPase. A large flexible coiled-coil region sticks out of the catalytic head of Rad50 and links the N- and C-terminal ABC segments (Assenmacher and Hopfner, 2004). The high resolution structure of the bacterial MR complex in its ATP-free state shows an elongated shape, with the Mre11 dimer in the center and a Rad50 monomer on each outer tip (Bemeleit, 2007; Lammens et al., 2011). Based on the fact that dimer assembly is essential for ABC ATPase function (Hopfner and Tainer, 2003), it was considered important to gain insights about the occurring conformational changes of MR upon ATP binding. Moreover, little is known about MR's DNA binding mechanism, a further question for this thesis. To this end, the single components and the catalytic head of the bacterial *Thermotoga maritima* (*Tm*) MR complex were characterized structurally and biochemically.

5.1. Two states of Mre11^{HLH}:Rad50^{NBD}

Even though the archaeal bipartite Rad50 ATP binding cassette had been crystallized in its ATP-bound state previously (Hopfner et al., 2000b) and the sequence of this domain is about 25% identical and about 45-50% similar to the bacterial *T. maritima*, the structure lacked the important coiled-coil domain and could not give insights into how

ATP might impact on the orientation of the coiled-coils as well as the interaction with Mre11. Therefore Rad50's nucleotide binding domain (NBD) together with approx. 50 amino acids of the Mre11 binding coiled-coil region and Mre11's helix-loop-helix (HLH) domain was crystallized to gain insights into the structural framework.

The high resolution structure of *Tm*Mre11^{HLH}:Rad50^{NBD} bound to the non-hydrolyzable ATP analog AMPPNP offers a detailed view of nucleotide coordination and hydrolysis. The resulting electron density was of high quality and nicely visualized the protein-protein interaction between Rad50's coiled-coil and Mre11's C-terminal HLH domain (designated as interface 1) (Figure 32). Interface 1 is stabilized mainly by hydrophobic patches which are highly conserved from bacteria to higher eukaryotes. Moreover mutations in interface 1 resulted in DNA damage sensitivity in *S. cerevisiae* yeast strains examined *in vivo* by the response to genotoxins (Lammens et al., 2011). The large interaction area of 1334 Å², the genetic studies and the high similarity of this interaction region to the nucleotide free, open state of MR (PDB entry: 3QG5) (Bemeleit, 2007; Lammens et al., 2011), emphasizes the biological relevance of this anchor point between Mre11 and Rad50 in DSB repair.

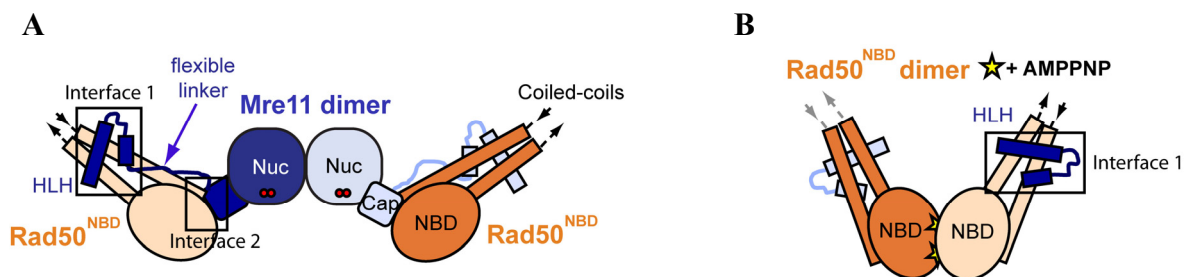


Figure 32: Schematic representation of (A) the *T. maritima* Mre11:Rad50^{NBD} complex in its nucleotide free state (PDB entry: 3QG5) and (B) *T. maritima* Mre11^{HLH}:Rad50^{NBD} bound to AMPPNP. Mre11 is colored in blue, Rad50 is colored in orange. The macromolecular interfaces 1 and 2 are highlighted by black boxes. Important domains are annotated.

The flexible linker that connects Mre11's nuclease module with the HLH domain in the nucleotide free MR complex potentially facilitates large conformational changes based on ATP and/or DNA binding (Figure 32). Besides interface 1, tight Rad50 NBD engagement upon ATP binding results in an approx. 50° rotation of the signature motif helix in respect to the Walker motifs, consequently resulting in a 50° rotation of the coiled-coil-HLH-

interacting region with respect to the N-terminal ABC-ATPase domain (lobe I) (Figure 10). As a consequence ATP-binding and therefore the formation of the engaged NBDs strongly affects the angle between the two coiled-coils protruding from the DNA binding catalytic head, consistent with scanning force microscopy of human MRN (Moreno-Herrero et al., 2005), where DNA binding was shown to alter the angle between two coiled-coils by about 60° . Comparing the angle between the coiled-coils in the nucleotide free, open conformation ($\sim 120^\circ$) and the ATP-bound, closed state ($\sim 60^\circ$), there is also a difference of about 60° . This suggests that the movement in the catalytic head from the nucleotide free MR complex to the ATP-bound conformation with engaged NBDs is the molecular basis for the observed mesoscale movements of the MRN coiled-coils upon DNA binding. The ATP-driven domain rotation in *P. furiosus* Mre11^{HLH(RBD)}:Rad50^{NBD} was suggested to be transduced to a ~ 30 Å linear pull on the linker region connecting the HLH domain with the nuclease module of Mre11 (Williams et al., 2011). Therefore, the repositioning of the coiled-coils with respect to the ATPase core could presumably transmit conformational changes to substrate-specific domains of Mre11 therefore stimulating DNA binding and processing activity (Hopfner and Tainer, 2003). Furthermore, the high resolution structure of the *Tm*Mre11^{HLH}:Rad50^{NBD}:AMPPNP complex enabled the alignment of the tertiary ATPase domain structures between *P. furiosus* (PDB entry: 1F2U) and *T. maritima*. Both structures are quite similar, with overall rms deviations of 2.05 Å, highlighting the similarity of morphological features in bacteria and archaea.

So far, two different states of Rad50's nucleotide binding domains are known, the nucleotide unbound NBDs which resembles also the conformation in its ADP-bound state (Hopfner and Tainer, 2003) and the ATP-bound state, which results in reorientation of the signature motif helix and therefore mesoscale movements of the coiled-coil domain. To analyze if Rad50's ATPase mechanism is affected in a third state, for instance the transition state like in P-Type ATPases where phosphorylation of a specific amino acid leads to a conformational change and therefore to the pumping power of the ATPase (Kuhlbrandt, 2004), Mre11^{HLH}:Rad50^{NBD} of *T. maritima* was crystallized bound to ADP orthovanadate. Since the orthovanadate ion has similar size and charge to inorganic phosphate, it can adopt its trigonal bipyramidal coordination, therefore mimicking the phosphate ion transition state expected during phosphoryl transfer. Based on these features, vanadate is a valuable tool for studying enzyme mechanism (Smith and Rayment, 1996).

Structural comparison of the Rad50 ATP binding region in AMPPNP-bound and ADP[VO₄]³⁻-state revealed no large conformational changes. These results suggest that ATP hydrolysis is not synchronized with a force-generating step leading to a stimulation of enzymatic action. This is in opposition to the proposed model where Rad50 might enter an adenylate kinase cycle as a result of occurring conformational changes upon ATP hydrolysis, which would necessarily reduce the distance between the two ATP binding sites from approx. 35Å to approx. 16Å (Bhaskara et al., 2007). However, Rad50 could stimulate the nuclease activity of Mre11 either by ATP-binding and/or ATP-release.

In summary, the Mre11:Rad50 complex has to undergo large open-to-closed conformational changes upon ATP binding. Linkage between the Rad50 coiled-coils and Mre11's HLH domain in interface 1 seems to be essential as an anchor point. In addition, the conformational changes driven by nucleotide binding lead to an alteration of the coiled-coil domains with respect to the ATPase core which is suitable to mediate communication within and between MR(N) complexes. In contrast, phosphoryl transfer does not seem to play a role in energy transfer followed by conformational alterations or stimulation of the adjacent substrate domain.

5.2. Trapping ATP dependent NBD-NBD formation

SAXS experiments with and without ATP revealed that the complex exists in at least two different states, indicating the engagement-disengagement cycle of Rad50 ATPases, similar to that seen in other ABC ATPases (Bemeleit, 2007; Liu et al., 1999; Moody et al., 2002). The nucleotide bound MR complex with closed NBDs could not be stabilized, even in the presence of non-hydrolyzable ATP analogs or by using an ATP-hydrolysis deficient mutant protein. To provide a structural framework for the architecture and ATP dependent conformational changes of the entire MR complex, the NBD-NBD domains had to be trapped in its ATP bound state. On the basis of the previously solved Mre11^{HLH}:Rad50^{NBD} structure bound to AMPPNP, two cysteine residues could be specifically introduced in Rad50^{NDB}. While these residues are far apart from each other in the nucleotide free MR complex, they are perfectly positioned to stabilize the ATP dependent NBD dimer by forming disulfide bonds across the NBD-NBD interface in the ATP bound, engaged state. The relatively moderate disulfide bonding efficiency of approx. 30%, consistent with SAXS data achieved with ATP γ S, raised the idea that the nucleotide

free conformation is stabilized via a transient structure. The second interaction site between Rad50 and Mre11 (designated as interface 2) not only comprises a relatively small area but also consists partly of the signature motif which is indispensable for ATP binding, therefore interface 2 is presumably representing this transiently stabilizing structure. Mutations introduced in interface 2 slightly increased the ATP hydrolysis activity of Rad50. Moreover, via specific substitution of a phenylalanine residue to a serine residue in position Mre11^{F291}, equilibrium could be shifted from the open to the closed state as confirmed by the increased disulfide bonding efficiency of approx. 65%. The well-directed trapping of the ATP bound state was key in analyzing the closed conformation of MR.

5.3. Mre11:Rad50^{NBD (S-S)} in its ATP/ADP bound state

Due to trapping of the ATP bound engaged Rad50 NBDs by disulfide bridging, it was possible to solve the crystal structure of the *T. maritima* Mre11:Rad50^{NBD (S-S)} (*TmMR*^{NBD (S-S)}) complex, trapped in its ATP/ADP bound state. Although ATP was hydrolyzed to ADP in the course of disulfide bridging or crystallization, the NBD dimer is structurally similar to the AMPPNP bound form of the Rad50^{NBD} dimer. This similarity not only emphasizes the relevance of the presented ATP dependent conformational changes of MR, it also suggests that disulfide bond stabilization could be a general approach to trap ABC enzymes in the ATP bound state for structural studies.

Together with the structure of *T. maritima* Mre11:Rad50^{NBD} in the open nucleotide free state, the illustrated structure in its ATP/ADP bound state allows the study of the ATP dependent conformational cycle of the MR complex (Figure 33). ATP induces a remarkably large transition which leads to an axial rotation of the Rad50 coiled-coils with respect to each other and an inverted orientation of them with respect to Mre11. This conformational switch is consistent with the previously proposed “clamp” model of MR (Williams et al., 2011). Furthermore, SAXS experiments of the bacterial Mre11:Rad50^{NBD} catalytic head domain resulted in a substantial decrease of the radius of gyration (R_g) from 230 Å to 193 Å as well as a more articulated peak at shorter vectors and a significant decrease of the long vectors in the pair distribution function $P(r)$ when ATP γ S was added to the solution (Lammens et al., 2011). This resembles the SAXS data of the *TmMre11:Rad50^{NBD}* complex with BMOE crosslinked and disulfide bonded NBDs, supporting the conclusion that the MR crystal structure in its ATP/ADP bound state

matches the conformation of the complex in solution. In fact, stabilization of MR in open and closed conformations by either interface 2 or ATP suggests an at least two state switch for the bacterial complex, although additional conformations in the presence of DNA cannot be ruled out which will be discussed later on.

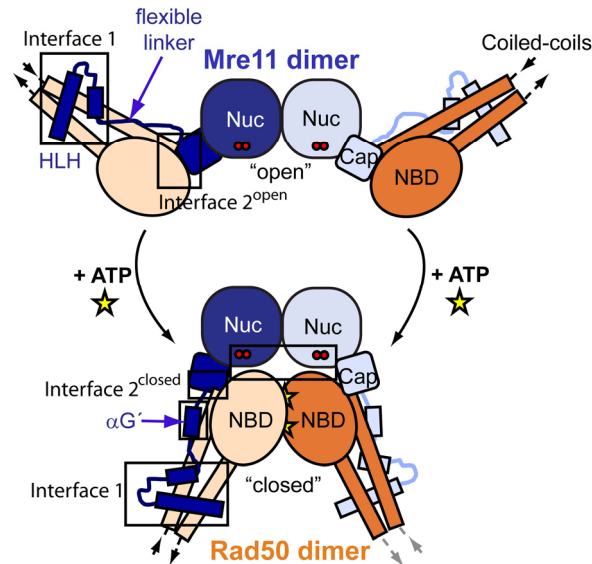


Figure 33: Schematic representation of the overall domain movement within the *T. maritima* Mre11:Rad50^{NBD} complex upon nucleotide binding. Mre11 is colored in blue, Rad50 is colored in orange. The interfaces 1 and 2 are highlighted by black boxes. Important domains and motifs are annotated.

Besides the obvious nucleotide-driven conformational change within the whole complex several minor alterations occurred, likely to be important for MR's function. Helix αG^{turn} is flipped around 90° from the open to the closed state, therefore enabling with its flexibility the large conformational relocation of the Rad50 NBDs. Moreover, the flexible linker connecting Mre11's capping domain with the HLH motif in the open conformation undergoes a disorder-to-order transition by forming a well-ordered α -helix ($\alpha G'$) (Figure 33). Still, the most notable result of the closed Mre11:Rad50^{NBD (S-S)} complex is the blocking of Mre11's dsDNA binding/active site groove by the Rad50 NBD dimer. In fact it is possible that ATP binding to Rad50 regulates MR by sterically controlling access to Mre11's nuclease and DNA binding sites and that the new formed $\alpha G'$ acts as a kind of flexible spring at the lateral entry side allowing conformational changes to enable access to the active site and/or functions in DNA binding. In addition, Mre11 interacts with Rad50 in

the newly formed interface 2^{closed} in a rather small and polar buried surface area, making conformational changes between the flexible modules not inconceivable (see section 5.6).

At the same time as the structure of *Tm*Mre11:Rad50^{NBD (S-S)} in its ATP/ADP bound state was solved, Yunje Cho and coworkers reported a related structure of archaeal Mre11:Rad50^{NBD} bound to the non-hydrolyzable ATP analog ATP γ S (Lim et al., 2011). The structure of archaeal MR in the absence of ATP is not known at present. However, SAXS analysis based on the archaeal *Pyrococcus furiosus* (*Pf*)MR^{NBD} complex indicate as well a two state mechanism with an elongated conformation of MR in its ATP-free, and a closed conformation with engaged NBDs in its ATP bound state (Figure 34). Together with the high degree of similarity between the structures of the ATP/ADP state of bacterial MR and ATP γ S bound state of archaeal MR it can be suggested that the ATP induced conformational cycle is an evolutionarily conserved feature of the complex. Moreover, the high similarity of the structures rules out crystallization artifacts as a result of site specific mutation and disulfide bridging.

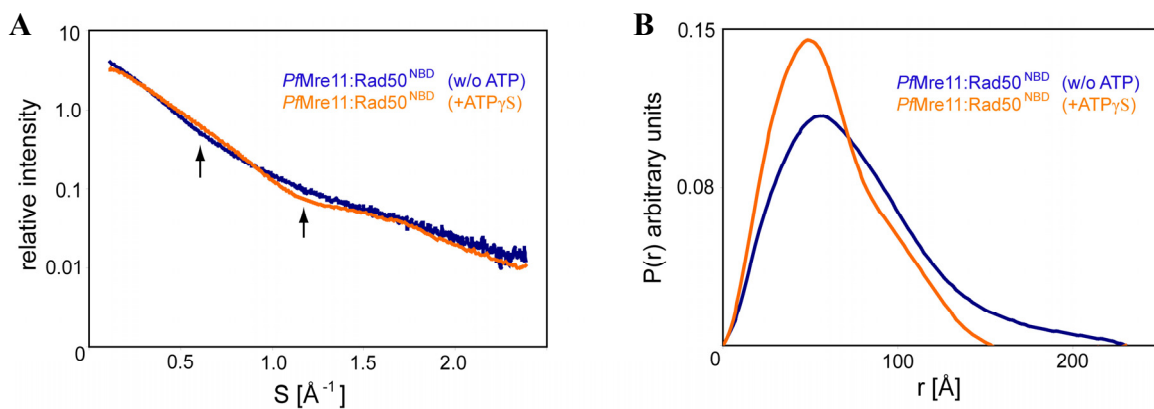


Figure 34: ATP induced conformational cycle of archaeal *P. furiosus*. (A) Superposition of experimental SAXS curves of *P. furiosus* MR^{NBD} with and without ATP γ S illustrate a to *T. maritima* likewise conformational change upon ATP binding. This suggests, that also archaeal MR exists in solution as open nucleotide unbound and closed ATP bound conformation. (B) The related electron pair distance distribution function $P(r)$ shows an increase of short distances and a decrease in long distances upon ATP γ S binding. Residual long distances match the prediction of a heterogeneous mixture between the open and closed ATP bound complex.

5.4. DNA binding mechanism of MR

Both prokaryotic and eukaryotic MR(N) bind DNA with a rather medium affinity and do not show a clear preference for single stranded or double stranded DNA, DNA ends or hairpins (de Jager et al., 2001; Lim et al., 2011). Anyway, stabilization of the closed, nucleotide bound conformation increased the affinity of MR to DNA, indicating that the engaged clamp-like form displays the DNA binding conformation. Even though the whole MR complex does not seem to have a preference for binding a specific DNA type, analyzing the single components of MR revealed a preference for Mre11^{HLH}:Rad50^{NBD}, lacking Mre11's phosphodiesterase and capping domains, to double stranded DNA. Thus, the nucleotide bound closed MR complex could bind dsDNA via the dimeric NBD-HLH module, whereas the Mre11 nuclease and capping domains might still bind ssDNA but are blocked from binding dsDNA. These data are consistent with the biochemistry of the bacteriophage Mre11:Rad50 homolog. Here, the dsDNA exonuclease was inhibited by ATP γ S, at least for processive degradation, while ssDNA endonuclease was not (Herdendorf et al., 2011). The phosphodiesterase and capping domains of Mre11, previously identified as important dsDNA binding elements (Williams et al., 2008), does not seem to play a major role for dsDNA binding in the closed complex. The precise interaction of MR with DNA ends remains to be seen, but it was not possible to detect disulfide bridged MR around single and double stranded plasmid DNA, respectively. Additionally, the disulfide bridged complex was still able to bind to DNA whose ends were blocked on both 5' ends by a fluorescein specific single chain Fab antibody fragment. It appears that the closed ATP bound complex does not entrap dsDNA like other DNA associated rings e.g. PCNA or specific helicases and that ends are not simply recognized by a topological ring (Bowman et al., 2004). This does not exclude the possibility that the open, elongated form of the MR complex can still bind to internal stretches of DNA. However, superimposition of the bacterial Mre11:Rad50^{NBD} complex in its ATP/ADP bound state on the archaeal Mre11 dimer bound to either synaptic DNA ends or branched DNA illustrate, that in both cases the Mre11 bound DNA would interfere with the NBDs of Rad50 (Figure 30) (Williams et al., 2008). In other words, Mre11's binding groove is completely blocked by the Rad50^{NBD} dimer, making access of dsDNA impossible. The positive patch in Rad50's groove suitable in size and charge to double stranded DNA (Figure 31A), together with the data of Mre11^{HLH}:Rad50^{NBD}'s preference for dsDNA, support the idea that the Rad50 dimer harbors an additional dsDNA binding site.

Furthermore, positively charged surface patches are located on the lateral side of Rad50 (Figure 31A). Y. Cho and coworkers identified several positively charged residues in the archaeal MR^{NBD} complex verified to be involved in DNA binding (Lim et al., 2011). Superimposition of the bacterial and archaeal ATP bound MR^{NBD} complex structures identified the corresponding positively charged residues in the MR complex of *Thermotoga maritima*. Thus residue R132 and K147 located in the central Rad50 groove matches R123 and K144 in *M. jannaschii* involved in DNA binding. DsDNA binding along such an NBD-NBD interface was proposed for the distantly related bacterial recombination enzyme RecF in the RecFOR pathway (Koroleva et al., 2007). The residues predicted to guide the DNA from the DNA binding site of Rad50's groove to the active site in Mre11 namely K897 and R902 in the archaeal complex correspond to K750 and K756 in the bacterial MR^{NBD} complex. Both patches may potentially form dsDNA binding sites (see section 5.6).

In summary, the structural and biochemical data of the closed *T. maritima* Mre11:Rad50^{NBD (S-S)} complex in its ATP/ADP bound state suggests that the previously identified dsDNA binding site of the Mre11 catalytic domain dimer is unlikely the dsDNA binding site of MR in the presence of ATP (Williams et al., 2008). This is in agreement with the recently reported structure of the archaeal MR complex bound to ATP γ S (Lim et al., 2011).

5.5. Interacting partners of MR(N)

Even though MR(N) is a key player in DSB repair and seems to sense and bind as one of the first proteins to DSBs (Stracker et al., 2004), it is remarkable that MR(N) shows a rather weak affinity to DNA (μ M range). One reason for this could be interactions with accessory proteins, such as with other enzymes involved in DSB repair.

SSB protein might be, in addition to its role in preventing secondary structures of free ssDNA, involved in recruitment of different repair proteins (Richard et al., 2011a). The interactome of *B. subtilis* SSB was recently estimated to include at least 12 proteins amongst others Rad50 (Costes et al., 2010). Moreover, human SSB1 was shown to be recruited to sites of DSBs in all interphase cells independently of MRN. It seems to function upstream of MRN, promoting its recruitment and even more hSSB1 was shown to stimulate Mre11's endonuclease activity (Richard et al., 2011a; Richard et al., 2011b).

Whereas hSSB1 seems to interact with Nbs1, human RPA was suggested to bind Mre11 and Nbs1 (Oakley et al., 2009; Richard et al., 2011a). However, the precise role of SSB/RPA together with MR(N) in DSB sensing, protein recruitment and signaling needs to be investigated, but this interaction could be an explanation why MR(N) on its own shows rather weak DNA binding and nuclease activity *in vitro*.

Another interaction site of MR(N) could be the Rad50S mutation cluster which is a surface patch that is thought to form a meiosis-specific protein interaction site (Alani et al., 1990; Usui et al., 2006). One interaction partner could be Sae2 (CtIP in mammals and Ctp1 in *S. pombe*) since deletion of Sae2 leads to a similar phenotype than Rad50S mutations (McKee and Kleckner, 1997). However, it is conceivable that this cluster is also involved in DNA interaction.

Besides this, further protein interactions with MRN have also been proposed. For instance, MRN was shown to stimulate resection by BLM and Dna2 by increasing the affinity of the helicase BLM for DNA ends but also by recruiting BLM to partially resected DNA (Nimonkar et al., 2011). Consistent with this interpretation, coimmunoprecipitation experiments showed that *Xenopus* Dna2 interacts with Nbs1 (Wawrousek et al., 2010). In addition, MRN was shown to stimulate together with RPA and BLM the resection by Exo1, by recruiting and by stimulating Exo1's processivity (Nimonkar et al., 2011). Biochemical data of *P. furiosus* also indicates a functional interplay in resection of MR together with a helicase and a nuclease (Hopkins and Paull, 2008). In addition, it is possible that DNA ends are first bound by the high affinity binder Ku70/80, which is then released by MRN and Ctp1 to assist recombinational repair as shown for *S. pombe* (Langerak et al., 2011). Studies revealed also that MRN promotes non-homologous end-joining repair in *S. cerevisiae* (Chen et al., 2001; Zhang and Paull, 2005).

In summary, various enzymes involved in DSB repair were shown to interact with or to be recruited by MR to DSBs, but physical and specific interaction needs to be investigated in most cases. Even though the structures of MR in its nucleotide bound and nucleotide free states show no clear evidence for protein-protein interactions and/or DSB end binding, such alternatives to address the rather low DNA binding affinity of MR(N) cannot be disregarded.

5.6. Working model of MR for DNA tethering and DSB processing

The data presented in this work allow the deduction of the ATP dependent conformational cycle of the MR complex, implying an at least two state switch (open-to-closed) for the bacterial complex, even though additional conformations in the presence of DNA are conceivable. However the Mre11 capping domains might play a role as key site for the transient stabilization of functional states of the MR complex and orients Rad50's NBDs. Although ATP binding can induce a transition to the closed form even in absence of DNA, it is conceivable that formation of the closed state is additionally promoted by dsDNA because it binds to this state with higher affinity. For instance, DNA binding to the capping domains of Mre11 could help Mre11 to release the NBDs from interface 2, allowing them to adopt a closed conformation in the presence of ATP. Thus, the working model includes dsDNA and ATP which cooperatively transform MR from the open to the closed state, giving MR a key role in both DNA tethering and DNA processing.

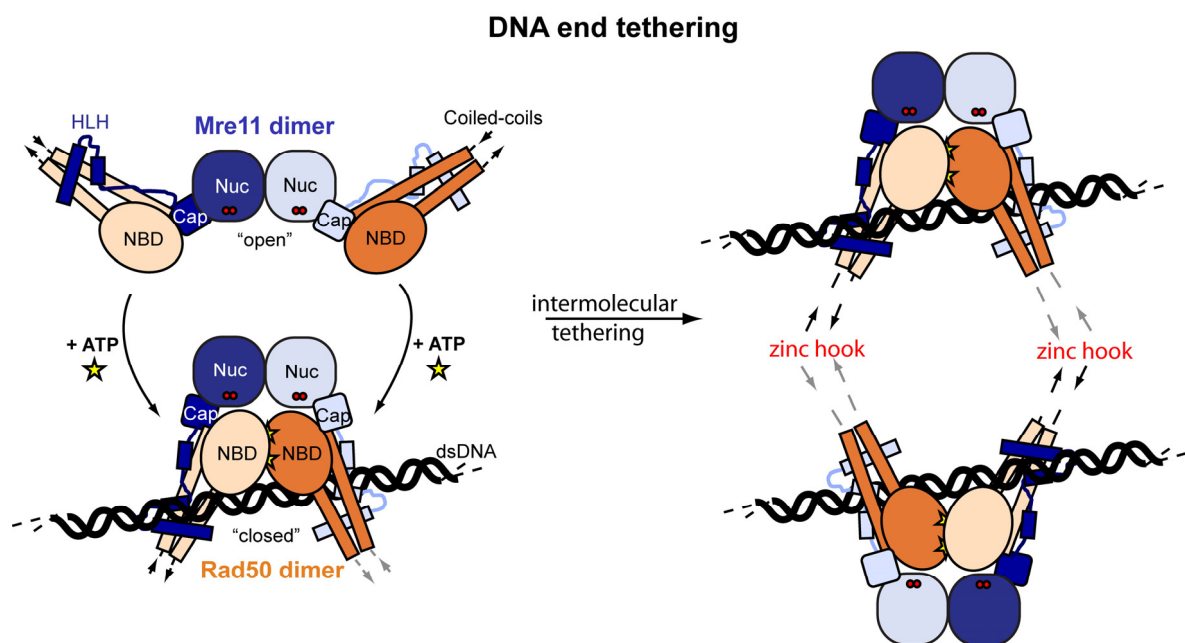


Figure 35: Proposed clamp model for DNA tethering. Hypothetical model for ATP-dependent tethering of dsDNA ends by the MR complex. The extended coiled-coil domains of Rad50 undergo an extensive conformational reorientation, which could open up the zinc hook interaction after ATP-dependent engagement and allow for intermolecular interaction between different MR complexes via the zinc hook. The proposed DNA-binding groove (Figure 31A) could orient two DNA ends or sister chromatids in close proximity to each other.

A possible molecular mechanism for ATP dependent DNA tethering can be seen by comparing the open and the ATP-bound closed form (Figure 35). The conformational transition turns Rad50 around as well is leading to an axial rotation of the Rad50 coiled-coil domains with respect to each other. Even though the coiled-coil domains are flexible (de Jager et al., 2004), the axial rotation of coiled-coils and zinc hook domains could prevent intramolecular tethering after ATP dependent engagement. This could liberate the zinc-hooks to allow intermolecular tethering of different MR complexes as seen by atomic force microscopy (AFM) in response to DNA binding to MRN (Figure 35) (Moreno-Herrero et al., 2005). However, in this study, ATP alone did not result in a conformational change as observed from the structures reported here as well as for the related archaeal system (Lim et al., 2011). These discrepancies can be explained if both ATP and DNA act cooperatively to induce the open-to-closed transition. This model also explains the tethering functions of MR(N) by preventing Mre11 dependent degradation of dsDNA ends.

The working model for MR in DSB processing is mainly based on the structural insights achieved by the Mre11:Rad50^{NBD} complex in its ATP-free and its ATP/ADP bound state combined with biochemical data including DNA affinity of the single MR components (Figure 36). Nevertheless, Mre11's dsDNA binding site could be important for 3'-5' exonuclease activity in the open form, for instance to degrade 3' ends to generate suitable substrates for repair synthesis or overhangs at microhomologies for NHEJ (Rahal et al., 2010). However, in the closed form Rad50 blocks the dsDNA binding site of Mre11 making access by dsDNA unfeasible. Positively charged surface patches in Rad50's groove and on the lateral site on Rad50 might bind dsDNA. However in both cases the DNA is rather distal to the Mre11 nuclease active site, making it at present unclear how DNA and ATP binding and DNA processing are functionally coupled. One explanation is that ATP dependent engagement of the NBDs could unwind dsDNA ends with one of the ssDNA strands binding between Rad50 and Mre11 since a single strand could fit through the tunnel. MRN was shown to melt/unwind short dsDNA oligonucleotides in the presence of ATP (Paull and Gellert, 1999). Even though Rad50 blocks the dsDNA binding site, a gap in the molecular surface on each side between Rad50 and Mre11 reaches the Mre11 active site and is large enough to accommodate ssDNA (Figure 31B). Several loops on Mre11 flanking this hole are unstructured in the illustrated crystal structure. Proteins from thermophilic organisms generally have well folded loops and unstructured loops often indicate unsaturated ligand or DNA binding sites. A structural motif for DNA binding is

also seen on the Rad50 side of this gap. Here, the helix $\alpha G'$, which connects the HLH and capping domain, is formed out of a flexible linker region as a result of the open-to-closed transition. Consequently, a right-angled helix-loop-helix structure appears at the lateral entry side to Mre11's nuclease cleft (αG^{turn} -loop- $\alpha G'$). The equivalent region of *S. cerevisiae* Mre11 is implicated in DNA binding (Usui et al., 1998), thus this transient helix-loop-helix structure might be involved in DNA recognition in the clamp/closed state.

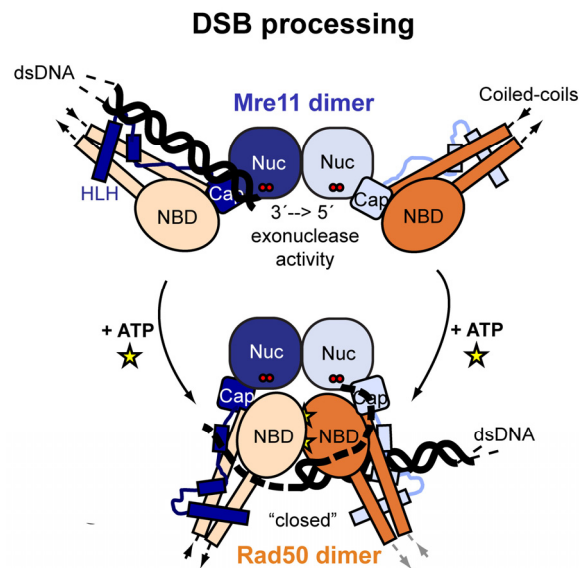


Figure 36: Proposed clamp model for DSB processing. Proposed model for ATP-controlled DSB processing. ATP driven conformational changes of the MR head module could be responsible for the unwinding of double stranded DNA and promote endonucleolytic cleavage of single-stranded DNA or hairpins.

The working model of DSB processing in the ATP bound state, where dsDNA is excluded but ssDNA can still bind to Mre11's nuclease active site also matches much of the known *in vitro* data. For instance, Mre11's ssDNA endonuclease activity was shown to be neither dependent on ATP nor inhibited by ATP analogs (Herdendorf et al., 2011). In addition, this model would fit data where the generation of a 15-55 nucleotides long 3' ssDNA tail by endonucleolytic cleavage from the DNA end is promoted by ATP or ATP γ S, rather than inhibited. This event could possibly combine DNA unwinding and endonucleolytic cleavage and is maybe dependent on protein conjugates or adducts at the 5' strand of the DSB (Hopkins and Paull, 2008).

However, the possibility remains that there might be a further conformational state of MR induced by DNA, allowing simultaneous dsDNA binding across the Mre11 dimer interface as seen previously (Williams et al., 2008) and the formation of the NBD dimer as seen in this work. Due to the fact that the interaction of Mre11 and Rad50, apart from the anchoring HLH coiled-coil interaction being quite polar, it could be in principal modulated or disrupted by DNA. The linker between the HLH and capping domain is flexible and can adopt extended (open form) and helical (closed form, $\alpha G'$) conformations, perhaps allowing conformational flexibility between Mre11 and Rad50^{NBD} dimer. Nevertheless, the biochemical data shown in this thesis implies that MR does not encircle dsDNA, therefore assuming that Rad50 indeed competes with Mre11 in dsDNA binding in the presence of ATP and at the same time creates an additional dsDNA binding site. Therefore the exact nature of the interaction of *Tm*MR with DNA remains to be determined experimentally.

In conclusion, the presented structures and the biochemical data reveal new insights in the ATP-induced conformational cycle of MR and a working model for DNA tethering and processing of MR is proposed. However, based on the new structures, the precise interaction of DNA with MR needs to be evaluated and the correlation between ATP binding and hydrolysis by Rad50 combined with its endo- and exonucleolytic activity on dsDNA near DNA ends will be important for further work. Finally, possible interaction partners of MR(N) and the precise role of its functional interplay needs to be investigated.

6. References

- Adams, P.D., Grosse-Kunstleve, R.W., Hung, L.W., Ioerger, T.R., McCoy, A.J., Moriarty, N.W., Read, R.J., Sacchettini, J.C., Sauter, N.K., and Terwilliger, T.C. (2002). PHENIX: building new software for automated crystallographic structure determination. *Acta Crystallogr D Biol Crystallogr* 58, 1948-1954.
- Alani, E., Padmore, R., and Kleckner, N. (1990). Analysis of wild-type and rad50 mutants of yeast suggests an intimate relationship between meiotic chromosome synapsis and recombination. *Cell* 61, 419-436.
- Assenmacher, N., and Hopfner, K.P. (2004). MRE11/RAD50/NBS1: complex activities. *Chromosoma* 113, 157-166.
- Avery, O.T., Macleod, C.M., and McCarty, M. (1944). Studies on the Chemical Nature of the Substance Inducing Transformation of Pneumococcal Types : Induction of Transformation by a Desoxyribonucleic Acid Fraction Isolated from Pneumococcus Type iii. *J Exp Med* 79, 137-158.
- Baker, N.A. (2004). Poisson-Boltzmann methods for biomolecular electrostatics. *Methods Enzymol* 383, 94-118.
- Bakkenist, C.J., and Kastan, M.B. (2003). DNA damage activates ATM through intermolecular autophosphorylation and dimer dissociation. *Nature* 421, 499-506.
- Bassing, C.H., Ranganath, S., Murphy, M., Savic, V., Gleason, M., and Alt, F.W. (2008). Aberrant V(D)J recombination is not required for rapid development of H2ax/p53-deficient thymic lymphomas with clonal translocations. *Blood* 111, 2163-2169.
- Baudat, F., and Nicolas, A. (1997). Clustering of meiotic double-strand breaks on yeast chromosome III. *Proc Natl Acad Sci U S A* 94, 5213-5218.
- Bemeleit, D. (2007). Structural characterization of the DNA repair protein complex SbcC-SbcD of *Thermotoga maritima*.
- Bhaskara, V., Dupre, A., Lengsfeld, B., Hopkins, B.B., Chan, A., Lee, J.H., Zhang, X., Gautier, J., Zakian, V., and Paull, T.T. (2007). Rad50 adenylate kinase activity regulates DNA tethering by Mre11/Rad50 complexes. *Mol Cell* 25, 647-661.
- Borde, V. (2007). The multiple roles of the Mre11 complex for meiotic recombination. *Chromosome Res* 15, 551-563.
- Borde, V., and Cobb, J. (2009). Double functions for the Mre11 complex during DNA double-strand break repair and replication. *Int J Biochem Cell Biol* 41, 1249-1253.
- Bowman, G.D., O'Donnell, M., and Kuriyan, J. (2004). Structural analysis of a eukaryotic sliding DNA clamp-clamp loader complex. *Nature* 429, 724-730.

- Bryson, K., McGuffin, L.J., Marsden, R.L., Ward, J.J., Sodhi, J.S., and Jones, D.T. (2005). Protein structure prediction servers at University College London. *Nucleic Acids Res* 33, W36-38.
- Bzymek, M., Thayer, N.H., Oh, S.D., Kleckner, N., and Hunter, N. (2010). Double Holliday junctions are intermediates of DNA break repair. *Nature* 464, 937-941.
- Cadet, J., Bellon, S., Berger, M., Bourdat, A.G., Douki, T., Duarte, V., Frelon, S., Gasparutto, D., Muller, E., Ravanat, J.L., *et al.* (2002). Recent aspects of oxidative DNA damage: guanine lesions, measurement and substrate specificity of DNA repair glycosylases. *Biol Chem* 383, 933-943.
- Carney, J.P., Maser, R.S., Olivares, H., Davis, E.M., Le Beau, M., Yates, J.R., 3rd, Hays, L., Morgan, W.F., and Petrini, J.H. (1998). The hMre11/hRad50 protein complex and Nijmegen breakage syndrome: linkage of double-strand break repair to the cellular DNA damage response. *Cell* 93, 477-486.
- Chamankhah, M., and Xiao, W. (1999). Formation of the yeast Mre11-Rad50-Xrs2 complex is correlated with DNA repair and telomere maintenance. *Nucleic Acids Res* 27, 2072-2079.
- Chen, L., Trujillo, K., Ramos, W., Sung, P., and Tomkinson, A.E. (2001). Promotion of Dnl4-catalyzed DNA end-joining by the Rad50/Mre11/Xrs2 and Hdf1/Hdf2 complexes. *Mol Cell* 8, 1105-1115.
- Chu, G. (1997). Double strand break repair. *J Biol Chem* 272, 24097-24100.
- Ciccia, A., and Elledge, S.J. (2010). The DNA damage response: making it safe to play with knives. *Mol Cell* 40, 179-204.
- Cole, C., Barber, J.D., and Barton, G.J. (2008). The Jpred 3 secondary structure prediction server. *Nucleic Acids Res* 36, W197-201.
- Connelly, J.C., de Leau, E.S., and Leach, D.R. (1999). DNA cleavage and degradation by the SbcCD protein complex from *Escherichia coli*. *Nucleic Acids Res* 27, 1039-1046.
- Connelly, J.C., de Leau, E.S., and Leach, D.R. (2003). Nucleolytic processing of a protein-bound DNA end by the *E. coli* SbcCD (MR) complex. *DNA Repair (Amst)* 2, 795-807.
- Connelly, J.C., de Leau, E.S., Okely, E.A., and Leach, D.R. (1997). Overexpression, purification, and characterization of the SbcCD protein from *Escherichia coli*. *J Biol Chem* 272, 19819-19826.
- Connelly, J.C., Kirkham, L.A., and Leach, D.R. (1998). The SbcCD nuclease of *Escherichia coli* is a structural maintenance of chromosomes (SMC) family protein that cleaves hairpin DNA. *Proc Natl Acad Sci U S A* 95, 7969-7974.
- Connelly, J.C., and Leach, D.R. (1996). The *sbcC* and *sbcD* genes of *Escherichia coli* encode a nuclease involved in palindrome inviability and genetic recombination. *Genes Cells* 1, 285-291.

- Constantinesco, F., Forterre, P., Koonin, E.V., Aravind, L., and Elie, C. (2004). A bipolar DNA helicase gene, *herA*, clusters with *rad50*, *mre11* and *nurA* genes in thermophilic archaea. *Nucleic Acids Res* 32, 1439-1447.
- Costanzo, V., Robertson, K., Bibikova, M., Kim, E., Grieco, D., Gottesman, M., Carroll, D., and Gautier, J. (2001). Mre11 protein complex prevents double-strand break accumulation during chromosomal DNA replication. *Mol Cell* 8, 137-147.
- Costes, A., Lecointe, F., McGovern, S., Quevillon-Cheruel, S., and Polard, P. (2010). The C-terminal domain of the bacterial SSB protein acts as a DNA maintenance hub at active chromosome replication forks. *PLoS Genet* 6, e1001238.
- Cowtan, K. (2006). The Buccaneer software for automated model building. 1. Tracing protein chains. *Acta Crystallogr D Biol Crystallogr* 62, 1002-1011.
- Cromie, G.A., Connelly, J.C., and Leach, D.R. (2001). Recombination at double-strand breaks and DNA ends: conserved mechanisms from phage to humans. *Mol Cell* 8, 1163-1174.
- Dahm, R. (2008). Discovering DNA: Friedrich Miescher and the early years of nucleic acid research. *Hum Genet* 122, 565-581.
- Darmon, E., Eykelenboom, J.K., Lincker, F., Jones, L.H., White, M., Okely, E., Blackwood, J.K., and Leach, D.R. (2010). *E. coli* SbcCD and RecA control chromosomal rearrangement induced by an interrupted palindrome. *Mol Cell* 39, 59-70.
- de Jager, M., Trujillo, K.M., Sung, P., Hopfner, K.P., Carney, J.P., Tainer, J.A., Connelly, J.C., Leach, D.R., Kanaar, R., and Wyman, C. (2004). Differential arrangements of conserved building blocks among homologs of the Rad50/Mre11 DNA repair protein complex. *J Mol Biol* 339, 937-949.
- de Jager, M., van Noort, J., van Gent, D.C., Dekker, C., Kanaar, R., and Wyman, C. (2001). Human Rad50/Mre11 is a flexible complex that can tether DNA ends. *Mol Cell* 8, 1129-1135.
- Degrassi, F., Fiore, M., and Palitti, F. (2004). Chromosomal aberrations and genomic instability induced by topoisomerase-targeted antitumour drugs. *Curr Med Chem Anticancer Agents* 4, 317-325.
- Deng, Y., Guo, X., Ferguson, D.O., and Chang, S. (2009). Multiple roles for MRE11 at uncapped telomeres. *Nature* 460, 914-918.
- Deriano, L., Stracker, T.H., Baker, A., Petrini, J.H., and Roth, D.B. (2009). Roles for NBS1 in alternative nonhomologous end-joining of V(D)J recombination intermediates. *Mol Cell* 34, 13-25.
- Desai-Mehta, A., Cerosaletti, K.M., and Concannon, P. (2001). Distinct functional domains of nibrin mediate Mre11 binding, focus formation, and nuclear localization. *Mol Cell Biol* 21, 2184-2191.

- Dinkelmann, M., Spehalski, E., Stoneham, T., Buis, J., Wu, Y., Sekiguchi, J.M., and Ferguson, D.O. (2009). Multiple functions of MRN in end-joining pathways during isotype class switching. *Nat Struct Mol Biol* *16*, 808-813.
- Du, L., van der Burg, M., Popov, S.W., Kotnis, A., van Dongen, J.J., Gennery, A.R., and Pan-Hammarstrom, Q. (2008). Involvement of Artemis in nonhomologous end-joining during immunoglobulin class switch recombination. *J Exp Med* *205*, 3031-3040.
- Dudley, D.D., Chaudhuri, J., Bassing, C.H., and Alt, F.W. (2005). Mechanism and control of V(D)J recombination versus class switch recombination: similarities and differences. *Adv Immunol* *86*, 43-112.
- Durocher, D., and Jackson, S.P. (2002). The FHA domain. *FEBS Lett* *513*, 58-66.
- Edlinger, B., and Schlogelhofer, P. (2011). Have a break: determinants of meiotic DNA double strand break (DSB) formation and processing in plants. *J Exp Bot* *62*, 1545-1563.
- Emsley, P., and Cowtan, K. (2004). Coot: model-building tools for molecular graphics. *Acta Crystallogr D Biol Crystallogr* *60*, 2126-2132.
- Falck, J., Coates, J., and Jackson, S.P. (2005). Conserved modes of recruitment of ATM, ATR and DNA-PKcs to sites of DNA damage. *Nature* *434*, 605-611.
- Friedberg, E.C., McDaniel, L.D., and Schultz, R.A. (2004). The role of endogenous and exogenous DNA damage and mutagenesis. *Curr Opin Genet Dev* *14*, 5-10.
- Furuse, M., Nagase, Y., Tsubouchi, H., Murakami-Murofushi, K., Shibata, T., and Ohta, K. (1998). Distinct roles of two separable in vitro activities of yeast Mre11 in mitotic and meiotic recombination. *EMBO J* *17*, 6412-6425.
- Guy, C.P., and Bolt, E.L. (2005). Archaeal Hel308 helicase targets replication forks in vivo and in vitro and unwinds lagging strands. *Nucleic Acids Res* *33*, 3678-3690.
- Hanahan, D. (1983). Studies on transformation of *Escherichia coli* with plasmids. *J Mol Biol* *166*, 557-580.
- Harper, J.W., and Elledge, S.J. (2007). The DNA damage response: ten years after. *Mol Cell* *28*, 739-745.
- Helmink, B.A., Bredemeyer, A.L., Lee, B.S., Huang, C.Y., Sharma, G.G., Walker, L.M., Bednarski, J.J., Lee, W.L., Pandita, T.K., Bassing, C.H., *et al.* (2009). MRN complex function in the repair of chromosomal Rag-mediated DNA double-strand breaks. *J Exp Med* *206*, 669-679.
- Herdendorf, T.J., Albrecht, D.W., Benkovic, S.J., and Nelson, S.W. (2011). Biochemical characterization of bacteriophage T4 Mre11-Rad50 complex. *J Biol Chem* *286*, 2382-2392.
- Hershey, A.D., and Chase, M. (1952). Independent functions of viral protein and nucleic acid in growth of bacteriophage. *J Gen Physiol* *36*, 39-56.
- Heyer, W.D., Ehmsen, K.T., and Liu, J. (2010). Regulation of homologous recombination in eukaryotes. *Annu Rev Genet* *44*, 113-139.

- Hoeijmakers, J.H. (2001). Genome maintenance mechanisms for preventing cancer. *Nature* *411*, 366-374.
- Hoeijmakers, J.H. (2009). DNA damage, aging, and cancer. *N Engl J Med* *361*, 1475-1485.
- Hohl, M., Kwon, Y., Galvan, S.M., Xue, X., Tous, C., Aguilera, A., Sung, P., and Petrini, J.H. (2011). The Rad50 coiled-coil domain is indispensable for Mre11 complex functions. *Nat Struct Mol Biol*.
- Honegger, A., Spinelli, S., Cambillau, C., and Pluckthun, A. (2005). A mutation designed to alter crystal packing permits structural analysis of a tight-binding fluorescein-scFv complex. *Protein Sci* *14*, 2537-2549.
- Hopfner, K.P., Craig, L., Moncalian, G., Zinkel, R.A., Usui, T., Owen, B.A., Karcher, A., Henderson, B., Bodmer, J.L., McMurray, C.T., *et al.* (2002). The Rad50 zinc-hook is a structure joining Mre11 complexes in DNA recombination and repair. *Nature* *418*, 562-566.
- Hopfner, K.P., Karcher, A., Craig, L., Woo, T.T., Carney, J.P., and Tainer, J.A. (2001). Structural biochemistry and interaction architecture of the DNA double-strand break repair Mre11 nuclease and Rad50-ATPase. *Cell* *105*, 473-485.
- Hopfner, K.P., Karcher, A., Shin, D., Fairley, C., Tainer, J.A., and Carney, J.P. (2000a). Mre11 and Rad50 from *Pyrococcus furiosus*: cloning and biochemical characterization reveal an evolutionarily conserved multiprotein machine. *J Bacteriol* *182*, 6036-6041.
- Hopfner, K.P., Karcher, A., Shin, D.S., Craig, L., Arthur, L.M., Carney, J.P., and Tainer, J.A. (2000b). Structural biology of Rad50 ATPase: ATP-driven conformational control in DNA double-strand break repair and the ABC-ATPase superfamily. *Cell* *101*, 789-800.
- Hopfner, K.P., and Tainer, J.A. (2003). Rad50/SMC proteins and ABC transporters: unifying concepts from high-resolution structures. *Curr Opin Struct Biol* *13*, 249-255.
- Hopkins, B.B., and Paull, T.T. (2008). The *P. furiosus* mre11/rad50 complex promotes 5' strand resection at a DNA double-strand break. *Cell* *135*, 250-260.
- Huen, M.S., Sy, S.M., and Chen, J. (2010). BRCA1 and its toolbox for the maintenance of genome integrity. *Nat Rev Mol Cell Biol* *11*, 138-148.
- Hung, L.W., Wang, I.X., Nikaido, K., Liu, P.Q., Ames, G.F., and Kim, S.H. (1998). Crystal structure of the ATP-binding subunit of an ABC transporter. *Nature* *396*, 703-707.
- Ivanov, E.L., Sugawara, N., Fishman-Lobell, J., and Haber, J.E. (1996). Genetic requirements for the single-strand annealing pathway of double-strand break repair in *Saccharomyces cerevisiae*. *Genetics* *142*, 693-704.
- Jiricny, J. (1998). Replication errors: cha(lle)nging the genome. *EMBO J* *17*, 6427-6436.
- Jones, M.E. (1953). Albrecht Kossel, a biographical sketch. *Yale J Biol Med* *26*, 80-97.

- Kabsch, W. (1993). Automatic processing of rotation diffraction data from crystals of initially unknown symmetry and cell constants. *Journal of Applied Crystallography* 26, 795-800.
- Keeney, S., Giroux, C.N., and Kleckner, N. (1997). Meiosis-specific DNA double-strand breaks are catalyzed by Spo11, a member of a widely conserved protein family. *Cell* 88, 375-384.
- Keeney, S., and Neale, M.J. (2006). Initiation of meiotic recombination by formation of DNA double-strand breaks: mechanism and regulation. *Biochem Soc Trans* 34, 523-525.
- Khanna, K.K., and Jackson, S.P. (2001). DNA double-strand breaks: signaling, repair and the cancer connection. *Nat Genet* 27, 247-254.
- Konarev, P.V., Petoukhov, M.V., Volkov, V.V., and Svergun, D.I. (2006). ATSAS 2.1, a program package for small-angle scattering data analysis. *Journal of Applied Crystallography* 39, 277-286.
- Konarev, P.V., Volkov, V.V., Sokolova, A.V., Koch, M.H.J., and Svergun, D.I. (2003). PRIMUS: a Windows PC-based system for small-angle scattering data analysis. *Journal of Applied Crystallography* 36, 1277-1282.
- Koroleva, O., Makharashvili, N., Courcelle, C.T., Courcelle, J., and Korolev, S. (2007). Structural conservation of RecF and Rad50: implications for DNA recognition and RecF function. *EMBO J* 26, 867-877.
- Kuhlbrandt, W. (2004). Biology, structure and mechanism of P-type ATPases. *Nat Rev Mol Cell Biol* 5, 282-295.
- Kuzminov, A. (2001). Single-strand interruptions in replicating chromosomes cause double-strand breaks. *Proc Natl Acad Sci U S A* 98, 8241-8246.
- Laemmli, U.K. (1970). Cleavage of structural proteins during the assembly of the head of bacteriophage T4. *Nature* 227, 680-685.
- Lammens, K., Bemeleit, D.J., Möckel, C., Clausing, E., Schele, A., Hartung, S., Schiller, C.B., Lucas, M., Angermüller, C., Söding, J., *et al.* (2011). The Mre11:Rad50 structure shows an ATP-dependent molecular clamp in DNA double-strand break repair. *Cell* 145, 54-66.
- Langer, G., Cohen, S.X., Lamzin, V.S., and Perrakis, A. (2008). Automated macromolecular model building for X-ray crystallography using ARP/wARP version 7. *Nat Protoc* 3, 1171-1179.
- Langerak, P., Mejia-Ramirez, E., Limbo, O., and Russell, P. (2011). Release of Ku and MRN from DNA Ends by Mre11 Nuclease Activity and Ctp1 Is Required for Homologous Recombination Repair of Double-Strand Breaks. *PLoS Genet* 7, e1002271.
- Larkin, M.A., Blackshields, G., Brown, N.P., Chenna, R., McGettigan, P.A., McWilliam, H., Valentin, F., Wallace, I.M., Wilm, A., Lopez, R., *et al.* (2007). Clustal W and Clustal X version 2.0. *Bioinformatics* 23, 2947-2948.

- Lee, J.H., Ghirlando, R., Bhaskara, V., Hoffmeyer, M.R., Gu, J., and Paull, T.T. (2003). Regulation of Mre11/Rad50 by Nbs1: effects on nucleotide-dependent DNA binding and association with ataxia-telangiectasia-like disorder mutant complexes. *J Biol Chem* 278, 45171-45181.
- Lee, J.H., and Paull, T.T. (2005). ATM activation by DNA double-strand breaks through the Mre11-Rad50-Nbs1 complex. *Science* 308, 551-554.
- Lengsfeld, B.M., Rattray, A.J., Bhaskara, V., Ghirlando, R., and Paull, T.T. (2007). Sae2 is an endonuclease that processes hairpin DNA cooperatively with the Mre11/Rad50/Xrs2 complex. *Mol Cell* 28, 638-651.
- Lieber, M.R. (2010). NHEJ and its backup pathways in chromosomal translocations. *Nat Struct Mol Biol* 17, 393-395.
- Lim, H.S., Kim, J.S., Park, Y.B., Gwon, G.H., and Cho, Y. (2011). Crystal structure of the Mre11-Rad50-ATPgammaS complex: understanding the interplay between Mre11 and Rad50. *Genes Dev* 25, 1091-1104.
- Limbo, O., Chahwan, C., Yamada, Y., de Bruin, R.A., Wittenberg, C., and Russell, P. (2007). Ctp1 is a cell-cycle-regulated protein that functions with Mre11 complex to control double-strand break repair by homologous recombination. *Mol Cell* 28, 134-146.
- Limoli, C.L., Giedzinski, E., Bonner, W.M., and Cleaver, J.E. (2002). UV-induced replication arrest in the xeroderma pigmentosum variant leads to DNA double-strand breaks, gamma-H2AX formation, and Mre11 relocalization. *Proc Natl Acad Sci U S A* 99, 233-238.
- Lindahl, T. (1993). Instability and decay of the primary structure of DNA. *Nature* 362, 709-715.
- Lindahl, T., and Barnes, D.E. (2000). Repair of endogenous DNA damage. *Cold Spring Harb Symp Quant Biol* 65, 127-133.
- Liu, P.Q., Liu, C.E., and Ames, G.F. (1999). Modulation of ATPase activity by physical disengagement of the ATP-binding domains of an ABC transporter, the histidine permease. *J Biol Chem* 274, 18310-18318.
- Lorenz, M.G., and Wackernagel, W. (1994). Bacterial gene transfer by natural genetic transformation in the environment. *Microbiol Rev* 58, 563-602.
- Luo, G., Yao, M.S., Bender, C.F., Mills, M., Bladl, A.R., Bradley, A., and Petrini, J.H. (1999). Disruption of mRad50 causes embryonic stem cell lethality, abnormal embryonic development, and sensitivity to ionizing radiation. *Proc Natl Acad Sci U S A* 96, 7376-7381.
- Lupas, A., Van Dyke, M., and Stock, J. (1991). Predicting coiled coils from protein sequences. *Science* 252, 1162-1164.
- Mahaney, B.L., Meek, K., and Lees-Miller, S.P. (2009). Repair of ionizing radiation-induced DNA double-strand breaks by non-homologous end-joining. *Biochem J* 417, 639-650.

- Mansour, W.Y., Schumacher, S., Roskopf, R., Rhein, T., Schmidt-Petersen, F., Gatzemeier, F., Haag, F., Borgmann, K., Willers, H., and Dahm-Daphi, J. (2008). Hierarchy of nonhomologous end-joining, single-strand annealing and gene conversion at site-directed DNA double-strand breaks. *Nucleic Acids Res* *36*, 4088-4098.
- Mascarenhas, J., Sanchez, H., Tadesse, S., Kidane, D., Krisnamurthy, M., Alonso, J.C., and Graumann, P.L. (2006). *Bacillus subtilis* SbcC protein plays an important role in DNA inter-strand cross-link repair. *BMC Mol Biol* *7*, 20.
- McCoy, A.J. (2007). Solving structures of protein complexes by molecular replacement with Phaser. *Acta Crystallogr D Biol Crystallogr* *63*, 32-41.
- McKee, A.H., and Kleckner, N. (1997). A general method for identifying recessive diploid-specific mutations in *Saccharomyces cerevisiae*, its application to the isolation of mutants blocked at intermediate stages of meiotic prophase and characterization of a new gene SAE2. *Genetics* *146*, 797-816.
- Mirzoeva, O.K., and Petrini, J.H. (2001). DNA damage-dependent nuclear dynamics of the Mre11 complex. *Mol Cell Biol* *21*, 281-288.
- Mladenov, E., and Iliakis, G. (2011). Induction and repair of DNA double strand breaks: the increasing spectrum of non-homologous end joining pathways. *Mutat Res* *711*, 61-72.
- Möckel, C., Lammens, K., Schele, A., and Hopfner, K.P. (2011). ATP driven structural changes of the bacterial Mre11:Rad50 catalytic head complex. *Nucleic Acids Res*.
- Moody, J.E., Millen, L., Binns, D., Hunt, J.F., and Thomas, P.J. (2002). Cooperative, ATP-dependent association of the nucleotide binding cassettes during the catalytic cycle of ATP-binding cassette transporters. *J Biol Chem* *277*, 21111-21114.
- Moreno-Herrero, F., de Jager, M., Dekker, N.H., Kanaar, R., Wyman, C., and Dekker, C. (2005). Mesoscale conformational changes in the DNA-repair complex Rad50/Mre11/Nbs1 upon binding DNA. *Nature* *437*, 440-443.
- Neale, M.J., Pan, J., and Keeney, S. (2005). Endonucleolytic processing of covalent protein-linked DNA double-strand breaks. *Nature* *436*, 1053-1057.
- New, J.H., Sugiyama, T., Zaitseva, E., and Kowalczykowski, S.C. (1998). Rad52 protein stimulates DNA strand exchange by Rad51 and replication protein A. *Nature* *391*, 407-410.
- Nimonkar, A.V., Genschel, J., Kinoshita, E., Polaczek, P., Campbell, J.L., Wyman, C., Modrich, P., and Kowalczykowski, S.C. (2011). BLM-DNA2-RPA-MRN and EXO1-BLM-RPA-MRN constitute two DNA end resection machineries for human DNA break repair. *Genes Dev* *25*, 350-362.
- Oakley, G.G., Tillison, K., Opiyo, S.A., Glanzer, J.G., Horn, J.M., and Patrick, S.M. (2009). Physical interaction between replication protein A (RPA) and MRN: involvement of RPA2 phosphorylation and the N-terminus of RPA1. *Biochemistry* *48*, 7473-7481.
- Ogawa, T., Yu, X., Shinohara, A., and Egelman, E.H. (1993). Similarity of the yeast RAD51 filament to the bacterial RecA filament. *Science* *259*, 1896-1899.

- Paull, T.T., and Gellert, M. (1998). The 3' to 5' exonuclease activity of Mre 11 facilitates repair of DNA double-strand breaks. *Mol Cell* *1*, 969-979.
- Paull, T.T., and Gellert, M. (1999). Nbs1 potentiates ATP-driven DNA unwinding and endonuclease cleavage by the Mre11/Rad50 complex. *Genes Dev* *13*, 1276-1288.
- Pedrazzi, G., Schwesinger, F., Honegger, A., Krebber, C., and Pluckthun, A. (1997). Affinity and folding properties both influence the selection of antibodies with the selectively infective phage (SIP) methodology. *FEBS Lett* *415*, 289-293.
- Perkins, E.J., Nair, A., Cowley, D.O., Van Dyke, T., Chang, Y., and Ramsden, D.A. (2002). Sensing of intermediates in V(D)J recombination by ATM. *Genes Dev* *16*, 159-164.
- Petrini, J.H. (2000). The Mre11 complex and ATM: collaborating to navigate S phase. *Curr Opin Cell Biol* *12*, 293-296.
- Pettersen, E.F., Goddard, T.D., Huang, C.C., Couch, G.S., Greenblatt, D.M., Meng, E.C., and Ferrin, T.E. (2004). UCSF Chimera--a visualization system for exploratory research and analysis. *J Comput Chem* *25*, 1605-1612.
- Rahal, E.A., Henriksen, L.A., Li, Y., Williams, R.S., Tainer, J.A., and Dixon, K. (2010). ATM regulates Mre11-dependent DNA end-degradation and microhomology-mediated end joining. *Cell Cycle* *9*, 2866-2877.
- Rass, E., Grabarz, A., Plo, I., Gautier, J., Bertrand, P., and Lopez, B.S. (2009). Role of Mre11 in chromosomal nonhomologous end joining in mammalian cells. *Nat Struct Mol Biol* *16*, 819-824.
- Richard, D.J., Cubeddu, L., Urquhart, A.J., Bain, A., Bolderson, E., Menon, D., White, M.F., and Khanna, K.K. (2011a). hSSB1 interacts directly with the MRN complex stimulating its recruitment to DNA double-strand breaks and its endo-nuclease activity. *Nucleic Acids Res* *39*, 3643-3651.
- Richard, D.J., Savage, K., Bolderson, E., Cubeddu, L., So, S., Ghita, M., Chen, D.J., White, M.F., Richard, K., Prise, K.M., *et al.* (2011b). hSSB1 rapidly binds at the sites of DNA double-strand breaks and is required for the efficient recruitment of the MRN complex. *Nucleic Acids Res* *39*, 1692-1702.
- Sabourin, M., and Zakian, V.A. (2008). ATM-like kinases and regulation of telomerase: lessons from yeast and mammals. *Trends Cell Biol* *18*, 337-346.
- Sambrook, J., and Russell, D.W. (2001). *Molecular Cloning: A Laboratory Manual*, 3rd edn (New York, Cold Spring Harbor Laboratory Press).
- San Filippo, J., Sung, P., and Klein, H. (2008). Mechanism of eukaryotic homologous recombination. *Annu Rev Biochem* *77*, 229-257.
- Schiller, C. (2011). Structural and functional analysis of the eukaryotic DNA repair proteins Mre11 and Nbs1.

- Sharples, G.J., and Leach, D.R. (1995). Structural and functional similarities between the SbcCD proteins of *Escherichia coli* and the RAD50 and MRE11 (RAD32) recombination and repair proteins of yeast. *Mol Microbiol* *17*, 1215-1217.
- Shibata, A., Conrad, S., Birraux, J., Geuting, V., Barton, O., Ismail, A., Kakarougkas, A., Meek, K., Taucher-Scholz, G., Lobrich, M., *et al.* (2011). Factors determining DNA double-strand break repair pathway choice in G2 phase. *EMBO J* *30*, 1079-1092.
- Shim, E.Y., Chung, W.H., Nicolette, M.L., Zhang, Y., Davis, M., Zhu, Z., Paull, T.T., Ira, G., and Lee, S.E. (2010). *Saccharomyces cerevisiae* Mre11/Rad50/Xrs2 and Ku proteins regulate association of Exo1 and Dna2 with DNA breaks. *EMBO J* *29*, 3370-3380.
- Smith, C.A., and Rayment, I. (1996). X-ray structure of the magnesium(II).ADP.vanadate complex of the *Dictyostelium discoideum* myosin motor domain to 1.9 Å resolution. *Biochemistry* *35*, 5404-5417.
- Soulas-Sprauel, P., Rivera-Munoz, P., Malivert, L., Le Guyader, G., Abramowski, V., Revy, P., and de Villartay, J.P. (2007). V(D)J and immunoglobulin class switch recombinations: a paradigm to study the regulation of DNA end-joining. *Oncogene* *26*, 7780-7791.
- Stewart, G.S., Maser, R.S., Stankovic, T., Bressan, D.A., Kaplan, M.I., Jaspers, N.G., Raams, A., Byrd, P.J., Petrini, J.H., and Taylor, A.M. (1999). The DNA double-strand break repair gene hMRE11 is mutated in individuals with an ataxia-telangiectasia-like disorder. *Cell* *99*, 577-587.
- Stracker, T.H., and Petrini, J.H. (2011). The MRE11 complex: starting from the ends. *Nat Rev Mol Cell Biol* *12*, 90-103.
- Stracker, T.H., Theunissen, J.W., Morales, M., and Petrini, J.H. (2004). The Mre11 complex and the metabolism of chromosome breaks: the importance of communicating and holding things together. *DNA Repair (Amst)* *3*, 845-854.
- Sung, P., and Klein, H. (2006). Mechanism of homologous recombination: mediators and helicases take on regulatory functions. *Nat Rev Mol Cell Biol* *7*, 739-750.
- Sutherland, B.M., Bennett, P.V., Sidorkina, O., and Laval, J. (2000). Clustered DNA damages induced in isolated DNA and in human cells by low doses of ionizing radiation. *Proc Natl Acad Sci U S A* *97*, 103-108.
- Svergun, D., Barberato, C., and Koch, M.H.J. (1995). CRY SOL - A program to evaluate x-ray solution scattering of biological macromolecules from atomic coordinates. *Journal of Applied Crystallography* *28*, 768-773.
- Svergun, D.I. (1992). Determination of the Regularization Parameter in Indirect-Transform Methods Using Perceptual Criteria. *Journal of Applied Crystallography* *25*, 495-503.
- Svergun, D.I. (1999). Restoring low resolution structure of biological macromolecules from solution scattering using simulated annealing. *Biophys J* *76*, 2879-2886.
- Trujillo, K.M., and Sung, P. (2001). DNA structure-specific nuclease activities in the *Saccharomyces cerevisiae* Rad50*Mre11 complex. *J Biol Chem* *276*, 35458-35464.

- Trujillo, K.M., Yuan, S.S., Lee, E.Y., and Sung, P. (1998). Nuclease activities in a complex of human recombination and DNA repair factors Rad50, Mre11, and p95. *J Biol Chem* 273, 21447-21450.
- Uchisaka, N., Takahashi, N., Sato, M., Kikuchi, A., Mochizuki, S., Imai, K., Nonoyama, S., Ohara, O., Watanabe, F., Mizutani, S., *et al.* (2009). Two brothers with ataxia-telangiectasia-like disorder with lung adenocarcinoma. *J Pediatr* 155, 435-438.
- Usui, T., Ohta, T., Oshiumi, H., Tomizawa, J., Ogawa, H., and Ogawa, T. (1998). Complex formation and functional versatility of Mre11 of budding yeast in recombination. *Cell* 95, 705-716.
- Usui, T., Petrini, J.H., and Morales, M. (2006). Rad50S alleles of the Mre11 complex: questions answered and questions raised. *Exp Cell Res* 312, 2694-2699.
- van der Linden, E., Sanchez, H., Kinoshita, E., Kanaar, R., and Wyman, C. (2009). RAD50 and NBS1 form a stable complex functional in DNA binding and tethering. *Nucleic Acids Res* 37, 1580-1588.
- van Gent, D.C., and van der Burg, M. (2007). Non-homologous end-joining, a sticky affair. *Oncogene* 26, 7731-7740.
- Varon, R., Vissinga, C., Platzer, M., Cerosaletti, K.M., Chrzanowska, K.H., Saar, K., Beckmann, G., Seemanova, E., Cooper, P.R., Nowak, N.J., *et al.* (1998). Nibrin, a novel DNA double-strand break repair protein, is mutated in Nijmegen breakage syndrome. *Cell* 93, 467-476.
- Venter, J.C., Adams, M.D., Myers, E.W., Li, P.W., Mural, R.J., Sutton, G.G., Smith, H.O., Yandell, M., Evans, C.A., Holt, R.A., *et al.* (2001). The sequence of the human genome. *Science* 291, 1304-1351.
- Waltes, R., Kalb, R., Gatei, M., Kijas, A.W., Stumm, M., Sobeck, A., Wieland, B., Varon, R., Lerenthal, Y., Lavin, M.F., *et al.* (2009). Human RAD50 deficiency in a Nijmegen breakage syndrome-like disorder. *Am J Hum Genet* 84, 605-616.
- Wang, M., Wu, W., Rosidi, B., Zhang, L., Wang, H., and Iliakis, G. (2006). PARP-1 and Ku compete for repair of DNA double strand breaks by distinct NHEJ pathways. *Nucleic Acids Res* 34, 6170-6182.
- Watson, J.D., and Crick, F.H. (1953). Molecular structure of nucleic acids; a structure for deoxyribose nucleic acid. *Nature* 171, 737-738.
- Wawrousek, K.E., Fortini, B.K., Polaczek, P., Chen, L., Liu, Q., Dunphy, W.G., and Campbell, J.L. (2010). Xenopus DNA2 is a helicase/nuclease that is found in complexes with replication proteins And-1/Ctf4 and Mcm10 and DSB response proteins Nbs1 and ATM. *Cell Cycle* 9, 1156-1166.
- Williams, G.J., Williams, R.S., Williams, J.S., Moncalian, G., Arvai, A.S., Limbo, O., Guenther, G., Sildas, S., Hammel, M., Russell, P., *et al.* (2011). ABC ATPase signature helices in Rad50 link nucleotide state to Mre11 interface for DNA repair. *Nat Struct Mol Biol* 18, 1084.

- Williams, R.S., Dodson, G.E., Limbo, O., Yamada, Y., Williams, J.S., Guenther, G., Classen, S., Glover, J.N., Iwasaki, H., Russell, P., *et al.* (2009). Nbs1 flexibly tethers Ctp1 and Mre11-Rad50 to coordinate DNA double-strand break processing and repair. *Cell* *139*, 87-99.
- Williams, R.S., Moncalian, G., Williams, J.S., Yamada, Y., Limbo, O., Shin, D.S., Grocock, L.M., Cahill, D., Hitomi, C., Guenther, G., *et al.* (2008). Mre11 dimers coordinate DNA end bridging and nuclease processing in double-strand-break repair. *Cell* *135*, 97-109.
- Williams, R.S., Williams, J.S., and Tainer, J.A. (2007). Mre11-Rad50-Nbs1 is a keystone complex connecting DNA repair machinery, double-strand break signaling, and the chromatin template. *Biochem Cell Biol* *85*, 509-520.
- Wiltzius, J.J., Hohl, M., Fleming, J.C., and Petrini, J.H. (2005). The Rad50 hook domain is a critical determinant of Mre11 complex functions. *Nat Struct Mol Biol* *12*, 403-407.
- Xiao, Y., and Weaver, D.T. (1997). Conditional gene targeted deletion by Cre recombinase demonstrates the requirement for the double-strand break repair Mre11 protein in murine embryonic stem cells. *Nucleic Acids Res* *25*, 2985-2991.
- Xie, A., Kwok, A., and Scully, R. (2009). Role of mammalian Mre11 in classical and alternative nonhomologous end joining. *Nat Struct Mol Biol* *16*, 814-818.
- Yang, Y.G., Saidi, A., Frappart, P.O., Min, W., Barrucand, C., Dumon-Jones, V., Michelon, J., Herceg, Z., and Wang, Z.Q. (2006). Conditional deletion of Nbs1 in murine cells reveals its role in branching repair pathways of DNA double-strand breaks. *EMBO J* *25*, 5527-5538.
- Ye, Y., and Godzik, A. (2004). FATCAT: a web server for flexible structure comparison and structure similarity searching. *Nucleic Acids Res* *32*, W582-585.
- You, Z., Chahwan, C., Bailis, J., Hunter, T., and Russell, P. (2005). ATM activation and its recruitment to damaged DNA require binding to the C terminus of Nbs1. *Mol Cell Biol* *25*, 5363-5379.
- Zahradka, K., Buljubasic, M., Petranovic, M., and Zahradka, D. (2009). Roles of ExoI and SbcCD nucleases in "reckless" DNA degradation in recA mutants of *Escherichia coli*. *J Bacteriol* *191*, 1677-1687.
- Zakharyevich, K., Ma, Y., Tang, S., Hwang, P.Y., Boiteux, S., and Hunter, N. (2010). Temporally and biochemically distinct activities of Exo1 during meiosis: double-strand break resection and resolution of double Holliday junctions. *Mol Cell* *40*, 1001-1015.
- Zha, S., Boboila, C., and Alt, F.W. (2009). Mre11: roles in DNA repair beyond homologous recombination. *Nat Struct Mol Biol* *16*, 798-800.
- Zhang, X., and Paull, T.T. (2005). The Mre11/Rad50/Xrs2 complex and non-homologous end-joining of incompatible ends in *S. cerevisiae*. *DNA Repair (Amst)* *4*, 1281-1294.

Zhu, J., Petersen, S., Tessarollo, L., and Nussenzweig, A. (2001). Targeted disruption of the Nijmegen breakage syndrome gene NBS1 leads to early embryonic lethality in mice. *Curr Biol* *11*, 105-109.

7. Abbreviations

aa	amino acid (residue)
°C	degree Celsius
6-FAM	6-carboxyfluorescein
Å	angstrom
ABC	ATP binding cassette
ADP	adenosine diphosphate
AMPPNP	adenosine 5'-(β,γ -imido)triphosphate
A-TLD	Ataxia-telangiectasia like disorder
ATP	adenosine triphosphate
ATPase N (C)	amino (carboxy) terminal segment of ATPase domain
ATP γ S	adenosine 5'-[γ -thio]triphosphate
BER	base-excision repair
BIR	break-induced replication
BMOE	bis-maleimidoethane
bp	base pair
BRCT	breast cancer carboxy terminus
Cap	Mre11's DNA capping domain
CSR	class switch recombination
C-terminus	carboxy terminus
CuSO ₄	copper sulfate
DNA	deoxyribonucleic acid
DNA-PKcs	catalytic subunit of DNA-dependent protein kinase
DSB	DNA double strand break
DSBR	DNA double strand break repair
dsDNA	double stranded DNA
ssDNA	single stranded DNA
<i>E. coli</i>	<i>Escherichia coli</i>
EDTA	ethylenediaminetetraacetic acid
EMSA	electrophoretic mobility shift assay
ESRF	European synchrotron radiation facility

FHA	forkhead associated
FLC	fluorescein
h	hours
HLH	helix-loop-helix motif
HPSF	high purity salt free
HR	homologous recombination
IPTG	isopropyl- β -D-thiogalactopyranosid
IR	ionizing radiation
kDa	kilo dalton
LB	Lysogeny Broth
M	molar
MES	2-(<i>N</i> -morpholino)ethanesulfonic acid
Mg	magnesium
MMEJ	microhomology-mediated end-joining
min	minute
<i>M. jannaschii</i> (<i>Mj</i>)	<i>Methanococcus jannaschii</i>
Mn	manganese
MR	Mre11:Rad50
Mre11	meiotic recombination
MRN(X)	Mre11:Rad50:Nbs1(Xrs2) (in <i>S. cerevisiae</i>)
NBD	nucleotide binding domain
Nbs	Nijmegen breakage syndrome
NBSLD	Nbs-like disorder
NER	nucleotide-excision repair
alt-NHEJ	alternative non-homologous end-joining
c-NHEJ	classical non-homologous end-joining
nt	nucleotide
N-terminus	amino terminus
Nuc	Mre11's nuclease domain
OD ₆₀₀	optical density at 600 nm
PAGE	polyacrylamide gelelectrophoresis
PARP1	poly(ADP-ribose) polymerase 1
PCNA	proliferating cell nuclear antigen

PCR	polymerase chain reaction
PDB	protein data bank
PEG	polyethylene glycol
<i>P. furiosus (Pf)</i>	<i>Pyrococcus furiosus</i>
pH	potential of hydrogen
Rad	radiation sensitive
Rec	recombination
rms	root mean square
ROS	reactive oxygen species
RPA	replication protein A
rpm	rotation per min
RT	room temperature
<i>S. cerevisiae (Sc)</i>	<i>Saccharomyces cerevisiae</i>
<i>S. pombe (Sp)</i>	<i>Schizosaccharomyces pombe</i>
SAXS	small angle x-ray scattering
SDS	sodium dodecyl-sulfate
SDSA	synthesis-dependent strand annealing
sec	second
SLS	Swiss light source
SMC	structural maintenance of chromosomes
SSA	single strand annealing
SSB	DNA single strand break
TB	tris-borate
<i>T. maritima (Tm)</i>	<i>Thermotoga maritima</i>
Topo	topoisomerase
Tris	<i>tris</i> (hydroxymethyl)aminomethane
UV	ultraviolet
[VO ₄] ³⁻	orthovanadate ion
wt	wild type
μ	micro
Zn	zinc

8. Curriculum vitae

Personal details

Name	Carolyn Möckel
Date of birth	02/23/1982
Place of birth	Munich, Germany
Nationality	German

Education

Oct 2002 – Jul 2007	Diplom-Biol. Univ. (Master's Degree) in Biology. University of Munich (LMU), Munich, Germany. <u>Main subjects:</u> Microbiology, Biochemistry, Genetics.
Sep 1992 – Jun 2001	Abitur (German High School Diploma). Lion-Feuchtwanger-Gymnasium (Secondary School), Munich. Majors: Mathematics, Biology. <u>Final thesis:</u> Gene therapy in somatic and germline cells.
Jul 1998 – Oct 1998	Abroad Communication (Student Exchange). San José, California, USA.

Academic training

Nov 2007 – now	PhD Thesis in Structural Biology. <u>Subject:</u> <i>Structural and functional analysis of ATP dependent conformational changes in the bacterial Mre11:Rad50 complex.</i> Gene Center, University of Munich (LMU), Munich, Germany.
Oct 2006 – Jul 2007	Diploma Thesis in Microbiology. <u>Subject:</u> <i>Physiological relevance of the two-component-system CbrA:CbrB of Pseudomonas putida KT2440.</i> Laboratory of Microbiology, Department of Microbiology and Genetics, University of Munich (LMU), Munich, Germany.
Mar 2006 - May 2006	Voluntary Internship in Genetics. <u>Subject:</u> <i>Genetical studies.</i> Laboratory of Genetics, Biomedical research center (CIBO), Guadalajara, Mexico.
Oct 2005 – Mar 2006	Research Assistant. <u>Subject:</u> <i>Characterization of the type III export signal of the flagellar hook scaffolding protein FlgD of Escherichia coli.</i> Laboratory of Microbiology, Department of Microbiology and Genetics, University of Munich (LMU), Munich, Germany.

9. Acknowledgements

I would like to thank everybody who has contributed to the successful completion of this work.

First of all, I want to thank my supervisor Prof. Dr. Karl-Peter Hopfner. You gave me not only the opportunity to work within this nice team but also permanently supported me during the last four years. You infected me with your enthusiasm about this project and you gave me at the right time the freedom to create my own ideas.

I am also thankful to Prof. Dr. Patrick Cramer for being the second examiner of this thesis.

I want to thank the members of the “Fellowship of the Ring”, especially Katja Lammens. You always supported me and taught me everything about this project and about structural biology. It was extremely important for me that you trusted in me and my capabilities and that you kept me grounded all the time. Thanks for that! Many thanks also to Alexandra Schele who contributed to this project with her fantastic work she did. But also for being always calm even if a hundred people wanted something from her like new stocks or new competent cells when they were spontaneously emptied again. I want to thank Christian Schiller for being the MR lexicon. You always had an answer for my question, even if they were stupid or you did not have time. You also built me up quite a few times during the last year when I was not able to see things positive anymore. Many thanks also to Ania Rojowska and Alexander Mengel who joined later on the project.

I would like to thank the whole Hopfner group for the nice atmosphere and for everything I learned from them. Especially I want to thank Matthew Bennett for proofreading and Maria Lucas and Matt for having always time if I needed something. Furthermore I want to thank Gregor Witte and Sofia Hartung who helped me a lot with their expertise in SAXS and especially Gregor for always helping me with technical problems. Even when you are annoyed, it is great to have someone like you in the group.

Nicht zuletzt möchte ich meinen Eltern, meinen Geschwistern und meinem Freund danken die nie an mir gezweifelt haben und mich ausnahmslos unterstützt und ermutigt haben.